# Chemical biological studies for the development of drug seeds for Parkinson's disease

June 2020

Tetsushi Kataura

A Thesis for the Degree of Ph.D. in Science

# Chemical biological studies for the development of drug seeds for Parkinson's disease

June 2020

Graduate School of Science and Technology

Keio University

Tetsushi Kataura

# Contents

# Abbreviations

| | |
|---|---|
| ADK | adenosine kinase |
| AMPK | AMP-activated protein kinase |
| ATF4 | activating transcription factor 4 |
| BLI | biolayer interferometry |
| CHOP | C/EBP homologous protein |
| eIF2α | eukaryotic translation initiation factor 2 alpha |
| ER | endoplasmic reticulum |
| FDA | Food and Drug Administration |
| GRP78 | glucose-regulated protein 78 |
| GSH | Glutathione |
| HD | Huntington's disease |
| HO-1 | heme oxygenase-1 |
| HSP90 | heat shock protein 90 |
| IRE1α | inositol-requiring kinase 1 alpha |
| JAK | Janus kinase |
| JNK | c-Jun N-terminal kinase |
| Keap1 | Kelch-like ECH-associated protein 1 |
| LC3 | microtubule associated protein 1 light chain 3 beta |
| LKB1 | liver kinase B1 |
| MPP$^+$ | 1-methyl-4-phenylpyridinium |
| mTOR | mammalian target of rapamycin |
| mTORC | mTOR complex |
| NAC | N-acetylcysteine |
| Neh | Nrf2-ECH-homology |
| NGF | nerve growth factor |
| NMDA | N-methyl-D-aspartate |
| Nrf2 | nuclear factor erythroid 2-related factor 2 |
| PCA | principal component analysis |
| PD | Parkinson's disease |
| PDA | pancreatic ductal adenocarcinoma |

| | |
|---|---|
| PERK | PKR-like ER kinase |
| PKC | protein kinase C |
| PMA | phorbol 12-myristate 13-acetate |
| ROCK | Rho-associated coiled-coil protein kinase |
| ROS | reactive oxygen species |
| RR | ribonucleotide reductase |
| SD | standard deviation |
| SEM | standard error of the mean |
| TFEB | transcription factor EB |
| TGF-$\beta$ | transforming growth factor beta |
| Tpl2 | tumor progression locus 2 |
| ULK1 | unc-51 like autophagy activating kinase 1 |
| Vps34 | phosphatidylinositol 3-kinase catalytic subunit type 3 |
| XBP1 | X-box binding protein 1 |
| ZnPP | zinc (II) protoporphyrin IX |

# Chapter 1


# General introduction

## 1.1. Chemical biology

Chemical biology is an interdisciplinary study done at the interface of chemistry and biology. In this area, small molecules produced by organic and synthetic chemistry or harvested from natural resources such as secondary metabolites from microbial origin are utilized as chemical probes to understand the molecular mechanisms underlying biological events. Chemical genetics is a part of chemical biology and has a root in genetics (Figure 1-1). Classical genetics is achieved by screening of genes that have random mutation and by isolation of mutant individuals that are responsible for a phenotype of interest (forward genetics). On the other hand, functional analysis of a specific gene against a phenotype by using gene modification including deletion, silencing, and point mutation is called reverse genetics. Similarly, chemical genetics is consisted of forward chemical genetics and reverse chemical genetics. In forward chemical genetics, bioactive small molecules that modulate an interested phenotype are screened from chemical library, and then the hit compounds are used as bioprobes to identify the target proteins and signal transduction pathways that are responsible for the phenotype. In reverse chemical genetics, small molecules that interact with a specific protein of interest are screened from chemical library and modified through synthetic chemistry, and then the function of protein is analyzed by the effect on the phenotype using the chemicals. So far, chemical genetics has been revealed a wide variety of molecular mechanisms. For example, identification of FK506 binding protein, calcineurin, by using FK506 that inhibits T lymphocyte signal transduction, revealed not only the mechanism of action of FK506 but also how T cells-mediated immunity is regulated [1]. Moreover, chemical genetics approach is also compatible with drug discovery research because it is necessary for novel drugs to be

elucidated their mechanisms of action, providing us to use for disease-modifying therapy and to predict and take measure to side effects of the drugs [2].

Chemical genomics is a systematic and integrated chemical genetics-approach based on functional genomics. For this, chemical libraries consisted of small molecules that are target-identified (have well-established modes of action) are used for screening. Target information of the hit compounds from screening can be used to i) identify the diverse biological pathways; ii) novel drug targets; iii) predict the modes of action of uncharacterized compounds. For example, chemical genomics was applied to reveal that target of rapamycin (TOR) has a diverse biological activity such as nutrient sensing, regulation of transcription, autophagy, ubiquitin-dependent proteasomal degradation, and microtubule related function in *Saccharomyces cerevisiae* [3]. Second example is the application to cancer research, which indicated that the inhibition of heat shock protein 90 (HSP90) could be a novel therapeutic strategy [4]. Thus, chemical biology including chemical genetics and chemical genomics plays a critical role in biological research and drug discovery.
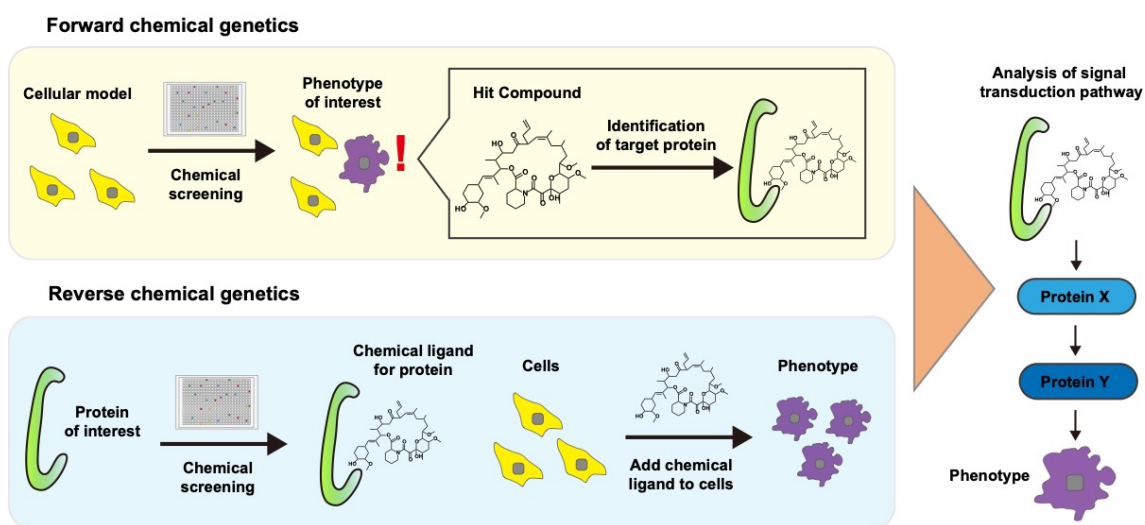


**Figure 1-1.** Overview illustration of chemical genetics.

**1.2. Parkinson's disease (PD)**

Parkinson's disease (PD) is a second common neurodegenerative disease characterized as progressive movement disorder called parkinsonism including bradykinesia, tremor, and posture imbalance. PD results mainly from progressive degeneration of dopaminergic neurons in the substantia nigra, increased microglial activation and accumulation of proteins in surviving dopaminergic neurons, known as Lewy bodies [5]. While PD affects more than 8 million people all over the world [6], current PD medications such as levodopa only relieve PD symptoms by supplementing the function impaired by dopamine deficiency. Chronic administration of these medications causes a shortened duration of action and severe side effects such as dyskinesia [7]. However, there is still no effective treatment that take the place of dopamine supplementation and slow progression of PD.

Although the cause of PD is still unknown, a considerable number of studies over the past few decades have identified the risk factors and proposed the mechanism of neuronal degeneration. Mechanisms of neuronal cell death have been implicated in association with elevated oxidative stress that damages cellular proteins and organelles including mitochondria and dysfunction of protein degradation systems, ubiquitin-proteasomal degradation and autophagy pathway (Figure 1-2). Mitochondrial dysfunction leads to energy depletion, further reactive oxygen species (ROS) production and induction of cell death signaling. Accumulation of aggregated/nonfunctional proteins impairs normal cellular functions of neurons. Possible causes of cellular degeneration include gene mutations and environmental factors. Some mutation of genes including α-synuclein, leucine-rich repeat kinase 2 (LRRK2), and β-glucocerebrosidase (GBA) are frequent in several populations of familial and sporadic

PD patients. In familial PD, mutations in PTEN-induced kinase 1 (PINK1) and PARKIN that are required for mitochondrial quality control through mitophagy (mitochondrial autophagy) were identified [8]. Although these gene mutations could illustrate the impaired cellular function observed in neurons affected by PD, around 90% PD patients have no gene mutations involving with familial PD. On the other hand, exposure to certain toxins such as pesticides may increase the risk of PD [9]. Moreover, useful biomarkers related to environmental factors have been elucidated using metabolomics technologies leading to understanding the metabolic pathways and networks in PD [10]. Interventions in the dysregulated metabolic pathways in PD are expected to be novel therapeutic strategies.

  Symptoms of PD appear when 50%-70% of nigrostriatal dopaminergic neurons have been lost, therefore the population of undiagnosed asymptomatic patients would be large [9]. In this view, presymtomatic diagnosis and treatment at early stage are critical to improve the prognosis of PD patients. Absolutely, effective drugs that can suppress further neuronal cell death and ultimately slow or stop progression of PD are required for patients not only at pre-onset but also at any stage of PD.
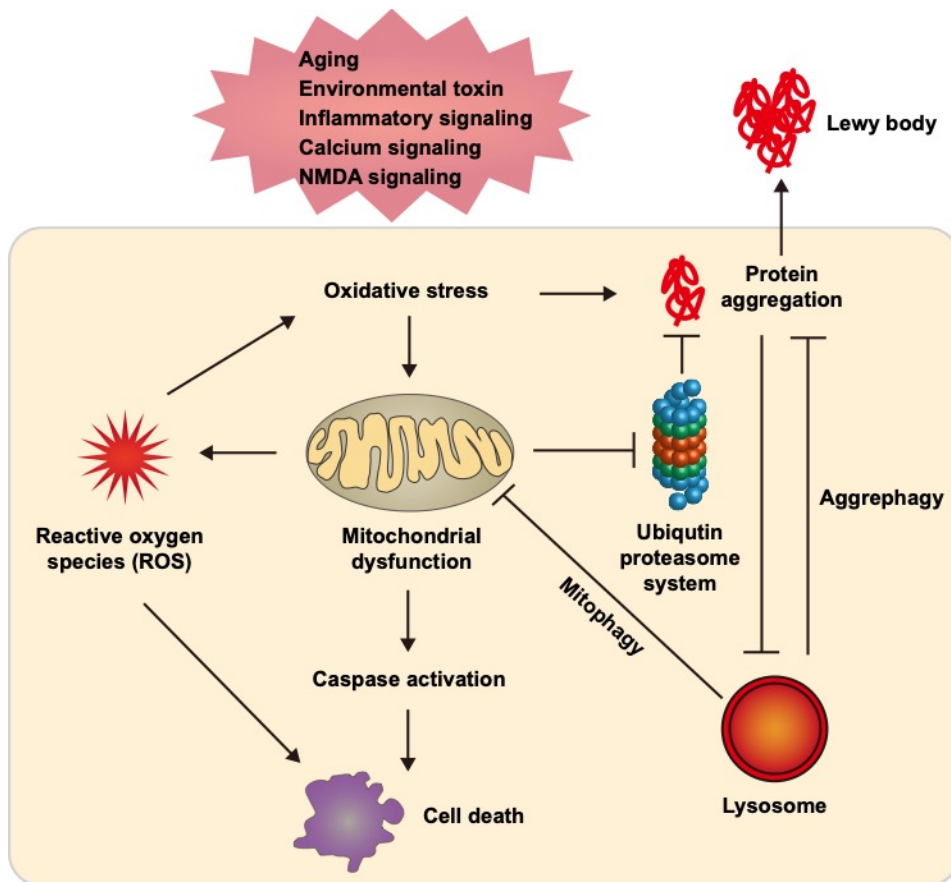
**Figure 1-2.** Molecular mechanisms of cellular degeneration in PD (image adapted from [11]).

## 1.3. Overview of the present study

The development of new drug seeds for PD treatment is becoming more and more important along with population aging that increases the risk of PD. Considering that chemical biology has been contributed to biological research and drug discovery, chemical biological approach could be effective in PD research. In the present study, I conducted two chemical biological studies for the development of novel drug seeds or strategies for PD. In Chapter 2, I describe a novel drug seed, BRUP-1 that modulates heme redox metabolism and exerts potent neuroprotective activity, identified by original phenotypic screening (forward chemical genetics) that targets the intracellular bilirubin level which recently elucidated as a PD biomarker. In chapter 3, I describe an integrated chemical genomic study for the pathway analyses and neuroprotective activity of autophagy inducers that are expected to be a new class of drugs for neurodegenerative disease including PD by eliminating cytotoxic/nonfunctional protein aggregates. These findings may provide conceivable strategies for novel PD treatment.

# Chapter 2

## BRUP-1, an intracellular bilirubin modulator, exerts neuro-protective activity in a cellular Parkinson's disease model

## 2.1. Introduction

Parkinson's disease (PD) is the second most common neurodegenerative disease and is characterized by progressive loss of dopaminergic neurons that contain cytoplasmic inclusions known as Lewy bodies, elevated oxidative stress, and mitochondrial dysfunction [12,13]. Various mitochondrial pathogenesis events such as mitochondrial DNA changes, decreased elimination of damaged mitochondria, and insufficient fatty acid β-oxidation have been proposed. Oxphos dysregulation induced by 1-methyl-4-phenyl-1,2,5,6-tetrahydropyridine (MPTP), a mitochondria complex I inhibitor, causes clinical features of PD, and *in vivo* and cellular models with MPTP (its metabolite, 1-Methyl-4-phenylpyridinium (MPP$^+$)) or rotenone have been established as PD models [14-17]. Heme oxygenase-1 (HO-1), the stress-inducible isoform of HO, may have cytoprotective properties against oxidative stress and mitochondrial dysfunction in PD [18,19]. These reports suggest that dysfunction in heme metabolism may lead to lower levels of bilirubin and negatively impact the pathogenesis of PD. However, whether interventions that affect heme metabolism lead to neuroprotection remains unclear.

Bilirubin, the end product of heme metabolism, is a potent antioxidant that can protect biomolecules such as lipids against oxidative stress [20-22]. In heme metabolism, the rate-limiting enzyme, HO, catabolizes heme into iron, carbon monoxide, and biliverdin, which is converted to bilirubin by biliverdin reductase, which is the enzyme responsible for bilirubin production [23-25]. This metabolic pathway plays an essential role in maintaining cellular homeostasis by removing cytotoxic free heme [26], converting heme into the antioxidant bilirubin, and producing iron, which is reutilized to synthesize iron-containing proteins [27], and carbon monoxide, which serves as a signal messenger that modulates inflammation and apoptosis signaling [28,29]. Clinically,

bilirubin levels in serum or urine are widely used to assess liver function [30]. A low serum bilirubin level is a strong predictive biomarker of disabilities in activities of daily living in elderly patients with type 2 diabetes mellitus [31]. Whether serum levels of bilirubin in PD are up-regulated or down-regulated is still controversial. Some studies show that bilirubin levels are negatively correlated with disease severity or positively correlated with preservation of dopaminergic neurons in PD as assessed with F-fluorinated-N-3-fluoropropyl-2-β-carboxymethoxy-3-β-(4-iodophenyl)nortropane-positron emission tomography [32-36]. Despite its biological and clinical importance, few studies have investigated the protective effects of bilirubin on PD cellular models using a chemical probe technique.

In this study, I show that the mitochondrial inhibitor, rotenone, significantly decreased intracellular bilirubin level via HO-1 down-regulation in human liver HepG2 cells as seen with Flag-UnaG-2A-mCherry, which is a ratiometric bilirubin probe that shows the bilirubin level and internal expression level. I performed chemical screening to obtain a novel bilirubin modulator compound named BRUP-1. I found that BRUP-1 elevated intracellular bilirubin levels by activating the nuclear factor erythroid 2-related factor 2 (Nrf2)-HO-1 pathway. Kinetic analysis using biolayer interferometry (BLI)-based assay showed BRUP-1 directly inhibited the interaction between Kelch-like ECH-associated protein 1 (Keap1) Kelch domain and Nrf2 ETGE motif within the Nrf2-ECH-homology (Neh) 2 domain. Furthermore, BRUP-1 showed potent neuroprotective activity in neuronal cells. These results suggest that chemical modulation of heme redox metabolism may be a new treatment strategy for PD.

## 2.2. Results

### 2.2.1. Ratiometric fluorescent probe for intracellular bilirubin level

UnaG is a green fluorescent protein from Japanese eel muscle; its fluorescence is triggered by bilirubin binding [37]. Therefore, UnaG was used to measure the bilirubin level [38,39]. To assess the intracellular bilirubin level easily, I developed the Flag-UnaG-2A-mCherry probe, which produces equal amounts of Flag-UnaG as the bilirubin reporter and mCherry as the internal expression control (Figure 2-1) due to ribosomal skipping at the 2A viral sequencing site [40]. This probe was transfected into HepG2 cells to obtain stable expression of this probe. This approach allows evaluation of the intracellular bilirubin level according to the signal intensity ratio of UnaG/mCherry. In HepG2 cells stably expressing this probe, UnaG-2A-mCherry was efficiently cleaved into Flag-UnaG and mCherry, whereas the uncleaved form of Flag-UnaG-2A-mCherry (approximately 45 kDa) was not detected (Figure 2-2). Following treatment of cells with bilirubin or biliverdin, the fluorescence intensity of UnaG, but not mCherry was enhanced (Figure 2-3), and the UnaG/mCherry ratio was increased in a dose-dependent manner (Figure 2-4). Thus, HepG2 cells stably expressing the Flag-UnaG-2A-mCherry construct that I cloned are useful for easy evaluation of the intracellular bilirubin level.
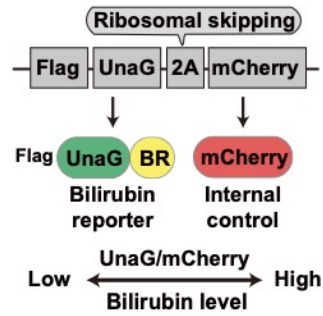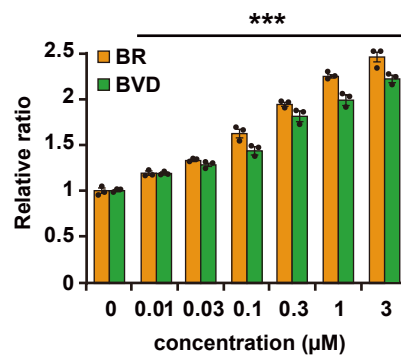
**Figure 2-1.** Schematic illustration of the intracellular bilirubin probe, Flag-UnaG-2A-mCherry.
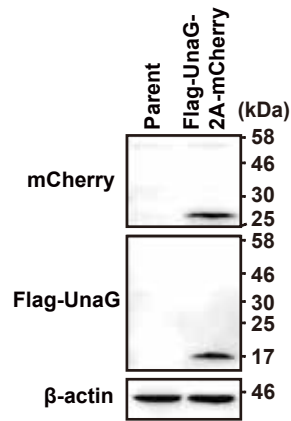


**Figure 2-2.** HepG2 cells stably expressing the Flag-UnaG-2A-mCherry probe were analyzed with western blotting.
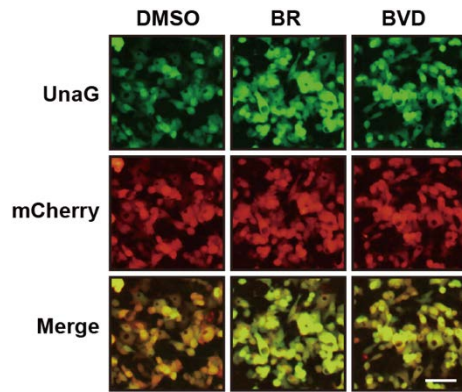
**Figure 2-3.** HepG2 cells stably expressing Flag-UnaG-2A-mCherry were treated with 1 $\mu$M bilirubin (BR) or biliverdin (BVD) for 24 hrs. The scale bar represents 40 $\mu$m.
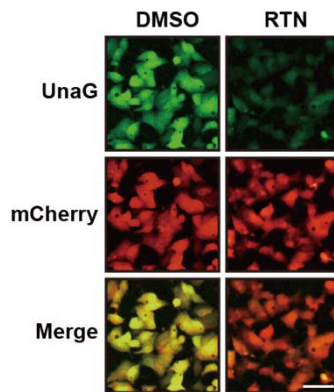


**Figure 2-4.** HepG2 cells stably expressing Flag-UnaG-2A-mCherry were treated with the indicated concentrations of bilirubin (BR) or biliverdin (BVD) for 24 h followed by the intracellular bilirubin assay. Data are representative of experiments and are shown as the mean ± standard deviation (SD). ***$p < 0.001$ (Dunnett's test).

## 2.2.2. The mitochondrial complex I inhibitor, rotenone, decreases the intracellular bilirubin level via HO-1 down-regulation in HepG2 cells

Hatano *et al*. recently reported that serum levels of bilirubin decrease significantly based on disease severity and progression in PD patients [34]. Rotenone, a direct inhibitor of mitochondria complex I, is usually employed to mimic parkinsonian motor symptoms *in vitro* and *in vivo* [15,41]. Therefore, I first examined whether rotenone could induce a decrease in the intracellular bilirubin level using HepG2 cells expressing Flag-UnaG-2A-mCherry. As shown in Figure 2-5, the signal intensity of UnaG but not mCherry was decreased by rotenone treatment in HepG2 cells. A dose-dependent (Figure 2-6) and time-dependent (Figure 2-7) decrease in the UnaG/mCherry ratio by rotenone was observed. These data indicated that rotenone significantly lowered the intracellular bilirubin level in HepG2 cells.

Intracellular bilirubin is mainly generated through heme degradation pathways, and HO is the rate-limiting enzyme that degrades heme into bilirubin [42]. Between two isoforms of HO (HO-1 and HO-2), I focused HO-1 because HO-1 is the stress-inducible isoform while HO-2 is the constitutive isoform [25]. I confirmed that knockdown of HO-1 in HepG2 cells lowered the intracellular bilirubin level (Figure 2-8); conversely, overexpression of HO-1 raised the intracellular bilirubin level (Figure 2-9). Therefore, I next examined the effect of rotenone on the expression level of HO-1. I found that HO-1 was down-regulated by rotenone treatment at both the protein (Figure 2-10) and mRNA (Figure 2-11) levels, in accordance with the decrease in intracellular bilirubin levels (Figure 2-7). These results indicated that rotenone induced the decrease in the intracellular bilirubin level via HO-1 down-regulation in HepG2 cells.

**Figure 2-5.** HepG2 cells stably expressing Flag-UnaG-2A-mCherry were treated with 1 $\mu$M rotenone (RTN) for 24 h. The scale bar represents 40 $\mu$m.
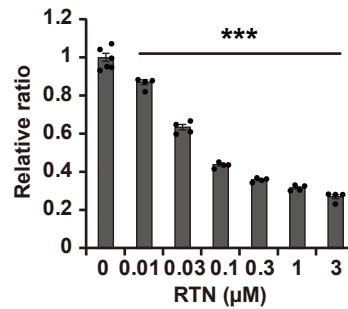


**Figure 2-6.** HepG2 cells stably expressing Flag-UnaG-2A-mCherry were treated with the indicated concentrations of rotenone for 24 h followed by the intracellular bilirubin assay. Data are shown as the mean ± SD (n=4-6) . ***p < 0.001 (Dunnett's test).
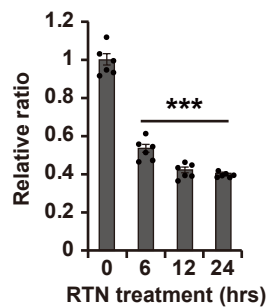


**Figure 2-7.** HepG2 cells stably expressing Flag-UnaG-2A-mCherry were treated with 1 $\mu$M rotenone for the indicated times followed by the intracellular bilirubin assay. Data are shown as the mean ± SD (n=6). ***p < 0.001 (Dunnett's test).
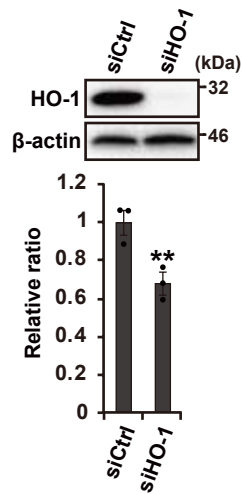
**Figure 2-8.** HepG2 cells stably expressing Flag-UnaG-2A-mCherry were transfected with HO-1 siRNA and then subjected to western blotting analysis and the intracellular bilirubin assay. Data are shown as the mean ± standard error of the mean (SEM) (n = 3). **p < 0.01 (Student's t test).
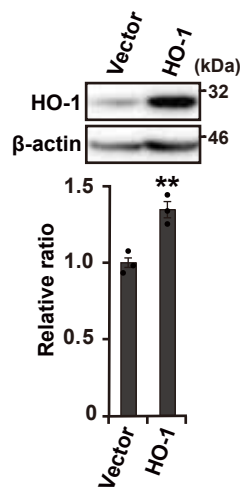


**Figure 2-9.** HepG2 cells stably expressing Flag-UnaG-2A-mCherry were transfected with the HO-1 vector and then subjected to western blotting analysis and the intracellular bilirubin assay. Data are shown as the mean ± SEM (n = 3). **p < 0.01 (Student's t test).

**Figure 2-10.** HepG2 cells were treated with 1 $\mu$M rotenone for the indicated times followed by western blotting analysis. Data are shown as the mean $\pm$ SEM (n = 3). ***p < 0.001 (Dunnett's test).
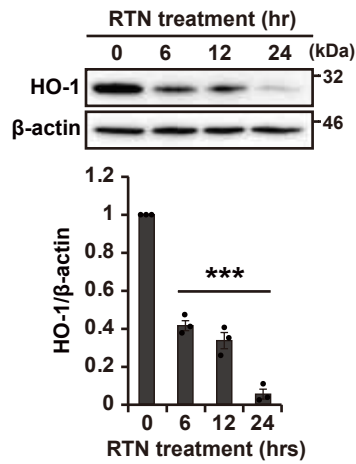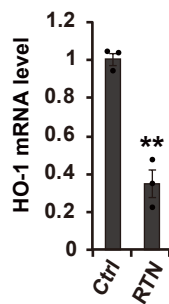


**Figure 2-11.** HepG2 cells were treated with 1 $\mu$M rotenone for 12 h followed by qRT-PCR analysis. Data are shown as the mean $\pm$ SEM (n = 3). **p < 0.01 (Student's t test).

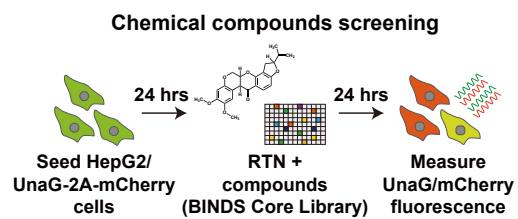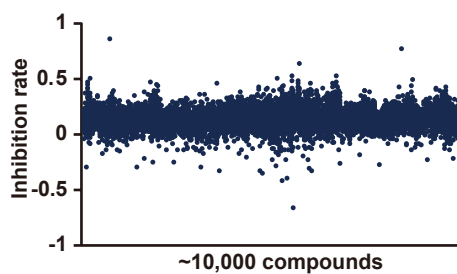### 2.2.3. Identification of BRUP-1, which modulates cellular bilirubin levels via HO-1 up-regulation

Oxidative stress that results from an imbalance in redox homeostasis is considered the major cause of neuronal cell death leading to PD pathogenesis [43]. Because many studies have implicated bilirubin as a strong antioxidant biomolecule [20,44], pharmacological modulation of bilirubin production may lead to cytoprotection in various diseases that are triggered by oxidative stress [45]. These ideas raised the possibility that the bilirubin level is not only a biomarker of PD progression but also a therapeutic target of PD. Therefore, I searched a chemical library consisting of 9,600 compounds for molecules that restore the rotenone-reduced intracellular bilirubin level in the above established HepG2 cell system (Figure 2-12). I set the threshold of the inhibition score at 0.3 to select hits from the first screening (Figure 2-13) and re-tested select compounds to confirm their activity (Figure 2-14). As a result, I identified BRUP-1 (Figure 2-15) as one of the top hits that restored intracellular bilirubin levels. BRUP-1 significantly suppressed rotenone-induced intracellular bilirubin depletion in a dose-dependent manner (Figure 2-16, 17) as well as rotenone-induced a decrease in extracellular bilirubin levels in the cultured medium (Figure 2-18). Cell viability was not affected as judged by the mCherry intensity (Figure 2-19). I then investigated the effect of BRUP-1 on rotenone-suppressed HO-1 expression. I found that BRUP-1 up-regulated HO-1 at both the mRNA (Figure 2-20) and protein (Figure 2-21) levels, indicating that BRUP-1 induced the up-regulation of HO-1 expression, thereby restoring the rotenone-reduced intracellular bilirubin level.

**Chemical compounds screening**

Seed HepG2/
UnaG-2A-mCherry
cells

24 hrs →

RTN +
compounds
(BINDS Core Library)

24 hrs →

Measure
UnaG/mCherry
fluorescence

**Figure 2-12.** Schematic illustration of chemical screening.



**Figure 2-13.** Scatter plot of the inhibition rate against rotenone of each compound in the first screening.
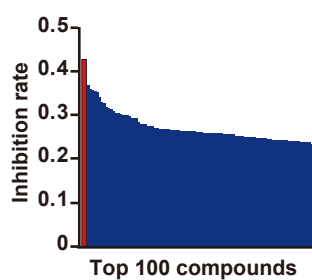


**Figure 2-14.** Column showing the re-tested inhibition rate against rotenone for the top 100 compounds in the first screening.
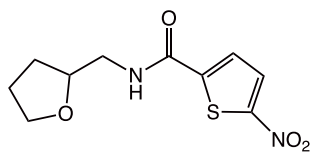
**BRUP-1**
Chemical Formula: $C_{10}H_{12}N_2O_4S$
Molecular Weight: 256.28

**Figure 2-15.** Chemical structure, chemical formula, and molecular weight of BRUP-1.
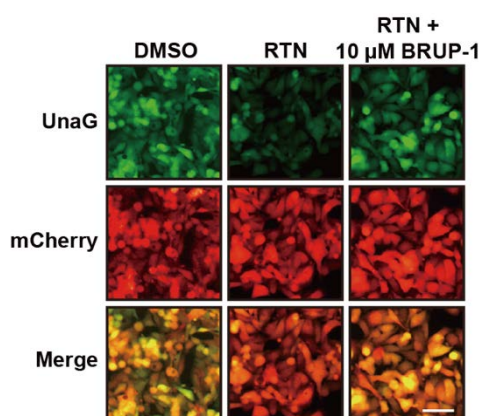


**Figure 2-16.** HepG2 cells stably expressing Flag-UnaG-2A-mCherry were treated with BRUP-1 in the presence or absence of 1 $\mu$M rotenone for 24 h followed by fluorescence microscopy. The scale bar represents 40 $\mu$m.
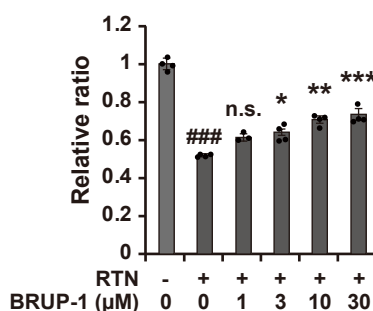


**Figure 2-17.** HepG2 cells stably expressing Flag-UnaG-2A-mCherry were treated with BRUP-1 in the presence or absence of 1 $\mu$M rotenone for 24 h followed by the intracellular bilirubin assay. Data are shown as the mean ± SEM (n = 4). [###]$p < 0.001$ (relative to untreated cells, Tukey's test), n.s., not significant, *$p < 0.05$, **$p < 0.01$, ***$p < 0.001$ (Dunnett's test).
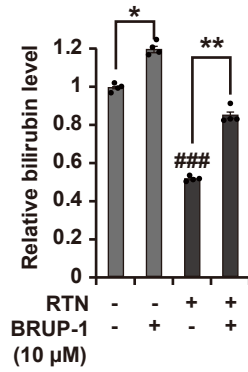
**Figure 2-18.** HepG2 cells were treated with 10 $\mu$M BRUP-1 in the presence or absence of 1 $\mu$M rotenone for 24 h followed by the *in vitro* bilirubin assay. Data are shown as the mean ± SEM (n = 4). ###p < 0.001 (relative to untreated cells, Tukey's test), *p < 0.05, **p < 0.01 (Student's t test).
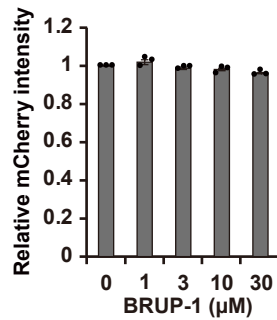


**Figure 2-19.** HepG2 cells stably expressing Flag-UnaG-2A-mCherry were treated with the indicated concentrations of BRUP-1 for 24 h, and the mCherry intensity was measured using a microplate reader. Data are shown as the mean ± SEM (n = 3).
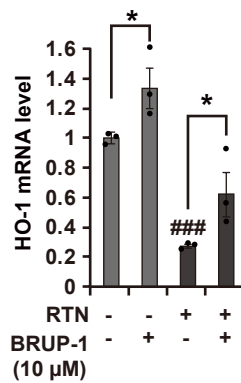
**Figure 2-20.** HepG2 cells were treated with the indicated concentrations of BRUP-1 in the presence or absence of 1 $\mu$M rotenone for 12 h followed by qRT-PCR. Data are shown as the mean ± SEM (n = 3). [###]p < 0.001 (relative to untreated cells, Tukey's test), *p < 0.05 (Student's t test).
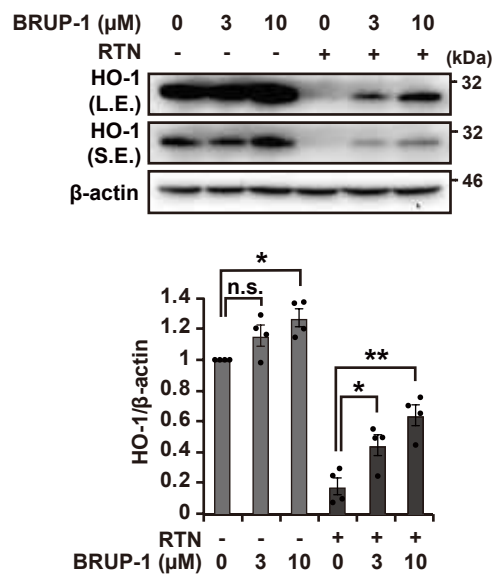


**Figure 2-21.** HepG2 cells were treated with the indicated concentrations of BRUP-1 in the presence or absence of 1 $\mu$M rotenone for 24 h followed by western blotting analysis. Data are shown as the mean ± SEM (n = 4). n.s., not significant, *p < 0.05, **p < 0.01 (Dunnett's test).

**2.2.4. BRUP-1 restores intracellular bilirubin levels via Nrf2 activation**

Nrf2 signaling is one of the major cellular redox pathways [46]. Nrf2 tightly and transcriptionally regulates the expression of target genes including HO-1 in response to a variety of stress conditions such as oxidative stress and inflammation [47]. Therefore, I next examined whether Nrf2 is actually involved in BRUP-1-induced expression of HO-1. The subcellular localization of Nrf2 is one of the major determining factors for its function. Thus, I performed immunofluorescence analysis to determine the effect of BRUP-1 on nuclear translocation of Nrf2. As shown in Figure 2-22, Nrf2 immunofluorescence in the nuclei was increased following BRUP-1 treatment, indicating that BRUP-1 induced Nrf2 translocation from the cytosol to the nucleus, resulting in Nrf2 activation. In line with these findings, when Nrf2 was knocked down using siRNA, BRUP-1 induced up-regulation of neither HO-1 nor p62, a well-known Nrf2 target gene [48], at both the protein and mRNA levels (Figure 2-23, 24). In addition, restoration of the rotenone-reduced intracellular bilirubin level by BRUP-1 was not observed following knockdown of HO-1 or Nrf2 (Figure 2-25). These results indicated that BRUP-1 increases the intracellular bilirubin level via activation of the Nrf2-HO-1 axis.

23
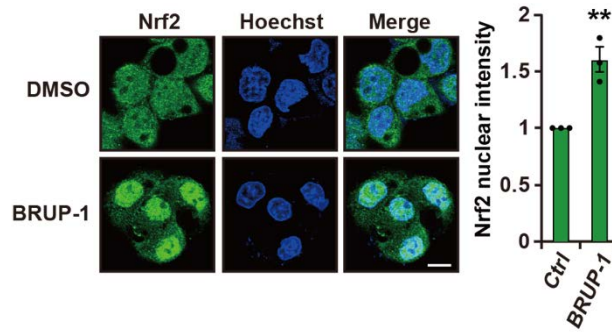
**Figure 2-22.** HepG2 cells were treated with 10 $\mu$M BRUP-1 for 3 h and then subjected to immunofluorescence analysis using anti-Nrf2 antibody. The scale bar represents 10 $\mu$m. Data are shown as the mean ± SEM (n = 3). **p < 0.01 (Student's t test).
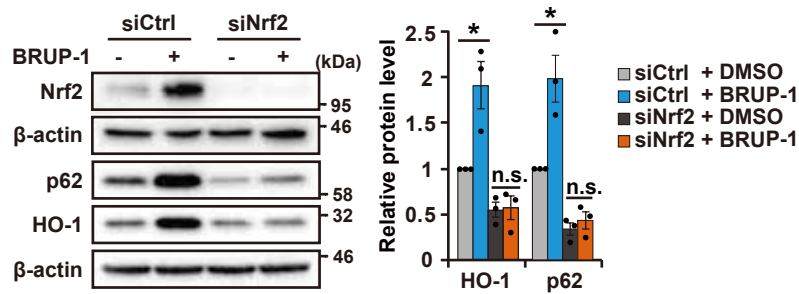


**Figure 2-23.** HepG2 cells transfected with Nrf2 siRNA or control siRNA were treated with 10 $\mu$M BRUP-1 for 24 h followed by western blotting analysis. Data are shown as the mean ± SEM (n = 3). n.s., not significant, *p < 0.05 (Student's t test).
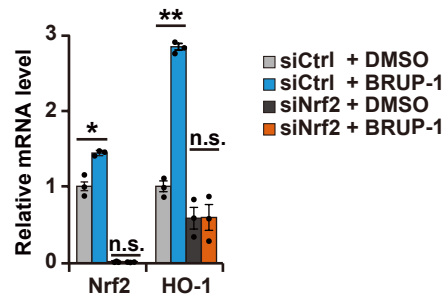
**Figure 2-24.** HepG2 cells transfected with Nrf2 siRNA or control siRNA were treated with 10 $\mu$M BRUP-1 for 12 h followed by qRT-PCR. Data are shown as the mean ± SEM (n = 3). n.s., not significant, *p < 0.05, **p < 0.01(Student's t test).
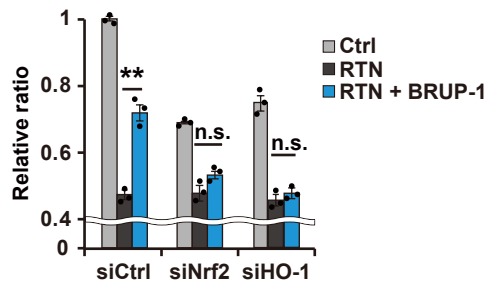


**Figure 2-25.** HepG2 cells stably expressing Flag-UnaG-2A-mCherry were transfected with Nrf2 siRNA, HO-1 siRNA, or control siRNA and then treated with 1 $\mu$M rotenone and/or 10 $\mu$M BRUP-1 for 24 h followed by the intracellular bilirubin assay. Data are shown as the mean ± SEM (n = 3). n.s., not significant, **p < 0.01 (Student's t test).

## 2.2.5. BRUP-1 directly inhibited the Keap1-Nrf2 protein-protein interaction

The activity of Nrf2 is tightly regulated by Keap1, which binds to Nrf2 in the cytosol and facilitates Cullin-mediated poly-ubiquitination of Nrf2, leading to its proteasomal degradation [49]. Because BRUP-1 activated Nrf2, I examined whether BRUP-1 inhibits the Keap1-Nrf2 interaction. I performed BLI-based kinetic analysis using 16mer Nrf2 peptide containing ETGE binding motif within the Nrf2 Neh2 domain which interacted with the Kelch domain of Keap1 [50,51]. As shown in Figure 2-26, Keap1 Kelch domain bound to 16mer Nrf2 peptide, and BRUP-1 inhibited this binding in a dose dependent manner. Initial slopes in the association phase of sensorgrams showed 6.15 $\mu$M BRUP-1 could reduce the initial reaction rate by 50% in this assay (Figure 2-27). These results indicated that BRUP-1 directly inhibited the interaction of Keap1 with Nrf2, leading to Nrf2 activation.
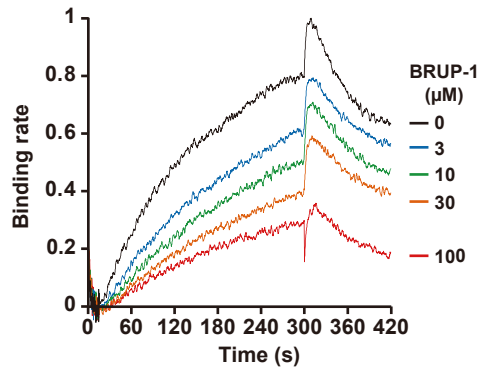
**Figure 2-26.** Sensorgrams of the binding of Keap1 Kelch domain incubated with the indicated concentrations of BRUP-1 to biotin-labeled 16mer Nrf2 peptide for 5 min association followed by dissociation.
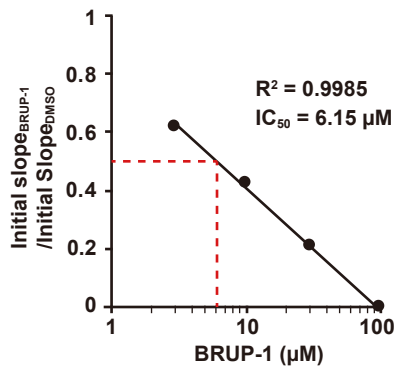


**Figure 2-27.** Plot of the relative ratio calculated by dividing each initial slopes$_{[BRUP-1]}$ by initial slope$_{[DMSO]}$ from 15 to 25 sec in the association phase in Figure 2-26.

**2.2.6. BRUP-1 rescues mitochondrial complex I inhibitor-induced neurotoxicity via**

**HO-1 up-regulation**

Previous reports showed that activation of Nrf2-HO-1 signaling contributes to defense against ROS and ameliorates neuronal cell death in PD models [52-57]. Because BRUP-1 induced the activation of Nrf2-HO-1 signaling, leading to the production of the antioxidant molecule, bilirubin, in HepG2 cells, I next examined whether BRUP-1 showed neuroprotective effects using a PD model cell system. I first confirmed that BRUP-1 induced Nrf2 nuclear translocation and HO-1 up-regulation in nerve growth factor (NGF)-differentiated neuronal PC12D cells (Figure 2-28). Both HO-1 expression and the bilirubin level in culture medium were increased when NGF-differentiated neuronal PC12D cells were treated with $MPP^+$, a well-known dopaminergic neurotoxin which is widely used to create a cellular model of PD. Although BRUP-1 alone failed to increase the bilirubin level in culture medium, I found that HO-1 expression and bilirubin production were further increased by BRUP-1 treatment in these PD model cells (Figure 2-29, 30, 31). Next, I examined whether BRUP-1 rescues neuronal cell death of NGF-differentiated neuronal PC12D cells treated with $MPP^+$ or rotenone. As shown in Figure 2-32 and 33, BRUP-1 effectively suppressed $MPP^+$-induced or rotenone-induced cell death in neuronal PC12D cells. On the other hand, zinc (II) protoporphyrin IX (ZnPP), a HO-1 inhibitor, significantly abrogated this neuroprotective effect of BRUP-1 (Figure 2-34). Involvement of HO-1 in the BRUP-1-mediated neuroprotective effect on PC12D cells was further confirmed in a HO-1 knockdown experiment in which control siRNA- or HO-1 siRNA-transfected PC12D cells were treated with $MPP^+$ in the presence or absence of BRUP-1. As shown in Figure 2-35 and 36, $MPP^+$-induced cell death was

observed in control siRNA- and HO-1 siRNA-transfected PC12D cells to a similar extent. BRUP-1 decreased the percentage of the MPP$^+$-increased subG1 population in control siRNA-transfected PC12D cells, but not in HO-1 siRNA-transfected PC12D cells. These results indicated that BRUP-1 exerted significant neuroprotective effects in this cellular PD model in a HO-1-dependent manner. In addition, although MPP$^+$ induces ROS generation that leads to neuronal cell death, BRUP-1 eliminated this MPP$^+$-mediated ROS production in PC12D cells (Figure 2-37). Also, addition of bilirubin to cell culture medium resulted in significant prevention of MPP$^+$ or rotenone-induced cell death (Figure 2-38). These results suggested that BRUP-1 exhibited neuroprotective effects in MPP$^+$-treated PC12D cells as a PD model through activation of the Nrf2-HO-1-bilirubin antioxidant pathway.

The presence of misfolded and aggregated proteins, which are referred to as Lewy bodies, is one of the hallmarks of PD [58]. Intracellular protein aggregates are nonfunctional, accumulate in the cytoplasm, interfere with normal cellular function, and potentially exert cytotoxicity [59]. Thus, preventing the accumulation of aggregated proteins is considered to be a new therapeutic strategy in PD [60]. Increased oxidative stress has been reported to lead to protein oxidation that is more prone to aggregate [61], I examined whether BRUP-1 protects neuronal cells from protein aggregation by increasing the antioxidant bilirubin level via HO-1 pathway. Aggregated proteins are actively transported to a cytoplasmic juxtanuclear structure called the aggresome. In neuronal PC12D cells, aggresomes formed following MPP$^+$ treatment for 24 h, and this MPP$^+$-mediated aggresome formation was significantly inhibited by BRUP-1 (Figure 2-39). I next examined the possible involvement of the Nrf2-HO-1-bilirubin pathway in suppression of MPP$^+$-induced aggresome formation by BRUP-1. As shown in Figure 2-

40, MPP$^+$ treatment of HO-1 knocked down neuronal PC12D cells also induced formation of aggresomes, but BRUP-1 failed to inhibit MPP$^+$-induced aggresome formation, indicating that activation of the Nrf2-HO-1-bilirubin antioxidant pathway by BRUP-1 suppressed MPP$^+$-induced aggresome formation in neuronal PC12D cells.
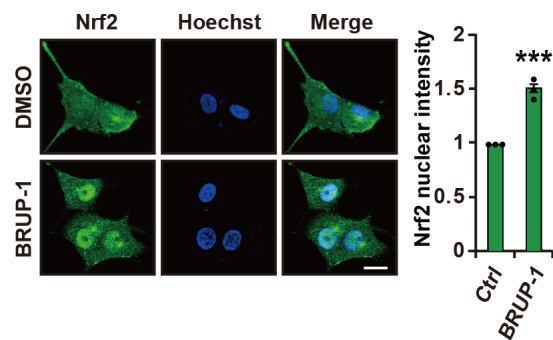


**Figure 2-28.** NGF-differentiated PC12D cells were treated with 10 $\mu$M BRUP-1 for 3 h and then subjected to immunofluorescence analysis with anti-Nrf2 antibody. The scale bar represents 10 $\mu$m. Data are shown as the mean ± SEM (n = 3). ***p < 0.001 (Student's t test).
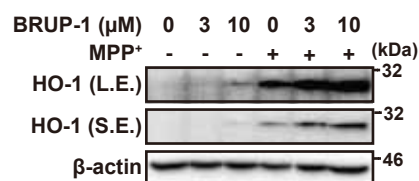


**Figure 2-29.** NGF-differentiated PC12D cells were treated with the indicated concentrations of BRUP-1 in the presence or absence of 0.3 mM MPP$^+$ for 24 h followed by western blotting analysis.
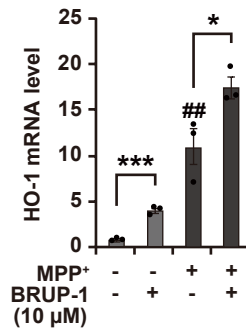
**Figure 2-30.** NGF-differentiated PC12D cells were treated with the indicated concentrations of BRUP-1 in the presence or absence of 0.3 mM MPP$^+$ for 12 h followed by qRT-PCR. Data are shown as the mean ± SEM (n = 3). $^{\#\#}p < 0.01$ (relative to untreated cells, Tukey's test), $^*p < 0.05$, $^{***}p < 0.001$ (Student's t test).
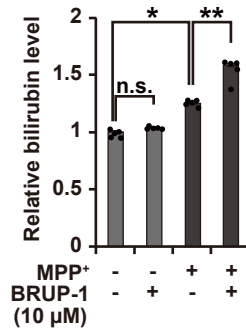


**Figure 2-31.** NGF-differentiated PC12D cells were treated with the indicated concentrations of BRUP-1 in the presence or absence of 0.3 mM MPP$^+$ for 24 h followed by the *in vitro* bilirubin assay. Data are shown as the mean ± SEM (n = 5). n.s., not significant, $^*p < 0.05$, $^{**}p < 0.01$ (Tukey's test).
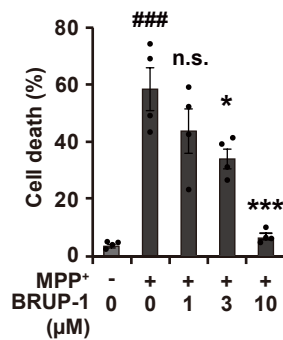
**Figure 2-32.** NGF-differentiated PC12D cells were treated with BRUP-1 and 0.3 mM MPP⁺ for 48 h followed by the cell death assay. Data are shown as the mean ± SEM (n = 4). $^{###}p < 0.001$ (relative to untreated cells), n.s., not significant, $^*p < 0.05$, $^{***}p < 0.001$ (Tukey's test).
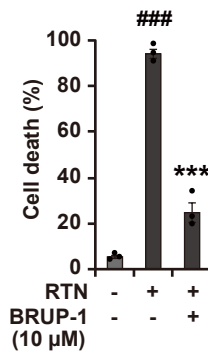


**Figure 2-33.** NGF-differentiated PC12D cells were treated with BRUP-1 and 0.3 $\mu$M rotenone for 48 h followed by the cell death assay. Data are shown as the mean ± SEM (n = 3). $^{###}p < 0.001$ (relative to untreated cells), $^{***}p < 0.001$ (Tukey's test).
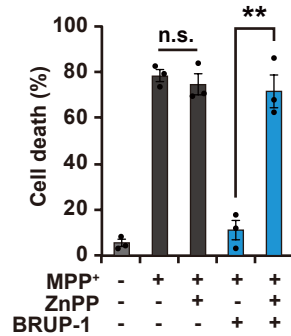
**Figure 2-34.** NGF-differentiated PC12D cells were treated with 10 $\mu$M BRUP-1 and 0.3 mM MPP$^+$ in the presence or absence of 10 $\mu$M ZnPP for 48 h followed by the cell death assay. Data are shown as the mean ± SEM (n = 3). n.s., not significant, **p < 0.01 (Student's t test).
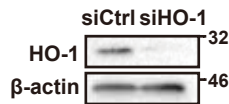


**Figure 2-35.** Knockdown of HO-1 in NGF-differentiated PC12D cells was confirmed with western blotting.
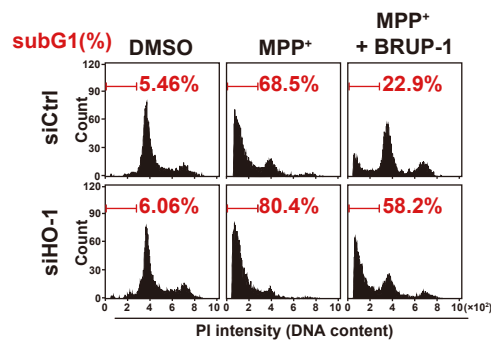


**Figure 2-36.** NGF-differentiated PC12D cells transfected with HO-1 siRNA or control siRNA were treated with 10 $\mu$M BRUP-1 and 0.3 mM MPP$^+$ for 48 h followed by the cell death assay.
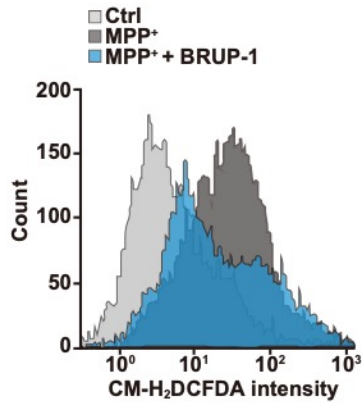
**Figure 2-37.** NGF-differentiated PC12D cells were treated with 10 $\mu$M BRUP-1 and 0.3 mM MPP$^+$ for 24 h followed by ROS measurement.
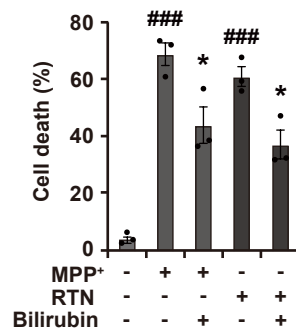


**Figure 2-38.** NGF-differentiated PC12D cells were treated with freshly prepared 250 nM bilirubin and 0.3 mM MPP+ or 0.1 $\mu$M rotenone for 48 h followed by the cell death assay. Data are shown as the mean ± SEM (n = 3). $^{###}$p < 0.001 (relative to untreated cells, Tukey's test), *p < 0.05 (Student's t test).
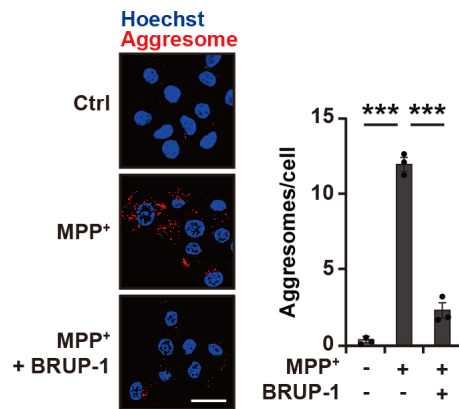
**Figure 2-39.** NGF-differentiated PC12D cells were treated with 10 $\mu$M BRUP-1 and 0.3 mM MPP$^+$ for 24 h followed by aggresome staining and confocal microscopy. The scale bar represents 20 $\mu$m. Data are shown as the mean ± SEM (n = 3). ***p < 0.001 (Tukey's test).
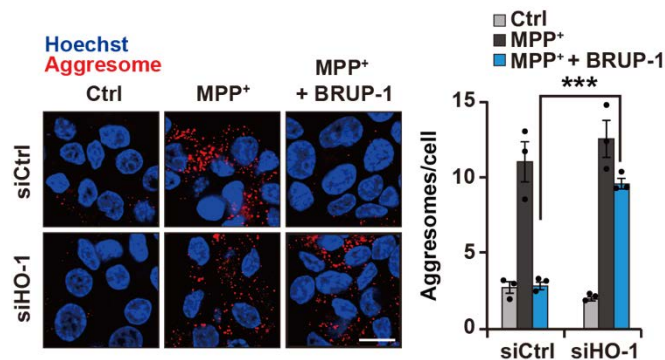


**Figure 2-40.** NGF-differentiated PC12D cells transfected with HO-1 siRNA or control siRNA were treated with 10 $\mu$M BRUP-1 and 0.3 mM MPP$^+$ for 24 h followed by aggresome staining and confocal microscopy. The scale bar represents 10 $\mu$m. Data are shown as the mean ± SEM (n = 3). ***p < 0.001 (Student's t test).

## 2.3. Discussion

In this study, I conducted screening for possible drugs that target bilirubin metabolism for treatment of PD. For this, I first established a cell system that can be used to easily measure the amount of intracellular bilirubin, and I developed a Flag-UnaG-2A-mCherry probe, which expresses two different reporters via ribosomal skipping at the 2A viral sequencing site [40]. Using this probe, the change in the intracellular bilirubin level can be evaluated simply by determining the UnaG/mCherry signal intensity ratio. Bilirubin is metabolized mainly in the liver and spleen [62], and rapid degradation of newly synthesized heme to bilirubin is observed in isolated hepatocytes [38]. Therefore, I established a bilirubin detection system using human hepatocellular carcinoma HepG2 cells to obtain adequate UnaG signal intensity. Indeed, green fluorescence of UnaG in HepG2 cells that stably expressed this probe was easily detected using a fluorescence microscope or microplate reader. To validate this bilirubin assay system, I confirmed that exposure of cells to bilirubin or its precursor, biliverdin, increased the UnaG/mCherry ratio. Interestingly, the mitochondrial complex I inhibitor, rotenone, which is widely used to induce the cardinal symptoms of PD in animal models [15], obviously decreased the intracellular bilirubin level, indicating that the UnaG-2A-mCherry-expressing cell system that I established reflects the finding that serum levels of bilirubin are significantly lower in PD patients [34]. This bilirubin depletion by rotenone was due to down-regulation of HO-1 at the transcription level [42] in HepG2 cells. Although repression of the gene encoding HO-1 is largely affected by the heme-regulated protein, Bach1 [63-65], at present I do not know whether Bach1 is related to rotenone-induced repression of HO-1 expression in HepG2 cells.

In the course of screening for compounds that restore the rotenone-decreased

intracellular bilirubin level using HepG2 cells expressing Flag-UnaG-2A-mCherry, I discovered that BRUP-1 restored the intracellular bilirubin level. BRUP-1 is a commercially available compound, and so far, no biological activity for BRUP-1 has been reported. BRUP-1 also restored rotenone-reduced expression of HO-1 at the transcriptional level. HO-1 expression is mainly regulated at the transcriptional level, and different cis-acting regulatory elements are associated with the expression level of the HO-1 gene [47]. Although several intracellular signaling molecules regulate HO-1 expression, such as mitogen-activated protein kinase (MAPK), phosphatidylinositol 3-kinase (PI3K), tyrosine kinase, activator protein-1 (AP-1), and nuclear factor-κB (NF-κB) [66], HO-1 expression is strongly potentiated by binding of the Nrf2 transcription factor to the antioxidant response element in the HO-1 gene [67]. Indeed, BRUP-1 treatment significantly stimulates nuclear translocation of Nrf2, indicating activation of Nrf2, and subsequently induces the expression of HO-1 [68], leading to elevation of intracellular bilirubin levels.

The most well-known modulator of Nrf2 activity is Keap1, which binds to Nrf2 in the cytosol and facilitates Cullin-mediated poly-ubiquitination of Nrf2, leading to its proteasomal degradation [49]. Human Keap1 is a 69-kDa protein that contains five domains: (i) the N-terminal region; (ii) the Broad complex, Tramtrack, and Bric-a-Brac; (iii) the linker intervening region; (iv) the Kelch domain; and (v) the C-terminal region. In the intervening region domain, 27 cysteine residues have been identified that are sensitive to oxidation and the nuclear export signal motif. Some of these cysteines are essential for Keap1-dependent ubiquitination of Nrf2 and Keap1-mediated repression of Nrf2 activity [69,70]. The Kelch domain interacts with the Neh2 domain of Nrf2.

I found that BRUP-1 inhibited the interaction between the Kelch domain of

Keap1 and the Neh2 domain of Nrf2. Many small molecules that activate Nrf2 have been identified, and most of them inhibit the Keap1-Nrf2 interaction by forming covalent adducts with the sulfhydryl groups of cysteines in Keap1 via oxidation or alkylation [71]. Structurally, BRUP-1 does not seem to modify the sulfhydryl groups of cysteine residues in the Kelch domain of Keap1. Over the past several years, non-covalent small molecule activators of Nrf2, which inhibit the Keap1 kelch-Nrf2 interaction, have been reported [72]. Inhibitors of Keap1-Nrf2 interaction are now in clinical development and are expected to provide cytoprotection against numerous pathologies including chronic diseases of the lung and liver; autoimmune, neurodegenerative and metabolic disorders; and cancer initiation [73]. BRUP-1 is a new member of Nrf2 activators by inhibiting the Keap1-Nrf2 interaction, obtained from the phenotypic screening, therefore, BRUP-1 may have potential not only for PD but also for diverse pathologies treatment.

In contrast to HepG2, treatment of NGF-differentiated PC12D cells with MPP$^+$ induced an increase in the expression of HO-1, leading to an increased level of bilirubin. These results using a PD model cell system closely reflect the previously reported findings that cytoplasmic Lewy bodies within affected dopaminergic neurons of the PD substantia nigra exhibit prominent HO-1 immunoreactivity [74,75]. In addition, Nrf2 activation is observed in the substantia nigra of PD patients [76]. Activation of the Nrf2-HO-1 pathway in the PD brain can be explained as a consequence of activation of the cellular defense mechanism that protects against oxidative stress [77]. Therefore, further activation of the Nrf2-HO-1 pathway was expected to protect PD model cells from neuronal cell death. BRUP-1 induced Nrf2 nuclear translocation and subsequent HO-1 upregulation in PC12D cells. Although this HO-1 upregulation by BRUP-1 was not sufficient to increase the extracellular bilirubin level, BRUP-1 potentiated the increase of

HO-1 expression level and bilirubin production by MPP$^+$ treatment. It would be interesting to understand why BRUP-1 alone did not result in significant increase of bilirubin production, while it potentiated the effect of MPP$^+$ in neuronal cells. One possibility is that HO-1 induction by MPP$^+$ treatment is caused via Nrf2-dependent and Nrf2 independent pathway such as MAPK, AP-1, and NF-κB signaling [66].

Nevertheless, BRUP-1 treatment could lead to the suppression of MPP$^+$-induced both ROS generation and cell death in neuronal PC12D cells. Innamorato *et al*. reported that the dopaminergic neurodegeneration by MPTP injection was exacerbated in Nrf2-knockout mice but not changed in HO-1 knockout mice [78]. Also, Nrf2 activation is expected to up-regulate not only HO-1 but also other key antioxidative genes including glutathione S-transferase (GST), NAD(P)H oxidoreductase (NQO1), and glutamate-cysteine ligase (GCL) [46]. However, neuroprotective activity of BRUP-1 was strongly abrogated by HO-1 silencing or chemical inhibition in MPP$^+$-treated PC12D cells. In addition, exogenous bilirubin supplementation significantly suppressed neuronal cell death. These results suggested that BRUP-1 exerted neuroprotective activity through activation of the Nrf2-HO-1-bilirubin pathway in PC12D cells.

Accumulation of misfolded proteins in inclusions is a prominent pathological feature common to many age-related neurodegenerative diseases, including PD. In cultured cells, when the production of misfolded proteins exceeds the capacity of mechanisms to clear these proteins, including suppression of aggregate formation by molecular chaperones and degradation of misfolded proteins by proteasomes, misfolded proteins are actively transported to a cytoplasmic juxtanuclear structure called an aggresome. Characterization of the molecular mechanisms underlying aggresome formation and its regulation has begun to provide promising therapeutic targets that may

be relevant to neurodegenerative diseases. Although abundant evidence indicates that aggresome formation is a cytoprotective response [79-82], compounds that inhibit early steps in the pathway of aggresome formation are expected to lead to lower levels of toxic protein species. I found that MPP$^+$ treatment significantly increased aggresome formation in NGF-differentiated neuronal PC12D cells, and BRUP-1 completely inhibited MPP$^+$-induced aggresome formation. Inhibition of MPP$^+$-induced aggresome formation by BRUP-1 was blocked when HO-1 was knocked down in neuronal PC12D cells. Considering that increased oxidative stress leads to protein oxidation that is more prone to aggregate [61], BRUP-1 inhibited MPP$^+$-induced aggresome formation possibly due to activation of the Nrf2-HO-1-bilirubin antioxidant pathway. Therefore, BRUP-1 may be beneficial by reducing cytotoxicity in various diseases characterized by accumulation of aggregated proteins. However, further investigation of the mechanisms of aggresome formation and the mode of action of BRUP-1 is required.

Notably, the neuroprotective effect of BRUP-1 on iPSC-derived neurons were tested by measuring cleaved caspase-3, an apoptosis marker, by Dr. Kei-ichi Ishikawa and Dr. Wado Akamatsu at Juntendo University. As a result, BRUP-1 significantly suppressed caspase-3 cleavage mediated by rotenone treatment in iPSC-derived neurons established from two independent individuals [83].

Thus, BRUP-1 showed potent neuroprotective effect in neuron-like cells, however, other cell types of the brain parenchyma, such as microglia and astroglia, also play a role in PD. Chronic release of proinflammatory cytokines by activated astrocytes and microglia leads to the exacerbation of dopaminergic neuron degeneration [84]. Considering that oxidative stress leads to prominent activation of microglia, BRUP-1 may reduce neuroinflammation activated by microglia through ROS suppression. Further

investigations using animal models for PD are required to understand the effect of BRUP-1 on neurons and other cell types of the brain parenchyma.

Recently, it has been reported that bilirubin's redox activity is particularly important in the brain and may underlie a prominent physiologic role despite being significantly less abundant than other endogenous and exogenous antioxidants [85]. Taken together with my results, activation of the heme redox pathway using BRUP-1 may be a new therapeutic approach in PD.

## 2.4. Materials and methods

### Reagents and antibodies

Rotenone (Cat #: R8875), Bilirubin (Cat #: B4126), Biliverdin (Cat #: 30891), zinc (II) protoporphyrin IX (ZnPP, Cat #: 282820), and MPP$^+$ (Cat #: D048) were purchased from Sigma. Nerve growth factor (NGF) 2.5S (Cat #: N-100) was purchased from Alomone Labs. BRUP-1 was purchased from Enamine (Cat #: EN300-6759210, CAS No. 726164-66-5). Biotin-labeled 16mer Nrf2 peptide AFFAQLQLDEETGEF was purchased from Scrum. His-tagged human Keap1 (321-609 a.a., Cat #: 70040) was purchased from BPS Bioscience. The following antibodies were used: anti-β-actin (Cat #: A1978), anti-Flag M2 (Cat #: F1804) from Sigma; anti-mCherry (Cat #: 632543) from Clontech; anti-HO-1 (Cat #: ab13248), anti-Nrf2 (Cat #: ab137550) from Abcam; anti-p62 (Cat #: 5114) from Cell Signaling Technology. Bilirubin, Biliverdin, ZnPP, and BRUP-1 were dissolved in DMSO. Rotenone was dissolved in ethanol. MPP$^+$ was dissolved in pure water. Bilirubin and Biliverdin were freshly prepared immediately prior to each experiment. Equal concentrations of solvent were added to each group to exclude solvent effects.

### Cell culture

Human hepatocellular carcinoma HepG2 cells (purchased from American Type Culture Collection) were cultured in Dulbecco's modified Eagle medium (DMEM) supplemented with 10% fetal bovine serum, 0.6 mg/mL L-glutamine, 100 U/mL penicillin G, and 0.1 mg/mL kanamycin at 37ºC in 5% $CO_2$. Rat adrenal pheochromocytoma PC12D cells (provided from Dr. Kazuo Umezawa at Keio University) were cultured in DMEM supplemented with 5% fetal bovine serum, 10% horse serum, 0.6 mg/mL L-glutamine,

and antibiotics. PC12D cells were differentiated by adding 100 ng/mL NGF and incubated for 72 h before drug treatment.

**Plasmid construction**

To generate a plasmid vector containing 2A-linked UnaG and mCherry, I first amplified UnaG and mCherry with PCR using pcDNA3-Flag/UnaG and pmCherry-N1, respectively, as templates and the following primers (5′-3′): UnaG-2A forward, GAGC-TCGGATCCATGGTCGAGAAATTTGTT; UnaG-2A reverse, GTCTCCTGCTTGCTT-TAACAGAGAGAAGTTCGTGGCTTCCG-TCGCCCTCCGGTA; 2A-mCherry forward, GCCACGAACTTCTCTCTGTTAAAGCAAGCAGGAGACGTGGAAGAA-AACCCCGGTCCTATG; 2A-mCherry reverse, TCTGCAGAATTCCTACTTGTACAG-CTCGTC. Subsequently, recombinant PCR was performed with purified amplicons of UnaG and mCherry as templates and external primers (UnaG-2A forward and 2A-mCherry reverse). The UnaG-2A-mCherry construct was then cloned into the BamHI and EcoRI sites of pcDNA3-flag. To generate the His-tagged UnaG plasmid vector, UnaG cDNA was amplified using the following primers (5′-3′): UnaG forward, GGAT-GGATCCGAATGGTCGAGAAATTTGTT; UnaG reverse, GTCGAATTCTATCATTC-CGTCGCCCTCCG. Subsequently, the UnaG amplicon was inserted into the BamHI and EcoRI sites of pRSETC. HO-1 cDNA was amplified with PCR from a cDNA library derived from HepG2 cells and the following primers (5′-3′): forward, GTATCG-GGATCCCGATGGAGCGTCCGCAAC; reverse, GGCTTTATGCCATG. HO-1 cDNA was then cloned into the BamHI and EcoRI sites of pcDNA3.1-hygro.

**Plasmid transfection**

HepG2 cells stably expressing UnaG-2A-mCherry or HO-1 were established

with plasmid transfection using Lipofectamine3000 (Invitrogen) according to the manufacturer's protocol. Forty-eight hours after the transfection, cells were selected with 0.8 mg/mL G418 (Wako) or 0.3 mg/mL hygromycin B (Wako) for 2 weeks followed by single-cell cloning.

**siRNA transfection**

Stealth siRNAs against HO-1 (HSS142462) and Nrf2 (HSS181505), and negative control siRNAs (12935300) were purchased from Invitrogen. Cells were transfected with 50 nM siRNA using Lipofectamine RNAiMAX (Invitrogen) for 48 or 72 h.

**Intracellular bilirubin assay**

HepG2/UnaG-2A-mCherry cells were seeded into a 96-well black plate. Twenty-four hours after seeding, medium was changed to OPTI-MEM (Gibco) containing 5 mg/mL bovine serum albumin (BSA). Subsequently, cells were treated with compounds for 24 h or the indicated time. Then cells were washed with phosphate-buffered saline (PBS), and then fluorescence of UnaG and mCherry was detected using a fluorescence microscope (IX71 with cellSens software, Olympus) or a microplate reader (SAFIRE, TECAN).

***in vitro* bilirubin assay**

Cells were seeded into a 60-mm dish. Twenty-four hours after seeding, medium was replaced with OPTI-MEM containing 5 mg/mL BSA. Subsequently, cells were treated with compounds for 24 h. Then 1 mL medium was collected and incubated with 2 $\mu$g His-UnaG recombinant protein for 1 h. The His-UnaG-bilirubin complex was purified using Ni-NTA agarose beads and eluted with 250 mM imidazole solution.

Fluorescence intensity of UnaG was measured using a microplate reader (SAFIRE, TECAN).

**Chemical screening**

The chemical library consisted of 9,600 compounds (Core library) and was supplied by the Drug Discovery Initiative (University of Tokyo). I performed the intracellular bilirubin assay using 10 $\mu$M each compound with 1 $\mu$M rotenone. In each plate, I confirmed that the Z'-factor was over 0.5 for assay validation. The inhibition rate was calculated by setting the average of eight independent wells of DMSO-treated cells at 1 and rotenone-treated cells at 0.

**Western blotting analysis**

Cells were lysed with RIPA buffer (pH 7.8, 25 mM HEPES, 1.5% Triton X-100, 1% sodium deoxycholate, 0.1% SDS, 0.5 M NaCl, 5 mM EDTA, 50 mM NaF, 100 mM Na3VO4, and protease inhibitor cocktail (Roche)). Equal amounts of protein were separated with SDS-PAGE and transferred onto PVDF membranes, which were incubated with primary antibodies (1:1000) overnight at 4ºC. HRP-conjugated secondary antibodies (GE Healthcare) were all used at 1:5000 for 1 h at room temperature (RT). Chemiluminescence detection was achieved using an Immobilon Western Kit (Merck Millipore) and ChemiDoc XRS+ (BioRad). Quantification of blots was performed using Image Lab software (BioRad).

**RNA extraction and quantitative RT-PCR**

Total RNA was extracted using the RNeasy Mini Kit (Qiagen). Total RNA (2 $\mu$g) was reverse transcribed using MMLV Reverse Transcriptase (Promega) according to the manufacturer's instructions. Quantitative PCR was performed on a Thermal

Cycler Dice (Takara) using SYBR Premix Ex Taq (Takara). mRNA levels were determined with the $\Delta\Delta$Ct method and normalized to *GAPDH* or *β-actin* levels. The primer sequences are as follows (5′-3′). *HO-1*: forward, GGAGATTGAGCGCAACAA-GG; reverse, CTGCATGGCTGGTGTGTAGG. *Nrf2*: forward, CAGCGACGGAAAG-AGTATGA; reverse, TGGGCAACCTGGGAGTAG. *GAPDH*: forward, AGGTCGGA-GTCAACGGATTT; reverse, TAGTTGAGGTCAATGAAGGG. Rat *Ho-1*: forward, GCCTGCTAGCCTGGTTCAAG; reverse, AGCGGTGTCTGGGATGAACTA. Rat *β-actin*: forward, CCTCTGAACCCTAAGGCCAA; reverse, GCCTGGATGGCTACGT-ACA.

**Immunofluorescence**

Cells seeded on coverslips (Matsunami) were fixed with 3% paraformaldehyde in PBS for 15 min, permeabilized with 0.1% Triton X-100, 1% BSA for 30 min, and blocked with 1% BSA in PBS with 0.05% Tween-20 (PBS-Tween) for 60 min. The primary antibody for Nrf2 (1:500) was added, and cells were incubated overnight at 4℃. After three washes using PBS-Tween, cells were incubated with the anti-rabbit IgG secondary antibody, Alexa Fluor 488 (Invitrogen) for 2 h at RT. Cells were then washed three times and stained with 2 $\mu$g/mL Hoechst33342 (Invitrogen) for 30 min at RT. The coverslips were mounted onto glass slides in 50% glycerol in PBS. Images were acquired using a confocal laser scanning microscope system (FV1000, Olympus), and signal intensity of Nrf2 in nuclei was analyzed using Fiji software.

**BLI-based Keap1-Nrf2 binding assay**

Keap1-Nrf2 binding assay was performed at 30℃ using an Octet K2 system (ForteBio). Kinetics buffer consisted of 0.01% BSA and 0.002% Tween-20 in PBS (pH

7.4) were used as the matrix throughout. For the kinetic assay, 5 nM Keap1 Kelch domain incubated with DMSO or BRUP-1 for 30 min was interacted with 10 nM biotin-labeled Nrf2 16mer peptide immobilized as the ligand on a streptavidin sensor chip (ForteBio) for 5 min.

**Cell death assay**

To determine the percentage of cell death, cell cycle analysis was performed as previously described [86,87]. In brief, NGF-differentiated PC12D cells treated with compounds for 48 h were harvested and fixed with ice-cold 70% ethanol for at least 1 h at 4°C. Cells were then incubated with RNase/PBS and stained with 50 $\mu$g/mL propidium iodide solution. Propidium iodide fluorescence intensity was measured with flow cytometry (Epics XL, Beckman Coulter), and the percentage of dead cells was determined by quantitating the subG1 population.

**Intracellular reactive oxygen species (ROS) detection**

NGF-differentiated PC12D cells were treated with 0.3 mM $MPP^+$ and 10 $\mu$M BRUP-1 for 24 h. Cells were then harvested and stained with 2 $\mu$M CM-H2DCFDA (Invitrogen) according to the manufacturer's instructions. The relative fluorescence levels were quantified using a flow cytometer (BD accuri C6).

**Aggresome formation assay**

NGF-differentiated PC12D cells seeded on coverslips were fixed with 3% paraformaldehyde in PBS for 15 min, permeabilized with 0.3% Triton X-100, 1% BSA for 30 min, and blocked with 1% BSA in PBS-Tween for 60 min. Aggresome staining was then performed using the Proteostat Aggresome Detection Kit (Enzo Life Sciences) according to the manufacturer's instructions. Sample preparation and confocal

microscopy were performed as described above. The number of aggresome dots per cell in each image was quantified using Fiji software.

**Statistical analyses**

All data are presented as the mean ± standard error of the mean (SEM) unless otherwise stated. Statistical analyses were performed with the paired t-test for two groups or one-way analysis of variance followed by Tukey's test or Dunnett's test for multiple groups using SPSS statistics ver.24 (IBM) software.

# Chapter 3

# A chemical genomics-aggrephagy integrated method studying functional analysis of autophagy inducers

## 3.1. Introduction

Autophagy, an intracellular degradation system for recycling damaged organelles and removing aggregated proteins via lysosomes, is an essential process that maintains cellular homeostasis [88]. Given that impairment of autophagy has been implicated in various diseases such as cancer, infections, and neurodegenerative disease [89], stimulating autophagy by small-molecule chemical compounds has been proposed as a therapeutic intervention [90]. While many autophagy inducers have been identified so far, their mechanisms of autophagy induction remain (in some cases) poorly understood, probably because of the highly diversified and complicated crosstalk among autophagy signaling pathways, which include both mammalian target of rapamycin (mTOR)-dependent and -independent processes [91].

mTOR inhibitors such as Rapamycin and Torin1 are the best-understood autophagy inducers. The mTOR complex 1 (mTORC1) negatively regulates autophagy by phosphorylating the unc-51 like autophagy activating kinase 1 (ULK1) required for autophagosome formation [92] and transcription factor EB (TFEB) known as a master regulator of autophagy/lysosome gene expression [93]. Inhibitors that act upstream of mTOR including Akt and p53; activators that act downstream of mTOR are expected to be inducers of autophagy. On the other hand, small molecules that modulate the inositol, $Ca^{2+}$-calpain, cAMP, or Beclin-1 signaling pathways activate autophagy in an mTOR-independent manner. In addition, activators of TFEB or other transcription factors that are involved in the expression of autophagy genes, such as those encoding the forkhead-box proteins FoxO1 and FoxO3, also are capable of inducing autophagy [94]. Inducers of endoplasmic reticulum (ER) stress also have been implicated in the activation of autophagy through the ER stress response, including effects mediated primarily via

inositol-requiring kinase 1 alpha (IRE1$\alpha$) and PKR-like ER kinase (PERK) signaling [95].

Thus, autophagy activation by small molecules can be achieved via various pathways, which complicates the analysis of their mechanisms of action. To address this issue, I performed chemical genomic analyses to classify autophagy inducers and facilitate characterization of the autophagy induction mechanism. Magi *et al*. previously demonstrated that cell migration can be controlled by diverse signaling pathways [96]; in that work, the authors used chemical signal transduction modulators as probes to inhibit target protein activity, rather than employing gene silencing. That approach is easily applicable in autophagy research because the strategy only requires adding signal modulators into cell culture medium with autophagy inducers at any desired time point.

In the present study, I firstly conducted a chemical screen and identified 39 compounds as autophagy inducers in neuronal PC12D cells. I then examined the autophagy profile of each of 26 autophagy inducers by chemical genomics. Multiple distinct autophagy profiles were observed. These were subjected to principal component analysis (PCA) and clustering analysis to infer the mechanism of action of chemical compounds that induce autophagy by unknown mechanisms. Based on my clustering analysis, I identified the mechanism underlying autophagy activation induced by two Food and Drug Administration (FDA)-approved drugs, Memantine and Clemastine, whose autophagy induction mechanism previously was not understood. In addition, I used my PCA to identify SMK-17, a recently identified MEK1/2 inhibitor, as a novel autophagy inducer, and further evaluated this compound's mechanism of autophagy activation. Through these studies, I demonstrated that a chemical genomic approach may be useful for inferring the mode of action of chemical autophagy inducers. Finally, I examined the effect of 26 autophagy inducers on protein aggregation (i.e., the clearance

of aggresomes), a hallmark of neurodegenerative disorders [60], using a cellular model of Parkinson's disease (PD), demonstrating a contrast to the effects of antioxidants. I showed the superiority of autophagy inducers in removing cytotoxic protein aggregates, which are commonly observed in neurodegenerative disorders including PD and Huntington's disease (HD).

## 3.2. Results

### 3.2.1. Screening of autophagy inducers using a GFP-LC3-RFP autophagy probe in neuronal PC12D cells

Autophagy flux can be evaluated simply by measuring GFP/RFP signal intensity ratio, using a GFP-LC3-RFP probe that produces equal amounts of GFP-LC3 as the autophagy marker (by degradation during the progression of autophagy) and RFP as an internal expression control [97]. I first generated PC12D stably expressing this probe by high-titer retroviral transduction followed by FACS to obtain comparably fluorescent cells (Figure 3-1). To validate the utility of the transduced cells as reporters of autophagy, I confirmed that (a) exposure of the cell to the known autophagy inducers Rapamycin and Torin1 yielded a decreased GFP/RFP ratio (Figure 3-2) and (b) exposure to the known autophagy inhibitor Bafilomycin A1 yielded an increased GFP/RFP ratio (Figure 3-3). I then screened ~ 400 compounds, primarily from SCADS inhibitor kits (I-IV) consisting of target-identified small molecules, to identify autophagy inducers (Figure 3-4, 5). Following re-evaluation of the top 50 compounds recovered in the 1st screen, I identified 39 compounds that significantly induced autophagy in neuronal PC12D cells (Figure 3-6, Table 1, 2). While 38 of these 39 compounds previously have been reported as autophagy inducers, one (SMK-17) appears to constitute a novel autophagy inducer. Among the 39 autophagy inducers, I selected 26 compounds as non-cytotoxic autophagy inducers (above 80% cell viability, Figure 3-7) for further investigation.
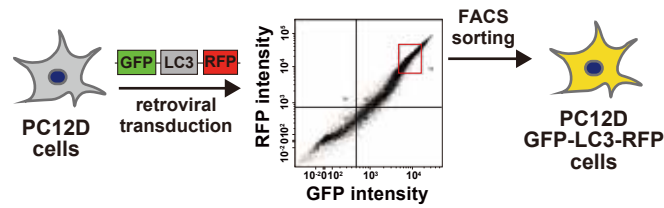
**Figure 3-1.** Schematic illustration of establishment of PC12D cells stably expressing GFP-LC3-RFP autophagy flux probe.
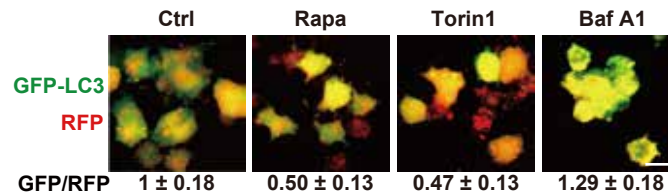


**Figure 3-2.** PC12D cells expressing GFP-LC3-RFP were treated with 10 $\mu$M Rapamycin (Rapa), 100 nM Torin1, or 10 nM Bafilomycin A1 (Baf A1) for 24 h. The scale bar represents 20 $\mu$m. Data are shown as mean ± SD (n=3).
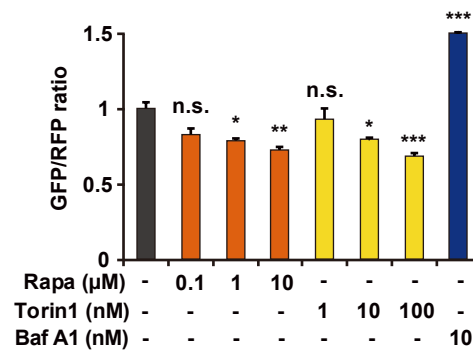


**Figure 3-3.** PC12D cells expressing GFP-LC3-RFP were treated with the indicated concentrations of Rapamycin, Torin1, or Bafilomycin A1 for 24 h. The GFP/RFP fluorescence intensity ratio was measured using a high-content imager. Data are shown as mean ± SD (n=3). n.s., non-significant, *$p < 0.05$, **$p < 0.01$, ***$p < 0.001$ (Dunnett's test).
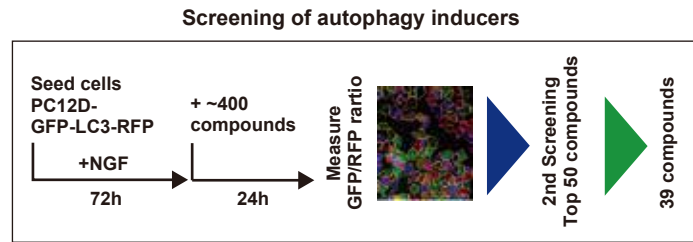
**Figure 3-4.** Schematic illustration of the chemical screen.
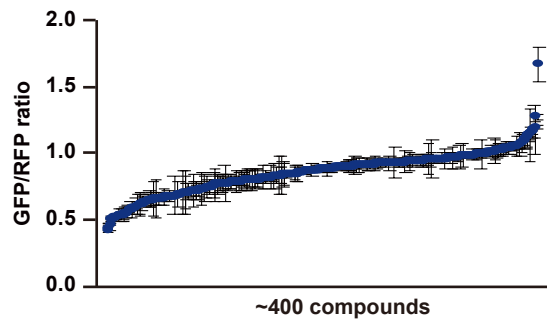


**Figure 3-5.** Scatter plot of the GFP/RFP ratio of each compound in the screen. Data are shown as mean ± SD (n=3).
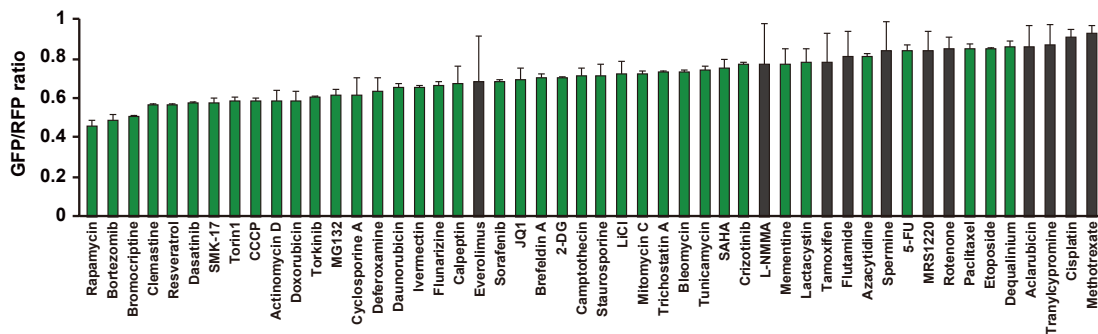


**Figure 3-6.** Bar graph showing the GFP/RFP ratios of the top 50 compounds. Green bars indicate compounds that significantly induced autophagy (p < 0.05, Student's t test compared to control). Data are shown as mean ± SD (n=3).
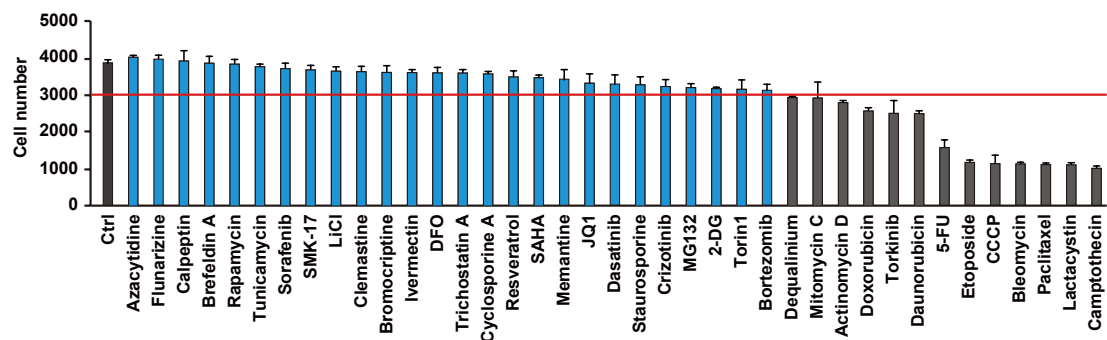
**Figure 3-7.** Cytotoxicity of the autophagy inducers in neuronal PC12D cells. Cell number quantification using a high-content imager in PC12D cells expressing GFP-LC3-RFP in the same condition as Figure 3-6. Blue bars indicate compounds considered as non-cytotoxic autophagy inducers (above 80% cell viability; red line).

**Table 1.** Autophagy inducers used in this study.

| Compound | Concentration | Target | Reference |
|---|---|---|---|
| 2-Deoxyglucose (2-DG) | 10 mM | glycolysis | [98] |
| Azacytidine | 10 $\mu$M | DNA methyltransferase | [99] |
| Bortezomib | 100 nM | proteasome | [100] |
| Brefeldin A | 500 nM | COP-I complex | [101] |
| Bromocriptine | 10 $\mu$M | dopamine receptor agonist | [102] |
| Calpeptin | 50 $\mu$M | calpain | [91] |
| Clemastine | 5 $\mu$M | histamine H1 antagonist | [103] |
| Crizotinib | 5 $\mu$M | tyrosine kinase | [104] |
| Cyclosporine A | 5 $\mu$M | immunosuppressant | [105] |
| Dasatinib | 10 $\mu$M | tyrosine kinase | [106] |
| Deferoxamine (DFO) | 100 $\mu$M | iron chelator | [107] |
| Flunarizine | 20 $\mu$M | calcium antagonist | [108] |
| Ivermectin | 10 $\mu$M | anti-parasite medication | [109] |
| JQ1 | 1 $\mu$M | bromodomain containing 4 (BRD4) | [110] |
| LiCl | 50 mM | glycogen synthase kinase 3 | [111] |
| Memantine | 100 $\mu$M | NMDA receptor antagonist | [112] |
| MG132 | 5 $\mu$M | proteasome | [113] |
| Rapamycin | 10 $\mu$M | mTORC1 | [114] |
| Resveratrol | 100 $\mu$M | polyphenol, Sirtuin 1 activator | [115] |
| SAHA | 3 $\mu$M | histone deacetylase (HDAC) | [116] |
| SMK-17 | 10 $\mu$M | MEK1/2 | [117] |
| Sorafenib | 2 $\mu$M | protein kinase | [118] |
| Staurosporine | 10 nM | protein kinase | [119] |
| Torin1 | 100 nM | mTORC1, 2 | [120] |
| Trichostatin A | 1 $\mu$M | histone deacetylase (HDAC) | [121] |
| Tunicamycin | 2 $\mu$M | N-linked glycosylation (ER stress) | [122] |

**Table 2.** Autophagy inducers identified in this study (excluded from Table 1).

| Compound | Concentration | Target | Reference |
|---|---|---|---|
| 5-FU | 5 µM | thymidylate synthetase | [123] |
| Actinomycin D | 10 nM | RNA synthesis | [124] |
| Bleomycin | 5 µM | DNA synthesis | [125] |
| Camptothecin | 100 nM | DNA synthesis | [126] |
| CCCP | 10 µM | protonophore | [127] |
| Daunorubicin | 100 nM | DNA synthesis | [128] |
| Dequalinium | 1 µM | $K^+$ channel | [97] |
| Doxorubicin | 100 nM | DNA synthesis | [129] |
| Etoposide | 1 µM | DNA synthesis | [130] |
| Lactacystin | 1 µM | proteasome | [131] |
| Mitomycin | 1 µM | DNA synthesis | [132] |
| Paclitaxel | 10 nM | β-tubulin | [133] |
| Torkinib | 1 µM | mTOR | [134] |

**3.2.2. Chemical genomic analyses of autophagy induction patterns associated with**

**small molecules**

I used a chemical genomic approach to classify these autophagy inducers based on their modulation of the autophagy induction patterns associated with various known chemical inhibitors. For this purpose, I firstly examined how pre-treatment with 200 well-established signal transduction modulators inhibited the induction of autophagy by 26 autophagy inducers selected from among the 39 compounds recovered as "hits" in the above screen. The autophagy profile associated with each autophagy inducer was obtained by setting the value of the GFP/RFP ratio in untreated cells and single autophagy inducer-treated cells as 1 and 0, respectively (Figure 3-8). Highly reproducible datasets from 2 independent experiments were averaged and subjected to PCA and clustering analysis (Figure 3-9). On the PC1-PC2 plane, autophagy inducers appeared to group based on their mode of action, given that mTOR inhibitors (Rapamycin and Torin1), ER stress inducers (2-deoxyglucose and Tunicamycin), epigenetic modulators (Azacytidine, SAHA, and Trichostatin A), and proteasome inhibitors (Bortezomib and MG132) yielded closely co-localizing patterns by class (Figure 3-10). Epigenetic modulators as well as proteasome inhibitors also were distinctly positioned on the PC3-PC4 plane (Figure 3-11). A loading plot showed that some portions of the patterns associated with signaling via cell cycle kinases (aurora, ataxia telangiectasia mutated (ATM), and cyclin-dependent kinase (CDK)) and HSP90/hypoxia inducible factor (HIF) were coordinated on the PC2 plane, while the patterns associated with a number of signal transduction modulators were coordinated on the PC1 plane (Figure 3-12). Vacuolar-type $H^+$-ATPase (V-ATPase)/protein kinase C (PKC)/Survivin/Akt inhibitors affected parameters on both the

PC1 and PC2 planes (Figure 3-12). Parameters on the PC3 and PC4 planes were negatively coordinated by fibroblast growth factor receptor (FGFR)/Janus kinase (JAK)/spleen tyrosine kinase (Syk)/tropomyosin receptor kinase A (TrkA) signaling and phosphoinositide 3-kinase (PI3K)/transforming growth factor beta (TGF-β)/Rho-associated coiled-coil protein kinase (ROCK) signaling, respectively, while adenosine kinase (ADK)/ribonucleotide reductase (RR)/tumor progression locus 2 (Tpl2) signaling positively coordinated along the PC4 axis (Figure 3-13). Next, I performed clustering analysis using all of the obtained inhibitory data. As shown in Figure 3-14, autophagy inducers classified into approximately 6 distinct groups, including epigenetic modulators (Cluster 1), ER stress inducers (Cluster 2), and proteasome inhibitors (Cluster 6). JQ1 sorted separately from these clusters, possibly reflecting the observation that autophagy induced by JQ1 was not inhibited by almost any of the signal transduction modulators. Given that JQ1 is an inhibitor of bromodomain containing 4 (BRD4), a transcriptional repressor of autophagy/lysosomal genes, I inferred that JQ1 directly induces autophagy in a signal transduction-independent manner [110]. In contrast, autophagy induction by Cyclosporine A was inhibited by multiple signal transduction modulators, presumably reflecting the multiple activities of Cyclosporine A [135] and explaining the distinct autophagy induction profile associated with this molecule. Among the signal transduction modulators, histone methyltransferase G9a/hypoxia inducible factor (HIF)/HSP90/ protein kinase R (PKR) and several cell cycle kinase inhibitors showed global inhibition of autophagy (Figure 3-15). In line with the results of PCA, modulators of signaling by JAK/signal transducers and activators of transcription (STAT), TGF-β/p300/ROCK, and RR/ADK/Tpl2 selectively inhibited the autophagy induced by compounds within (respectively) Clusters 6, 5, and 1 (Figure 3-15). Although specific signaling pathways

differing between Clusters 2, 3, and 4 were not observed, similarities of the patterns of

the autophagy profiles among these clusters were inferred to be indicative of some shared

mechanisms of autophagy induction.
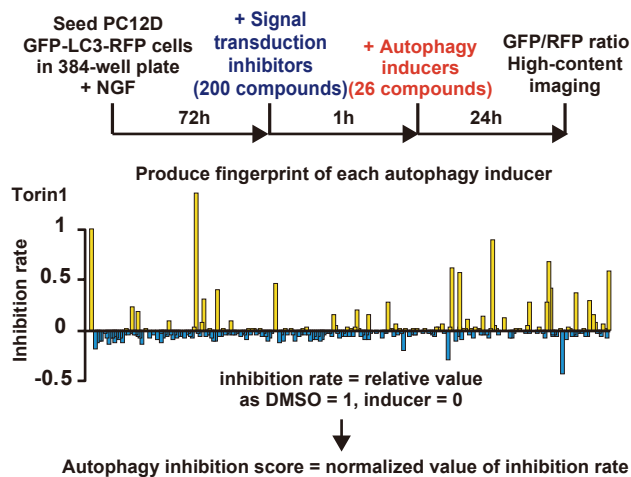


**Figure 3-8.** Schematic illustration of the experiments for chemical genomic analyses.
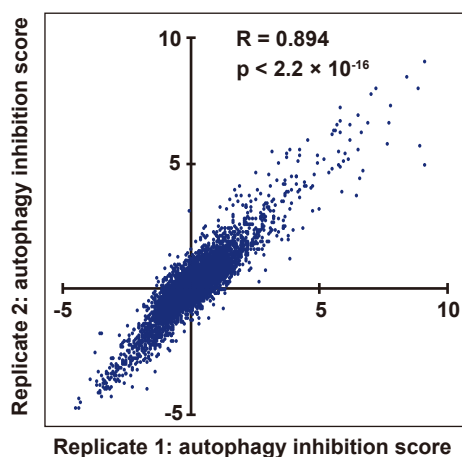


**Figure 3-9.** Scatter-plot of the two-independent datasets of autophagy inhibition scores,
as used to confirm reproducibility.
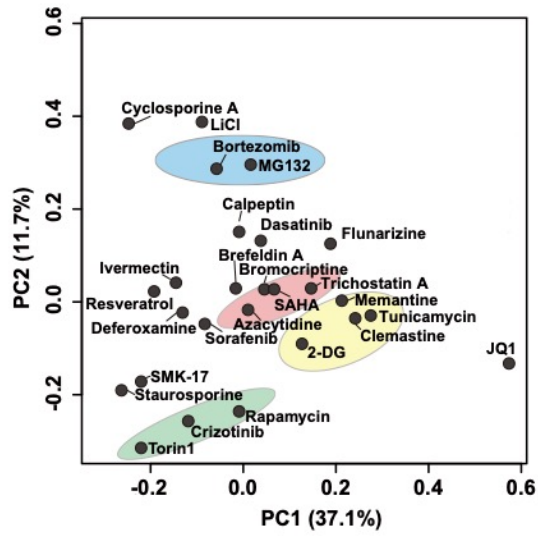
**Figure 3-10.** Two-dimensional plot of PCA scores of PC1 and PC2 as analyzed by autophagy inhibition scores.
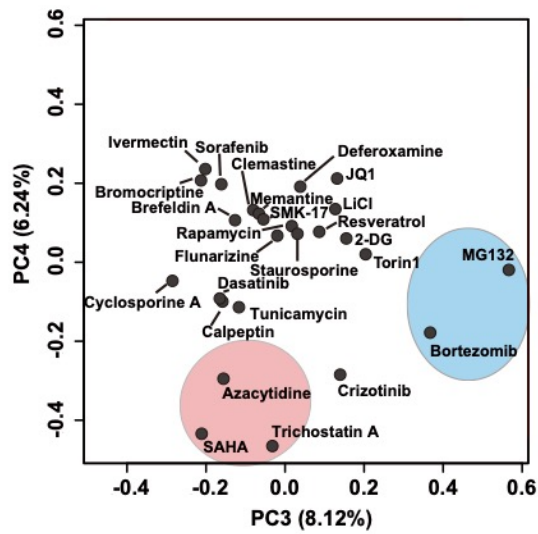


**Figure 3-11.** Two-dimensional plot of PCA scores of PC3 and PC4 as analyzed by autophagy inhibition scores.
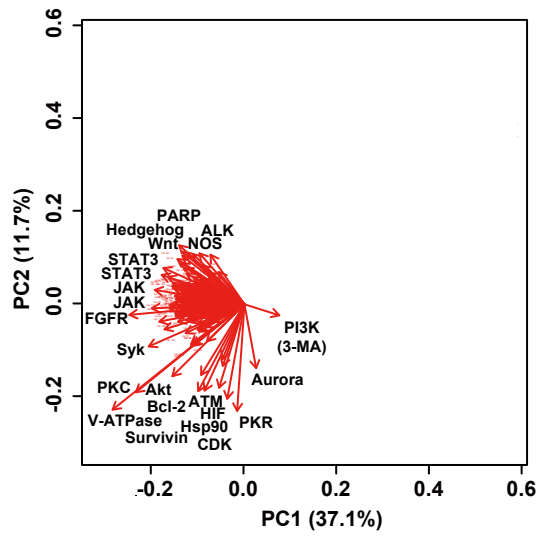
**Figure 3-12.** Loading plot of PC1 and PC2 and from the PCA of autophagy inhibition scores.
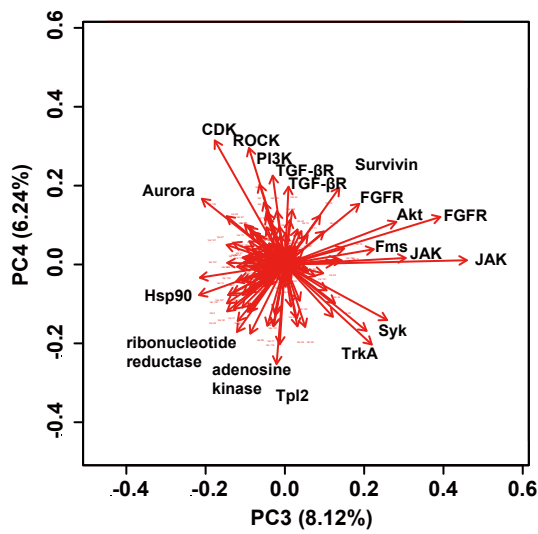


**Figure 3-13.** Loading plot of PC3 and PC4 and from the PCA of autophagy inhibition scores.
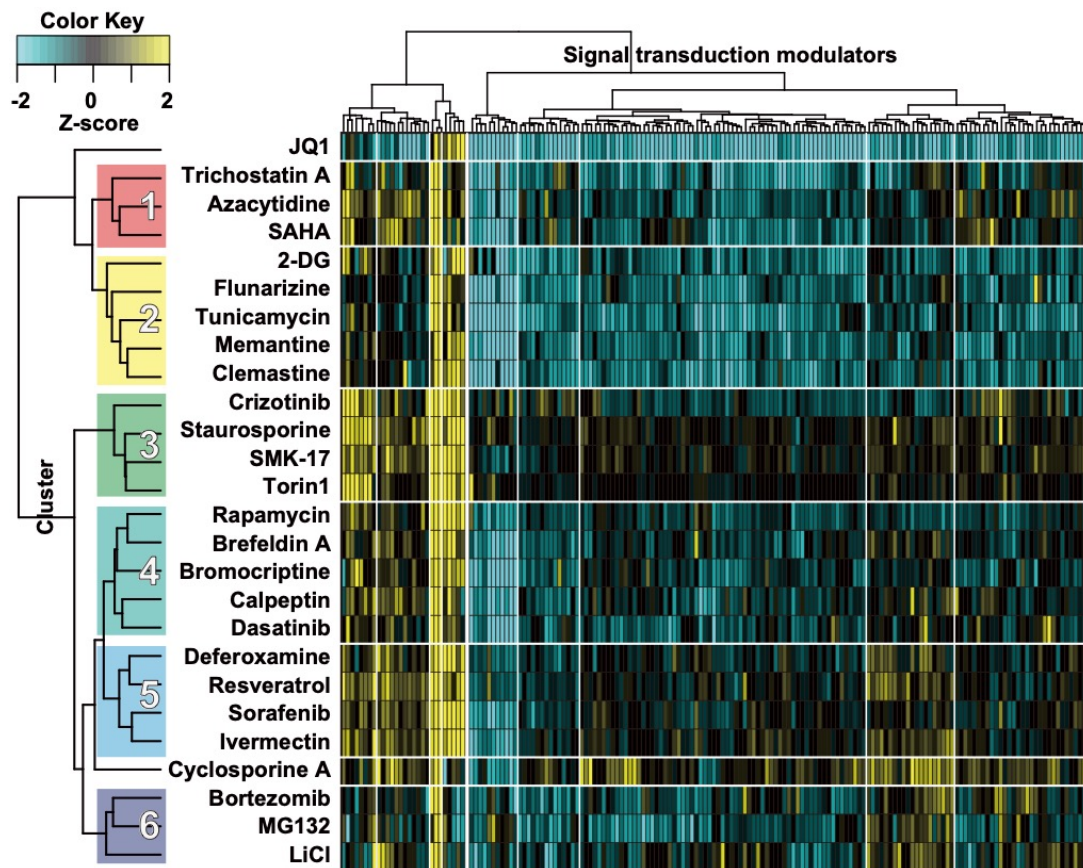
**Figure 3-14.** Hierarchical clustering and heatmap analyses of the chemosensitivity profiles of autophagy inhibition against 26 autophagy inducers. Hierarchical clustering analysis was performed using Euclidean distance and Ward's method. Rows indicate 170 different well-established compounds, and columns indicate 26 autophagy inducers. The heatmap shows a gradient color scale ranging from cyan to black to yellow, indicating the autophagy inhibition score (z-score).
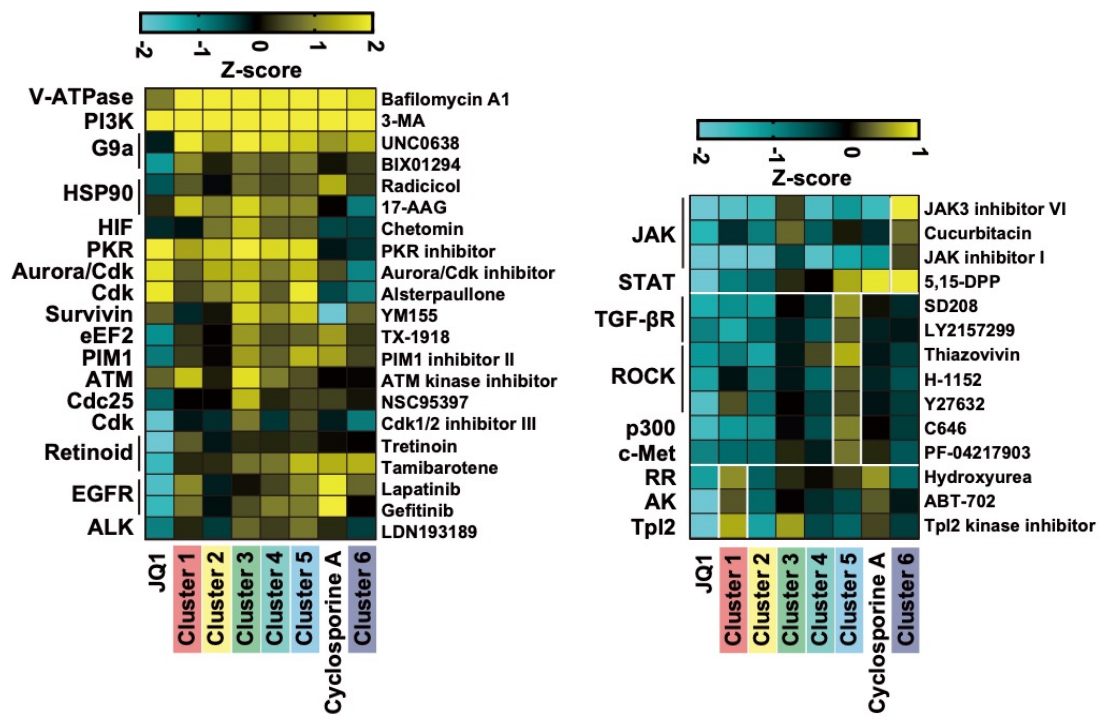
**Figure 3-15.** Heatmap analyses of the autophagy profiles of the average of each cluster with the indicated signal transduction modulators. The heatmap shows a gradient color scale ranging from cyan to black to yellow, indicating the autophagy inhibition score (z-score).

### 3.2.3. Memantine and Clemastine induce ER stress

I observed that Memantine, Clemastine, and Flunarizine, three clinically used drugs were classified into Cluster 2 with Tunicamycin and 2-deoxyglucose, known inducers of ER stress. This result raised the possibility that these three clinically used drugs also are inducers of ER stress. As shown in Figure 3-16, both the expression levels of C/EBP homologous protein (CHOP) and the phosphorylation levels of eukaryotic translation initiation factor 2 alpha (eIF2$\alpha$) were increased by treatment with Memantine, Clemastine, and Flunarizine, as was seen for Tunicamycin and 2-deoxyglucose. The expression levels of CHOP and the phosphorylation levels of eIF2$\alpha$ were increased by the phosphorylation of PERK, a known sensor of ER stress, and the phosphorylation of PERK (as judged by the mobility shift of PERK on SDS-PAGE [136-138] was observed following treatment with Memantine and Clemastine, though not with Flunarizine (Figure 3-17). In addition, increased levels of glucose-regulated protein 78 (GRP78) expression and accumulation of the mRNA encoding spliced X-box binding protein 1 (XBP1), which were seen in Tunicamycin- or 2-deoxyglucose-treated PC12D cells, also were observed in cells treated with Memantine or Clemastine, though not in cells treated with Flunarizine (Figure 3-18). These results suggested that two of these FDA-approved drugs, Memantine and Clemastine, are inducers of ER stress. Although Flunarizine increased phosphorylation of eIF2$\alpha$ and CHOP expression, this increase was mediated by a PERK-independent pathway, indicating that Flunarizine might induce the integrated stress response rather than ER stress [139].
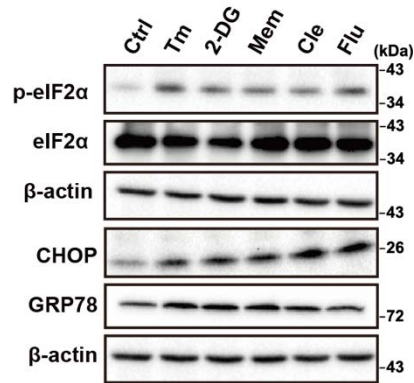
**Figure 3-16.** Effect of Memantine, Clemastine, and Flunarizine on the expression of ER stress markers. NGF-differentiated PC12D cells were treated with 2 $\mu$M Tunicamycin (Tm), 10 mM 2-deoxyglucose (2-DG), 100 $\mu$M Memantine (Mem), 5 $\mu$M Clemastine (Cle), or 20 $\mu$M Flunarizine (Flu). After 12 h (for detection of eIF2$\alpha$ phosphorylation) or 24 h (for detection of GRP78 and CHOP expression), the cells were collected and subjected to western blotting analysis with the indicated antibodies.
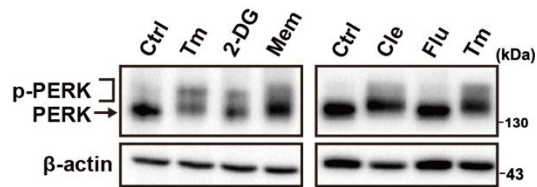


**Figure 3-17.** Memantine and Clemastine induce PERK phosphorylation. NGF-differentiated PC12D cells were treated with the indicated compounds at the same concentrations as described in Figure 3-16. After 12 h, the cells were collected and subjected to western blotting analysis with the indicated antibodies.
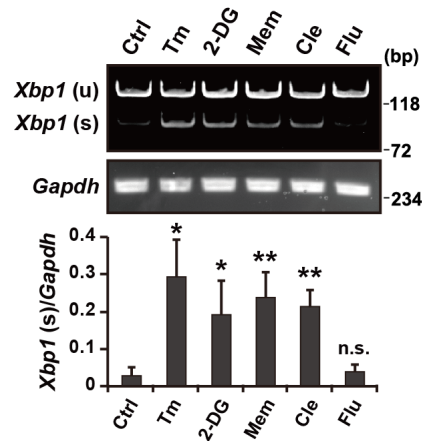
**Figure 3-18.** Memantine and Clemastine induce alternative *Xbp1* mRNA splicing. NGF-differentiated PC12D cells were treated with the indicated compounds for 12 h at the same concentrations as described in Figure 3-16. Unspliced (u) and spliced (s) *Xbp1* were detected by mRNA splicing assay. Data are shown as mean ± SD (n=3). n.s., non-significant, *p < 0.05, **p < 0.01 (Student's t test).

### 3.2.4. SMK-17 induces autophagy in a MEK-inhibition- or mTOR-independent manner

In the course of my primary screen (Figure 3-6), I identified a novel autophagy inducer, SMK-17 (Figure 3-19). SMK-17 induced the generation of LC3-II (microtubule associated protein 1 light chain 3 beta-II, lipidated), an indicator of autophagosome formation [88]) in a time-dependent manner (Figure 3-20). The LC3 conversion by SMK-17 were further increased in the presence of lysosomal inhibitor, Bafilomycin A1 (Figure 3-21), indicating that SMK-17 activates autophagy flux. Consistently, the number of red dots were increased following exposure to SMK-17 in PC12D cells expressing a tandem fluorescent label-tagged LC3 (mCherry-GFP-LC3, tfLC3 [140]), a well-established autophagic probe (Figure 3-22). Given that SMK-17 originally was developed as a selective inhibitor of MEK1/2 [141], I examined whether MEK inhibition stimulates autophagy. As shown in Figure 3-22 and 23, unlike other MEK inhibitors (U0126 and PD184352), SMK-17 activated autophagosome formation and increased the number of red dots seen in PC12D cells expressing a tfLC3 probe, indicating that SMK-17 induced autophagy in a MEK inhibition-independent manner. Given that SMK-17 clustered with Torin1 by clustering analysis (Figure 3-14), I next examined whether SMK-17 induced autophagy via the mTOR pathway. Torin1 suppressed the accumulation of phospho-S6, phospho-S6K, and phospho-ULK1 (Figure 3-24), effects known to reflect inhibition of mTOR [88]. SMK-17 also yielded attenuation of the level of phospho-S6, but not those of phospho-S6K and phospho-ULK1 (Figure 3-24), suggesting that SMK-17 induces autophagy via a mTOR-independent pathway. Given that U0126 also yielded attenuation of the levels of phospho-S6, I inferred that the decrease in phospho-S6 level following

SMK-17 exposure reflects the inhibition of MEK by SMK-17. SMK-17 increased the expression level of p62, an autophagy substrate, indicating that SMK-17 either inhibits autophagic degradation or transcriptionally up-regulates the p62 mRNA expression [88] (Figure 3-20). Considering that SMK-17 enhanced autophagy flux measured by various experiments (Figure 3-6, 21, 22), I expected that SMK-17 would transcriptionally increase the p62 expression, and examined the possible involvement of TFEB, a master regulator of lysosomal/autophagy gene expression in SMK-17-induced autophagy [142-144].
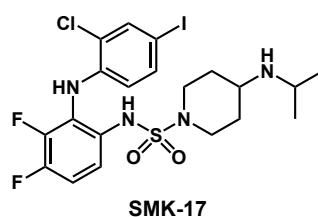


**Figure 3-19.** Chemical structure of SMK-17.
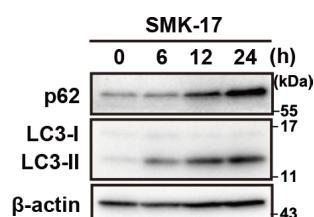


**Figure 3-20.** Western blotting analysis of NGF-differentiated PC12D cells treated with 10 $\mu$M SMK-17 for the indicated times for 24 h with the indicated antibodies.
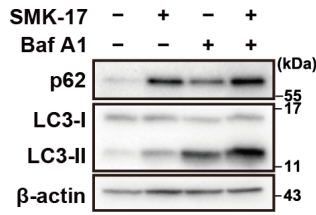
**Figure 3-21.** Western blotting analysis of NGF-differentiated PC12D cells treated with 10 $\mu$M SMK-17 in the presence or absence of 100 nM Bafilomycin A1 (Baf A1) for 24-h with the indicated antibodies.
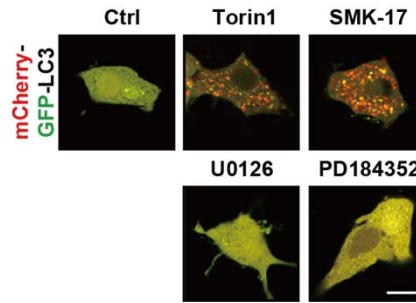


**Figure 3-22.** NGF-differentiated PC12D cells transfected with the mCherry-GFP-LC3 (tfLC3) plasmid vector were treated with 100 nM Torin1, 10 $\mu$M SMK-17, 10 $\mu$M U0126, or 10 $\mu$M PD184352 for 8 h.
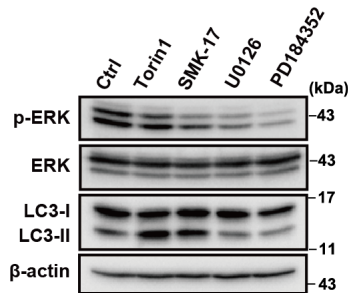


**Figure 3-23.** Western blotting analysis of NGF-differentiated PC12D cells treated with 100 nM Torin1, 10 $\mu$M SMK-17, 10 $\mu$M U0126, or 10 $\mu$M PD184352 for 4 h with the indicated antibodies.
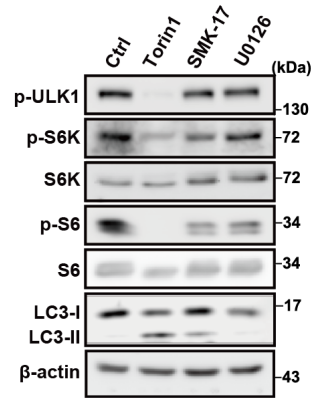
**Figure 3-24.** Western blotting analyses of NGF-differentiated PC12D cells treated with 100 nM Torin1, 10 $\mu$M SMK-17, or 10 $\mu$M U0126 for 1 h with the indicated antibodies.

### 3.2.5. SMK-17 induces TFEB nuclear translocation leading to autophagy activation

Interestingly, although SMK-17 apparently did not inhibit mTOR, the compound induced TFEB nuclear translocation leading to lysosomal/autophagy gene expression (Figure 3-25), a process that is regulated primarily by mTOR [93]. Indeed, I found that SMK-17 induced up-regulation of the expression of 9 well-known TFEB target genes including *Sqstm1/p62* (Figure 3-26). In addition, knockdown of TFEB (Figure 3-27) significantly suppressed the SMK-17-induced expression of all these TFEB target genes (Figure 3-28), and also suppressed SMK-17-induced autophagy (Figure 3-29). These results indicated that SMK-17 induced autophagy through TFEB-mediated lysosomal/autophagy gene expression.
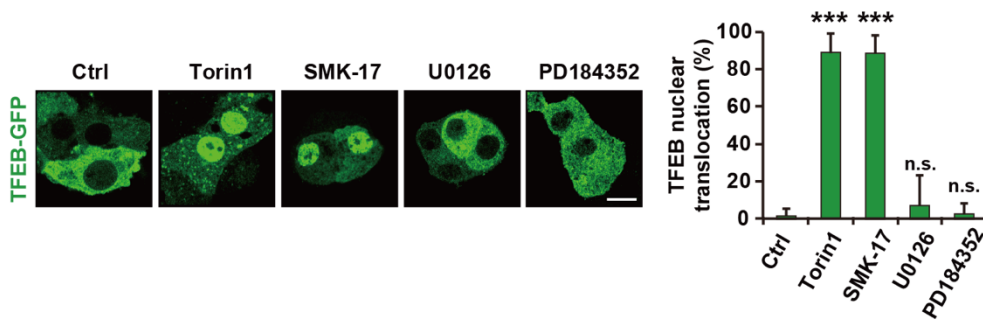


**Figure 3-25.** Representative images and quantification of TFEB nuclear translocation assay results. NGF-differentiated PC12D cells stably expressing TFEB-GFP were treated with 100 nM Torin1, 10 $\mu$M SMK-17, 10 $\mu$M U0126, or 10 $\mu$M PD184352 for 1 h. The scale bar represents 20 $\mu$m. Data are shown as mean $\pm$ SD (n=3). n.s., non-significant, ***p $<$ 0.001 (Student's t test).
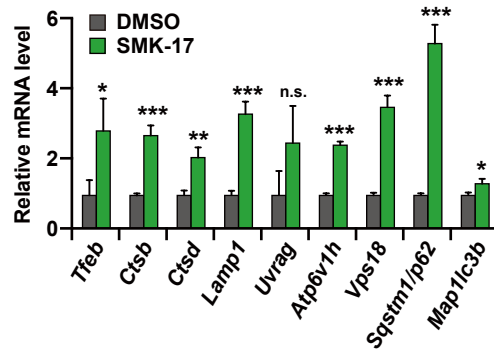
**Figure 3-26.** NGF-differentiated PC12D cells were treated with 10 $\mu$M SMK-17 for 6 h followed by qRT-PCR analysis. Data are shown as mean ± SD (n=3). n.s., non-significant, *p < 0.05, **p < 0.01, ***p < 0.001 (Student's t test).
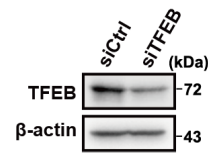


**Figure 3-27.** Knockdown of TFEB in NGF-differentiated PC12D cells was confirmed with western blotting.
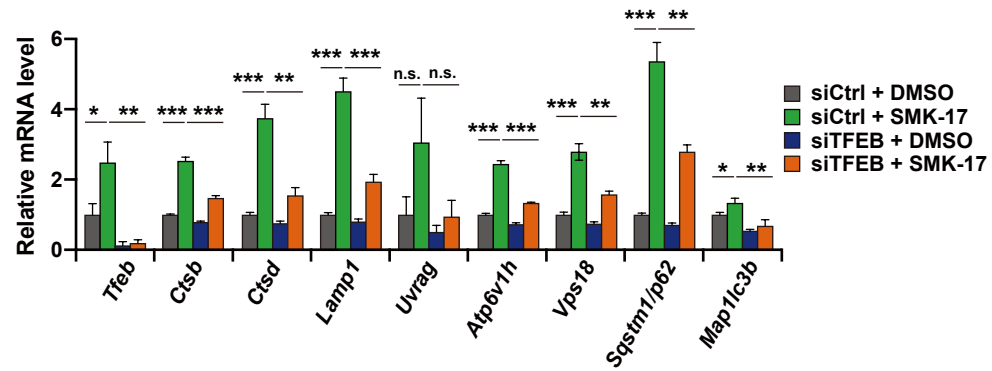


**Figure 3-28.** NGF-differentiated PC12D cells transfected with TFEB siRNA or control siRNA were treated with 10 $\mu$M SMK-17 for 6 h followed by qRT-PCR analysis. Data are shown as mean ± SD (n=3). n.s., non-significant, *p < 0.05, **p < 0.01, ***p < 0.001 (Student's t test).
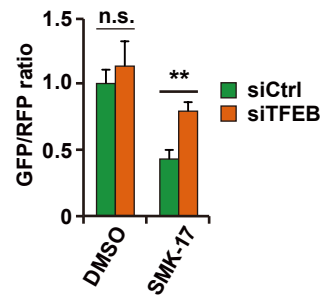
**Figure 3-29.** Involvement of TFEB in SMK-17-induced autophagy. NGF-differentiated PC12D cells expressing GFP-LC3-RFP were transfected with TFEB siRNA or control siRNA and then treated with 10 $\mu$M SMK-17 for 24 h. Autophagy flux was evaluated by GFP/RFP ratio using a plate-reader. Data are shown as mean ± SD (n=3). n.s., non-significant, **p < 0.01 (Student's t test).

### 3.2.6. SMK-17 activates PKC-TFEB pathway leading to clearance of protein aggregates

A previous study showed that PKC controls TFEB activity in a mTOR-independent manner [145]. Moreover, my chemical genomic analysis revealed that a PKC inhibitor counteracted SMK-17-induced autophagy (Figure 3-10, 12). Therefore, I examined the possible involvement of PKC in the SMK-17-mediated autophagy pathway. I found that the phosphorylation levels of PKC substrates were increased in SMK-17-treated cells as well as phorbol 12-myristate 13-acetate (PMA, PKC activator)-treated cells (Figure 3-30), and the increased phosphorylation of PKC substrates by SMK-17 treatment was abrogated by PKC inhibitor Gö6983 (Figure 3-31), indicating that SMK-17 enhances PKC activity. Moreover, TFEB nuclear translocation induced by SMK-17 was strongly suppressed by the PKC inhibitor, although this PKC inhibitor did not affect Torin1-induced TFEB nuclear translocation (Figure 3-32), indicating that SMK-17-induced TFEB nuclear localization is regulated by PKC signaling. TFEB nuclear translocation is expected to induce lysosomal biogenesis [93], and SMK-17 or Torin1 induced lysosomal biogenesis as judged from the increased LysoTracker DND-99 signal intensity, an indicator of acidic organelles including lysosomes. This effect induced by SMK-17 was suppressed by PKC inhibition, while the increased signal intensity of LysoTracker by Torin1 treatment was not affected by PKC inhibition (Figure 3-33). Consistently, this PKC inhibitor inhibited SMK-17-induced autophagy, but not Torin1-induced autophagy (Figure 3-34). These results indicated that SMK-17 induces autophagy and lysosomal biogenesis via mTOR-independent but PKC-dependent TFEB activation.

Accumulation of aggregated proteins is associated with various diseases including neurodegenerative disorders such as PD and HD. Autophagy induction has been proposed as a new strategy for the treatment of proteinopathies by removing cytotoxic aggregates or damaged organelles [90]. Therefore, I examined whether autophagy activation by SMK-17 results in the depletion of protein aggregates. As I described in Chapter 2, I observed that the treatment with 1-methyl-4-phenylpyridinium ($MPP^+$), a compound widely used to induce cellular and animal models of PD, causes aggresome formation (Figure 2-39). In the present work, I observed that SMK-17 induced the clearance of aggresomes formed in PC12D cells and human neuroblastoma SH-SY5Y cells pre-treated with $MPP^+$. Notably, the aggresome-clearing effect of SMK-17 was significantly abrogated in the presence of a PKC inhibitor (Figure 3-35, 36). I also tested the efficacy of SMK-17 in a cellular model of HD induced by overexpression of EGFP-tagged huntingtin exon1 containing 74 polyQ repeats (EGFP-HTTQ74), a well-established autophagy substrate [91] (Figure 3-37). As a result, transfection with EGFP-HTTQ74 but not wild type 23 polyQ repeats (EGFP-HTTQ23) caused aggregation in neuronal PC12D cells (Figure 3-38). HTTQ74 aggregation was suppressed by not only SMK-17 but also Torin-1, and PKC inhibitor remarkably inhibited only SMK-17-mediated clearance of HTTQ74 aggregates (Figure 3-38). Taken together with these results, I propose that SMK-17 induces clearance of protein aggregates by activating autophagy via the PKC-TFEB pathway.
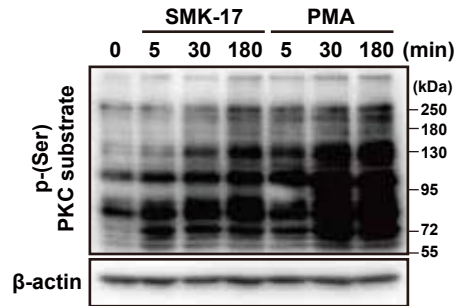
**Figure 3-30.** Western blotting analysis of NGF-differentiated PC12D cells treated with 10 $\mu$M SMK-17 or 100 nM PMA for the indicated times. Phosphorylation of PKC substrates were detected by using p-(Ser) PKC substrate antibody.



**Figure 3-31.** Western blotting analysis of NGF-differentiated PC12D cells treated with 10 $\mu$M SMK-17 in the presence or absence of 5 $\mu$M PKC inhibitor (PKCi, Gö6983) for 3 h. Phosphorylation of PKC substrates were detected by using p-(Ser) PKC substrate antibody.
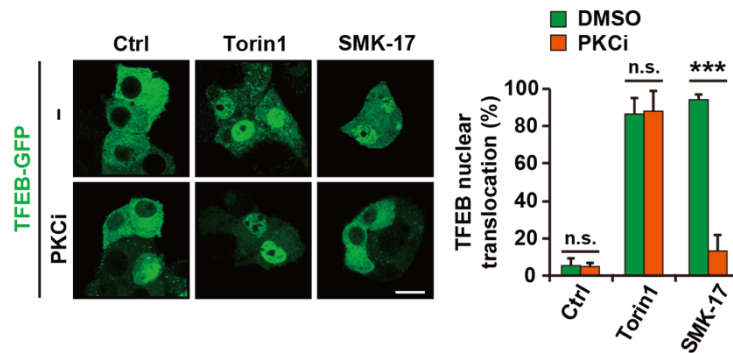
**Figure 3-32.** Representative images and quantification of TFEB nuclear translocation assay results. NGF-differentiated PC12D cells stably expressing TFEB-GFP were treated with 100 nM Torin1 or 10 $\mu$M SMK-17 in the presence or absence of 5 $\mu$M PKC inhibitor (PKCi, Gö6983). The scale bar represents 20 $\mu$m. Data are shown as mean ± SD (n=3). n.s., non-significant, ***$p < 0.001$ (Student's t test).
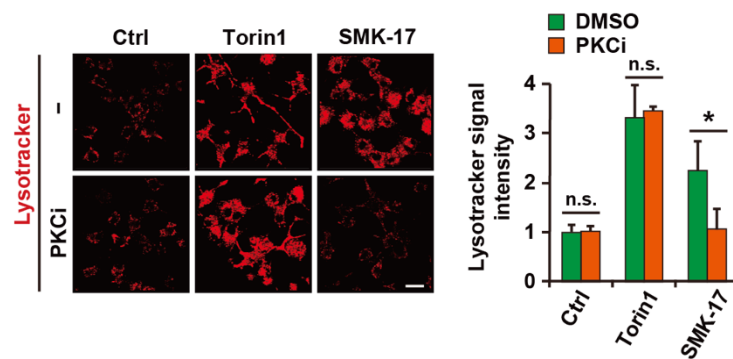


**Figure 3-33.** Representative images and quantification of LysoTracker Red DND-99 staining assay results. NGF-differentiated PC12D cells were treated with 100 nM Torin1, 10 $\mu$M SMK-17 in the presence or absence of 5 $\mu$M PKCi. Mean fluorescent intensity was quantified. The scale bar represents 20 $\mu$m. Data are shown as mean ± SD (n=3). n.s., non-significant, *$p < 0.05$ (Student's t test).
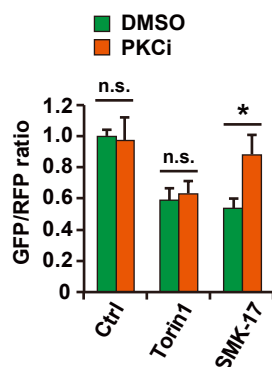
**Figure 3-34.** NGF-differentiated PC12D cells expressing GFP-LC3-RFP were treated with 100 nM Torin1 or 10 $\mu$M SMK-17 for 24 h in the presence or absence of 5 $\mu$M PKCi. Autophagy flux was evaluated by GFP/RFP ratio using a plate-reader. Data are shown as mean $\pm$ SD (n=3). n.s., non-significant, *$p < 0.05$ (Student's t test).
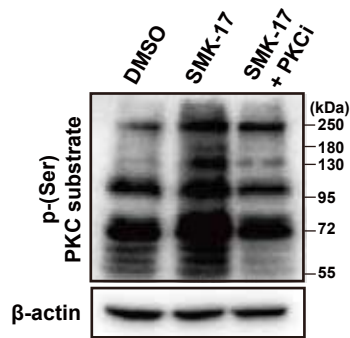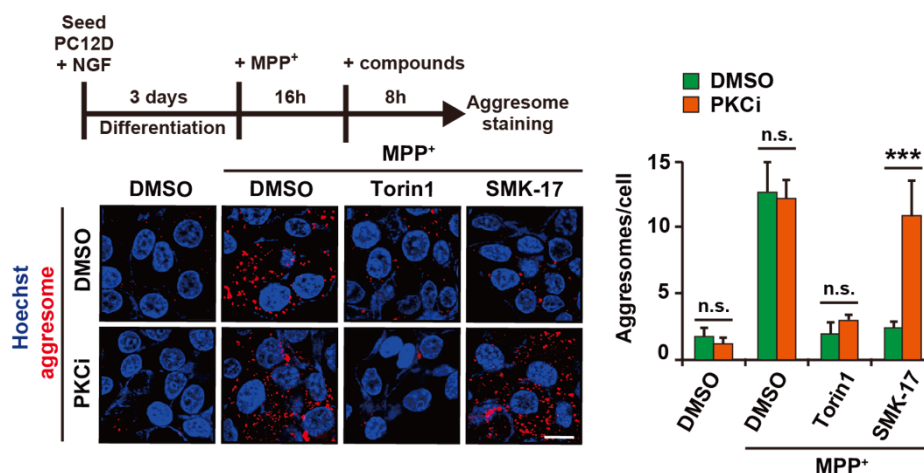


**Figure 3-35.** Representative images and quantification of aggresome clearance assay results. NGF-differentiated PC12D cells were treated with MPP[+] for 16 h prior to treatment with 100 nM Torin1 or 10 $\mu$M SMK-17 for 8 h in the presence or absence of 5 $\mu$M PKCi. The scale bar represents 20 $\mu$m. Data are shown as mean $\pm$ SD (n=3). n.s., non-significant, ***$p < 0.001$ (Student's t test).
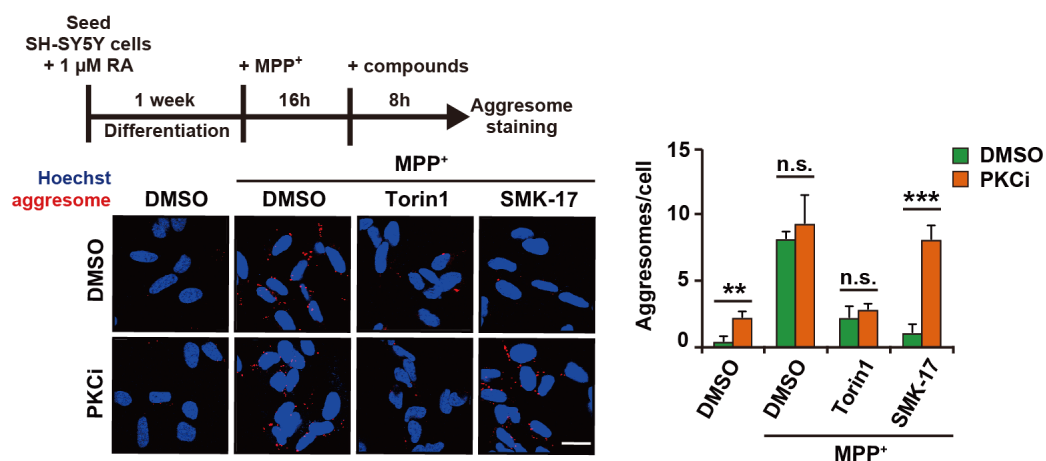
**Figure 3-36.** Representative images and quantification of aggresome clearance assay results. RA-differentiated SH-SY5Y cells treated with MPP$^+$ for 16 h prior to treatment with 100 nM Torin1 or 10 $\mu$M SMK-17 for 8 h in the presence or absence of 5 $\mu$M PKC inhibitor. The scale bar represents 20 $\mu$m. Data are shown as mean $\pm$ SD (n=3). n.s., non-significant, **p $<$ 0.01, ***p $<$ 0.001 (Student's t test).



**Figure 3-37.** Western blotting analysis of NGF-differentiated PC12D cells transiently transfected with GFP, GFP-HTTQ23, or GFP-HTTQ74 for 72 h.
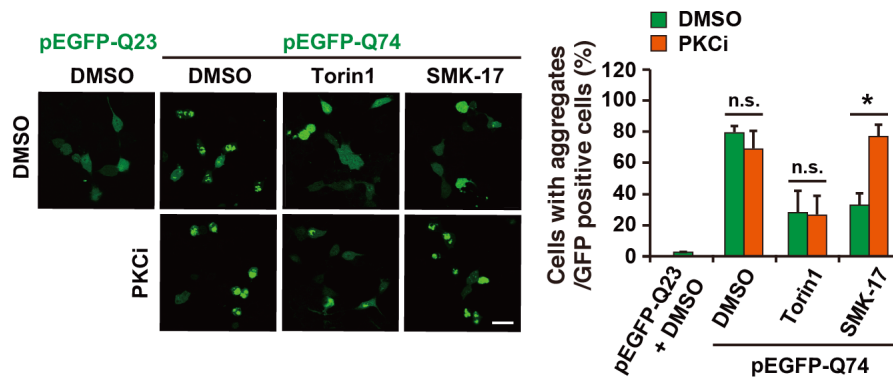
**Figure 3-38.** Representative images and quantification of mutant huntingtin clearance assay results. NGF-differentiated PC12D cells were transiently transfected with GFP-HTTQ23 or GFP-HTTQ74 for 48 h prior to treatment with 100 nM Torin1 or 10 $\mu$M SMK-17 for 24 h in the presence or absence of 5 $\mu$M PKCi. Percentage of cells with GFP-huntingtin aggregates to GFP-positive cells was calculated in each sample. The scale bar represents 20 $\mu$m. Data are shown as mean $\pm$ SD (n=3). n.s., non-significant, *p < 0.05, (Student's t test).

### 3.2.7. Clearance activity of protein aggregates by autophagy-inducing small molecules

PD is pathologically associated with the interrelated processes of abnormal protein accumulation and oxidative stress due to mitochondrial dysfunction [146]. Indeed, I found that the well-known antioxidants N-acetylcysteine (NAC) and glutathione (GSH) as well as the autophagy inducers SMK-17, Torin1, and Rapamycin significantly inhibited aggresome formation when provided simultaneously with MPP$^+$ (Figure 3-39). In contrast, although the autophagy inducers also provided significant clearance of aggresomes in cells pre-treated with MPP$^+$, NAC and GSH did not (Figure 3-40). These results indicated that autophagy induction is required for clearance of aggregated proteins in the cellular models of PD. To confirm this inference, 26 small molecules identified as autophagy inducers were assessed for their aggresome clearance activity. Notably, almost all of the autophagy inducers (excepting 2-deoxyglucose and two proteasomal inhibitors, MG132 and Bortezomib) yielded significant attenuation of aggresome accumulation (Figure 3-41). Similarly, these autophagy inducers significantly induced the clearance of mutant huntingtin (Figure 3-42). Finally, I evaluated the cytotoxicity of autophagy inducers tested in this study against more appropriate cells derived from neural tissues than PC12D cells. I found that 23 autophagy inducers that induced the clearance of protein aggregates, did not show cytotoxicity against primary cultured rat cortical neurons as judged from LDH assay (blue bars, Figure 3-43). Interestingly, other autophagy inducers including cytotoxic compounds against PC12D cells, except for CCCP, also did not affect cell viability in primary cultured rat cortical neurons (black bars, Figure 3-43). These results suggested that stimulation of autophagy removes protein aggregates without

neurotoxicity, implying on a potential indication of treatment against neurodegenerative diseases with neuronal aggregations.
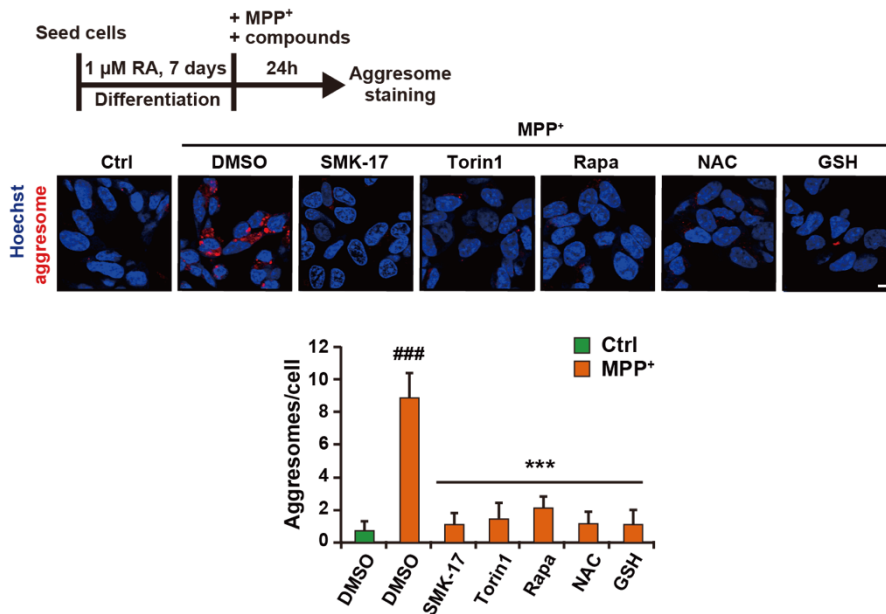


**Figure 3-39.** Representative images and quantification of aggresome formation assay results. RA-differentiated SH-SY5Y cells were treated with MPP$^+$ for 24 h in the presence or absence of 10 $\mu$M SMK-17, 100 nM Torin1, 10 $\mu$M rapamycin, 10 mM NAC, or 10 mM GSH. The scale bar represents 20 $\mu$m. Data are shown as mean $\pm$ SD (n=3). $^{\#\#\#}$p < 0.001 (Student's t test compared to untreated control (Ctrl)). $^{***}$p < 0.001 (two-tailed Student's t test).
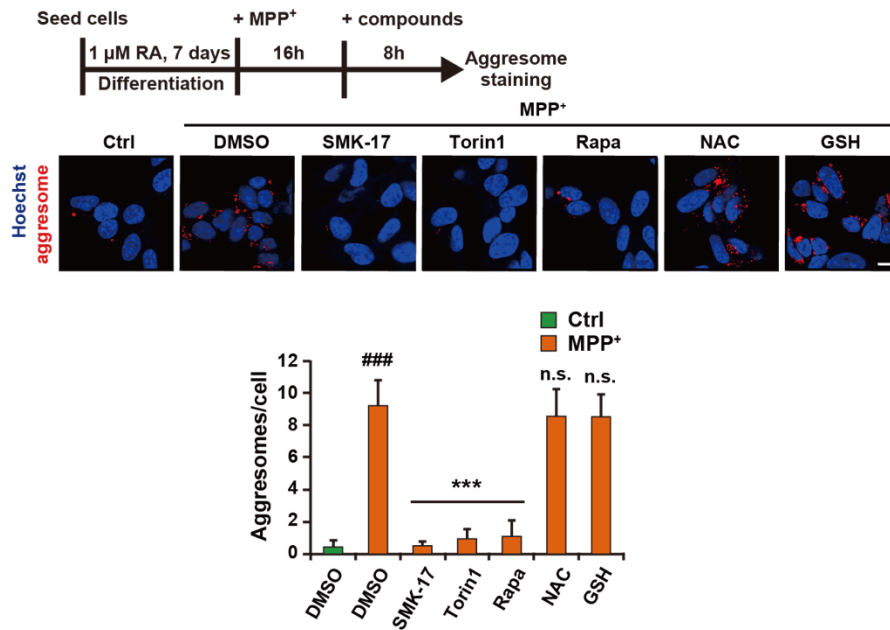
**Figure 3-40.** Representative images and quantification of aggresome clearance assay results. RA-differentiated SH-SY5Y cells were treated with MPP⁺ for 16 h prior to treatment with 10 $\mu$M SMK-17, 100 nM Torin1, 10 $\mu$M Rapamycin, 10 mM NAC, or 10 mM GSH for 8 h. The scale bar represents 20 $\mu$m. Data are shown as mean ± SD (n=3). $^{\#\#\#}p < 0.001$ (Student's t test compared to untreated control (Ctrl)). n.s., non-significant, $^{***}p < 0.001$ (Student's t test).
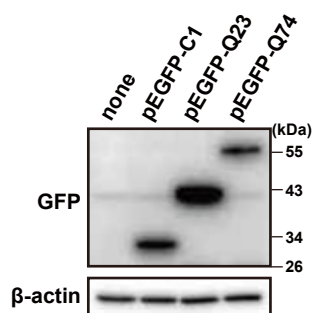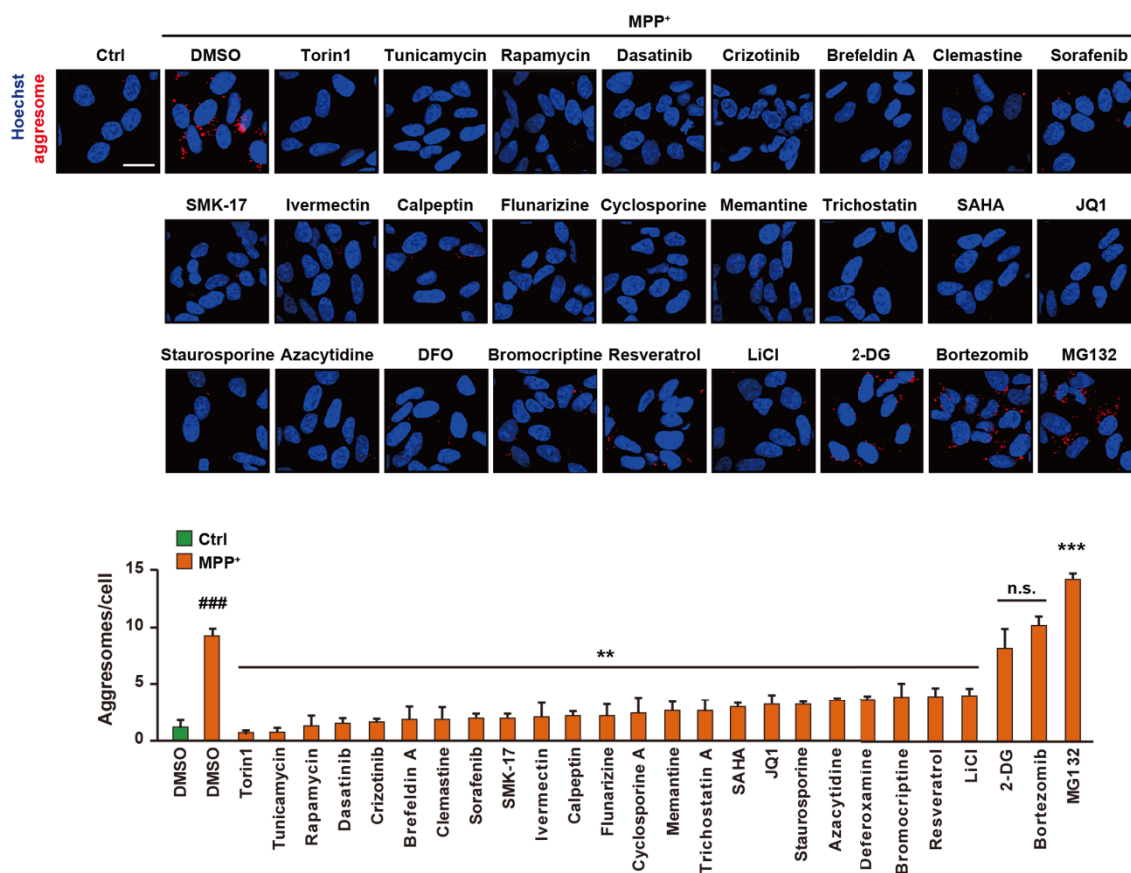
**Figure 3-41.** Representative images and quantification of the aggresome clearance assay results. RA-differentiated SH-SY5Y cells were treated with MPP$^+$ for 16 h prior to treatment with the indicated compounds for 8 h. See also Table 1. The scale bar represents 10 $\mu$m. Data are shown as mean $\pm$ SD (n=3). $^{\#\#\#}$p $<$ 0.001 (Student's t test compared to untreated control (Ctrl)). n.s., non-significant, **p $<$ 0.01, ***p $<$ 0.001 (Student's t test).
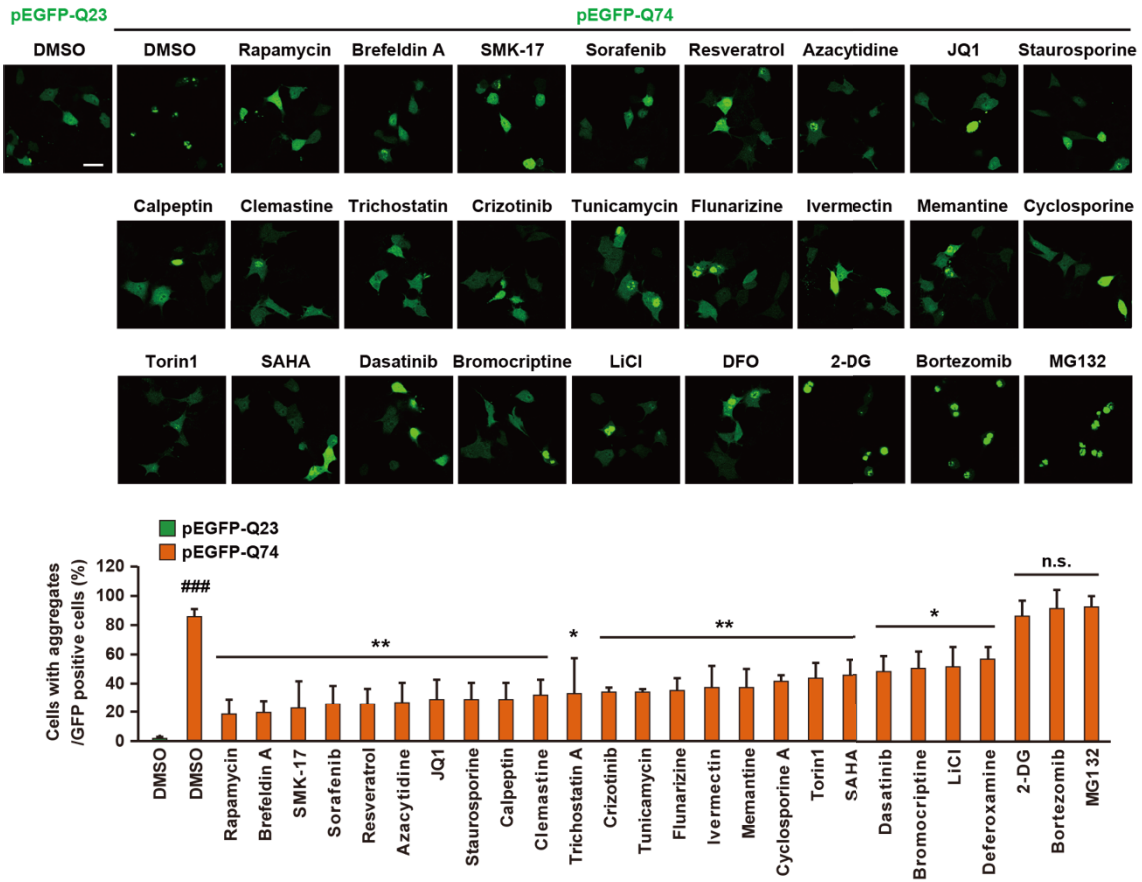
**Figure 3-42.** Representative images and quantification of the mutant huntingtin clearance assay results. NGF-differentiated PC12D cells were transiently transfected with GFP-HTTQ23 or GFP-HTTQ74 for 48 h prior to treatment with the indicated compounds for 24 h. See also Table 1. Percentage of cells with GFP-huntingtin aggregates to GFP-positive cells was calculated in each sample. The scale bar represents 10 $\mu$m. Data are shown as mean ± SD (n=3). [###]p < 0.001 (Student's t test compared to untreated control). n.s., non-significant, *p < 0.05, **p < 0.01 (Student's t test).
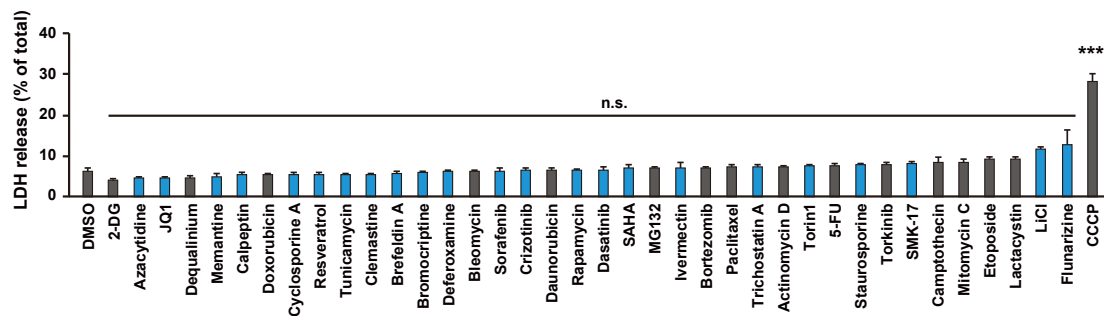
**Figure 3-43.** Cytotoxicity of the autophagy inducers against primary cultured rat cortical neurons. Cells were treated with the indicated compounds for 24 h, and cytotoxicity was measured by LDH release assay. See also Table 1 and 2. The data are expressed as a percentage of total amount of LDH analyzed in each plate. Data are shown as mean ± SD (n=5). n.s., non-significant, ***p < 0.001 (Dunnett's test).

## 3.3. Discussion

In this study, I addressed the induction of autophagy by small molecules. To this end, I used a chemical genomic technique previously employed for several studies that identified diverse and selective signaling pathways involved in cancer cell migration and ER stress response [96,147]. Among the 39 autophagy inducers identified by my initial chemical screen, 13 compounds were excluded from further investigation because of their cytotoxicity in PC12D cells. The remaining 26 compounds were subjected to chemical genomic analysis to profile the pattern of autophagy induction. Based on the results of PCA and clustering analysis, the autophagy inducers were classified into several groups, possibly reflecting distinct modes of action. Considering the effect of signal transduction inhibitors on autophagy induction, JAK-signal transducers and activators of transcription (STAT), TGF-β/p300/ROCK, ADK/RR/Tpl2 signaling were inferred to be involved in the autophagy induced by compounds within (respectively) Clusters 6, 5, and 1 (Figure 3-15). This finding may provide a clue for mechanistic analysis of the autophagic processes induced by those compounds. Unfortunately, I did not identify specific pathways associated with the differences among Clusters 2, 3, and 4 (Figure 3-14). However, I hypothesize that similarities in the patterns of the autophagy profiles may be associated with overlapping mechanisms of autophagy induction. Next, I asked whether autophagy inducers in Clusters 3 and 4 inhibit mTOR, given that Torin1 and Rapamycin were classified into Clusters 3 and 4, respectively. Like Torin1, SMK-17, Staurosporine, and Crizotinib are members of Cluster 3 and yielded attenuation of phospho-S6 levels; however, SMK-17, Staurosporine, and Crizotinib did not yield changes in the levels of phospho-ULK1, in contrast to Torin1 (Figure 3-44). On the other hand, Brefeldin A, Bromocriptine, Calpeptin, and Dasatinib did not yield attenuation of either phospho-S6

nor phospho-ULK1 levels, in contrast to Rapamycin, although all 5 of these compounds were assigned to Cluster 4 (Figure 3-45). These results suggested that these compounds did not inhibit mTOR, and that the difference between Clusters 3 and 4 may reflect distinct effects on phospho-S6 accumulation.

My clustering analysis led to the finding that Memantine and Clemastine (Cluster 2) induced ER stress. Memantine is known as an antagonist of the N-methyl-D-aspartate (NMDA) receptor. Memantine and its structural analogue Amantadine have proven efficacy against Alzheimer's disease [148] and PD [149], respectively. Recently, Hirano *et al*. [112] reported that Memantine enhances autophagic flux, leading to the enhanced clearance of aggregation-prone proteins and damaged mitochondria in various neuronal models. However, Memantine-induced autophagy is not dependent on antagonism of the NMDA receptor [112]. In the present work, I demonstrated that Memantine induced autophagy possibly through ER stress induction. Memantine inhibits the NMDA receptor with an $IC_{50}$ of approximately 1 $\mu$M; however, higher concentrations (10-500 $\mu$M) of Memantine affect many additional targets, including the sigma-1 receptor [150]. Since the sigma-1 receptor is a chaperone protein residing at the mitochondrion-associated ER membrane, the inhibition of the sigma-1 receptor is expected to inhibit ER function [151]. Indeed, another sigma-1 receptor antagonist, Haloperidol, has been reported to induce ER stress [152]. Therefore, it is likely that 100 $\mu$M Memantine induces ER stress, possibly due to the inhibition of sigma-1 receptor function. Once ER stress responses are activated, IRE1$\alpha$, a sensor of ER stress, could form a complex with tumor necrosis factor receptor-associated factor-2 (TRAF2) and apoptosis signal-regulating kinase-1 (ASK-1), causing activation of the c-Jun N-terminal kinase (JNK), which in turn promotes autophagy via activation of Beclin-1 [122,153]. Activated IRE1$\alpha$ also activates

the XBP1 transcription factor via unconventional splicing, and the activated XBP1 then regulates transcription of the Beclin-1-encoding gene through direct binding to the gene's promoter region [154]. As a result, Beclin-1 (up-regulated by ER stress) forms a complex with phosphatidylinositol 3-kinase catalytic subunit type 3 (Vps34) and serine/threonine-protein kinase Vps15, triggering autophagosome formation [95]. Indeed, Memantine has been reported to influence Vps34 or components of the Vps34 complex [112]. Clemastine, an antihistamine drug originally marketed for the treatment of allergic rhinitis, has efficacy against multiple sclerosis [155]. Recently, Clemastine was also was shown to be capable of counteracting spinal cord pathology and neuroinflammatory responses in the superoxide dismutase 1 (SOD1)-G93A mouse model of amyotrophic lateral sclerosis [156]. In addition, Clemastine has been reported to activate autophagy in superoxide dismutase 1 (SOD1)-G93A primary microglia [103]. The stimulation of autophagy by Clemastine is consistent with the role that H1-targeting antihistamines play in autophagy [157,158]. Among several histamine H1 receptor antagonists, Astemizole has been reported to induce ER stress and autophagy, possibly through the accumulation of intracellular $Ca^{2+}$ [159]. Moreover, Terfenadine, another histamine H1 antagonist, also has been shown to potentiate the concentration of cytosolic $Ca^{2+}$ and to induce autophagy [157,160]. Therefore, I infer that Clemastine also induces ER stress through increases in cytosolic $Ca^{2+}$, leading in turn to autophagy induction.

Flunarizine, which also was classified into Cluster 2 in my analysis, is a voltage-dependent L-/T-type $Ca^{2+}$ channel blocker that is approved for treating migraine and epilepsy. Moreover, Flunarizine has been reported to alter autophagy [108]. Although Flunarizine did not induce ER stress, as assessed by the failure of the compound to induce PERK phosphorylation, Flunarizine induced activation of the eIF2α-activating

91

transcription factor 4 (ATF4)-CHOP pathway, which is commonly observed with other ER stress inducers classified into Cluster 2. Several genes, including those encoding autophagy related 5, 12 (Atg5, Atg12), and p62, have been reported to be transcriptionally regulated by the eIF2α-ATF4-CHOP pathway [161,162]. There are four eIF2α kinases (PERK, general control nonderepressible 2 (GCN2), protein kinase R (PKR), and heme-regulated inhibitor (HRI)), all of which are activated in response to various stimuli [163]. Therefore, I propose that Flunarizine induces activation of the eIF2α/ATF4/CHOP pathway via eIF2α kinases other than PERK, thereby leading to autophagy induction.

In the course of the screen, I identified a novel autophagy inducer, SMK-17. SMK-17 originally was developed as a MEK1/2 inhibitor that exerts potent antitumor effects both *in vitro* and *in vivo* [117,141]. However, unlike SMK-17, two other MEK inhibitors (U0126 and PD184352) did not activate autophagy flux in PC12D cells, indicating that SMK-17 induces autophagy in a MEK inhibition-independent manner. On the other hand, Trametinib, an inhibitor of MEK1/2, has been reported to activate autophagy in pancreatic ductal adenocarcinoma (PDA) cells, in which the KRAS-RAF-MEK-ERK pathway is activated [164]. These results indicate that the KRAS-RAF-MEK-ERK pathway may regulate autophagy, depending on the status of the cultured cells under study. Mechanistically, Trametinib treatment of PDA cells led to decreased phosphorylation of liver kinase B1 (LKB1) and increased phosphorylation of AMP-activated protein kinase (AMPK; at T172) and ULK1 (at S555) [164], indicating that Trametinib-induced autophagy in PDA cells is mediated by the LKB1-AMPK-ULK1 signaling axis. On the other hand, SMK-17 failed to inhibit phosphorylation of the autophagy-negative regulation site of ULK1 (residue S757), indicating that SMK-17-induced autophagy in PC12D cells is mediated by a pathway distinct from the LKB1-

AMPK-ULK1 signaling axis. PCA of my chemical genomic data predicted the involvement of PKC in SMK-17-induced autophagy. Indeed, I found that SMK-17 activated PKC and induced TFEB nuclear translocation (thereby activating lysosomal biogenesis and autophagy) in a PKC-dependent manner. According to previous reports, PKC activates JNK and p38 MAPK, in turn inactivating zinc finger protein with KRAB and SCAN domains 3 (ZKSCAN3), a repressor of lysosomal/autophagy genes [145,165]. Moreover, some isotypes of PKC also are regulated by 3-phosphoinositide-dependent protein kinase 1 (PDK1) [166]. My chemical genomic study revealed that JNK/p38 inhibitors and an inhibitor of 3-phosphoinositide-dependent protein kinase 1 (PDK1), as well as a PKC inhibitor, counteracted SMK-17-induced autophagy (Figure 3-46). At present, I do not know the mechanism of SMK-17-induced PKC activation, but SMK-17 nonetheless appears to induce autophagy through PKC.

Autophagy has an essential role in eliminating nonfunctional and potentially cytotoxic aggregation-prone proteins. Therefore, the stimulation of autophagy with small molecules may serve as a new therapeutic strategy for proteinopathies including PD, which is characterized by the accumulation of aggregated proteins ("Lewy bodies"). Oxidative stress due to mitochondrial dysfunction is closely associated with PD and is a major cause of protein aggregation [13,167]. As I described in Chapter 2, I observed that $MPP^+$, a neurotoxin known to act as an inhibitor of mitochondrial complex I, induces reactive oxygen species (ROS) and aggresome formation in neuronal PC12D cells. Indeed, the potent antioxidants NAC and GSH significantly suppressed $MPP^+$-induced aggresome formation. However, NAC and GSH failed to induce the clearance of aggresomes formed by pre-treatment with $MPP^+$, indicating that antioxidant molecules can only inhibit aggresomes at the formation stage. On the other hand, almost all of the

autophagy-inducing compounds tested in the present study (with the exception of proteasome inhibitors and 2-deoxyglucose) provided aggresome clearance. Although proteasome inhibitors have been reported to impair autophagy [168,169], my findings that proteasome inhibitors activated autophagy are consistent with recent report that proteasome inhibitors induced autophagy [170]. Considering the ubiquitin-proteasome system is also involved in protein degradation pathway [171], aggresome accumulation has been inferred to be the result of proteasome inhibition. 2-Deoxyglucose exposure mimics glucose deprivation, a process that causes oxidative stress and stimulates aggresome formation in cardiac myocytes [172], suggesting that 2-deoxyglucose enhances aggresome formation while activating autophagy.

In summary, my chemical genomic approach was able to classify autophagy inducers into several clusters that appeared to correlate with their autophagy-inducing mode of action. Analysis of individual clusters led to the demonstration (the first, to my knowledge) that Memantine and Clemastine, compounds approved by the FDA for the treatment of neurodegenerative disease, may function through the activation of ER stress-mediated autophagy. Therefore, the chemical genomic approach is expected to be useful for the functional analysis of approved drugs and for development of repositioned drugs. Moreover, my combined chemical genomic and PCA approach permitted me to identify SMK-17 as a new autophagy inducer that induces autophagy via PKC activation. In addition, I demonstrated that autophagy inducers provide the clearance of protein aggregates in cellular models of PD and HD without showing any cytotoxic effect on primary cultured rat cortical neurons, suggesting that autophagy induction may improve neuronal function in patients with PD or HD (as well as those with other proteinopathies) even after disease onset.
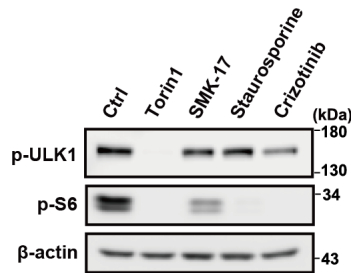
**Figure 3-44.** NGF-differentiated PC12D cells were treated with 100 nM Torin1, 10 $\mu$M SMK-17, 10 nM Staurosporine, or 5 $\mu$M Crizotinib for 1 h and then subjected to western blotting analysis with the indicated antibodies.
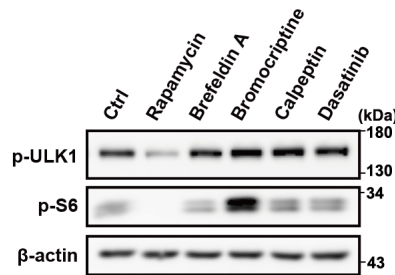


**Figure 3-45.** NGF-differentiated PC12D cells were treated with 10 $\mu$M Rapamycin (Rapa), 500 nM Brefeldin A, 10 $\mu$M Bromocriptine, 50 $\mu$M Calpeptin, or 100 $\mu$M Resveratrol for 1 h and then subjected to western blotting analysis with the indicated antibodies.
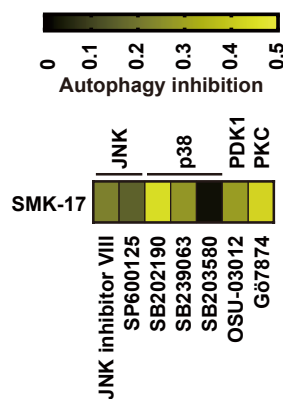


**Figure 3-46.** Heatmap analysis on the autophagy profile of SMK-17 with the indicated signal transduction modulators. The heatmap shows a gradient color scale from black to yellow, indicating the autophagy inhibition scores.

## 3.4. Materials and methods

**Reagents and antibodies**

SCADS inhibitor kits were supplied by the Molecular Profiling Committee, Grant-in-Aid for Scientific Research on Innovative Areas "Advanced Animal Model Support (AdAMS)", from the Ministry of Education, Culture, Sports, Science and Technology, Japan (KAKENHI 16H06276). Staurosporine was prepared from one such kit. 2-Deoxy-D-glucose (Cat #: D6134), Bromocriptine (Cat #: B2134), Crizotinib (Cat #: PZ0191), Dasatinib (Cat #: SML2589), Deferoxamine (Cat #: D9533), Ivermectin (Cat #: I8898), JQ1 (Cat #: SML1524), Resveratrol (Cat #: R5010), SAHA (Cat #: SML0061), and MPP$^+$ (Cat #: D048) were purchased from Sigma. Bortezomib (Cat #: S1013) and Calpeptin (Cat #: S7396) were purchased from Selleck. All-trans retinoic acid (RA, Cat #: 182-01111), Azacytidine (Cat #: 016-25361), Cyclosporine A (Cat #: 031-24931), lithium chloride (LiCl, Cat #: 123-01162), Memantine hydrochloride (Cat #: 41100-52-1), Trichostatin A (Cat #: 203-17561), and Tunicamycin (Cat #: 202-08241) were purchased from Wako. Brefeldin A (Cat #: 203729) was purchased from Calbiochem. MG132 (Cat #: 10012628) and Torin1 (Cat #: 10997) were purchased from Cayman. Rapamycin (Cat #: R-5000) was purchased from LC Laboratories. Clemastine fumarate (Cat #: C568500) was purchased from Toronto Research Chemicals. Flunarizine hydrochloride (Cat #: 0522/500) was purchased from Tocris Bioscience. SMK-17 and Sorafenib were kindly provided by the Daiichi-Sankyo Pharmaceutical Company. Gö6983 (Cat #: ab144414) and phorbol 12-myristate 13-acetate (PMA, Cat #: ab120297) were purchased from Abcam. Nerve growth factor 2.5S (NGF; Cat #: N-100) was purchased from Alomone Labs. Antibodies were obtained as follows: anti-β-actin (Cat #:

A1978), anti-LC3 (Cat #: L7543) from Sigma; anti-phospho-ULK1 (Cat #: #6888), anti-phospho-S6K (Cat #: #9204), anti-S6K (Cat #: #9202), anti-phospho-S6 (Cat #: #4858), anti-S6 (Cat #: #2217), anti-phospho-ERK (Cat #: #9101), anti-ERK (Cat #: #9102), anti-phospho-eIF2α (ser51) (Cat #: #9721), anti-eIF2α (Cat #: #9722), anti-PERK (Cat #: #3192), anti-SQSTM1/p62 (Cat #: #5114), anti-phospho-(Ser) PKC substrate (Cat #: #2261) from Cell Signaling Technology; anti-CHOP (Cat #: MA1-250) from Thermo Fisher Scientific; anti-KDEL (Cat #: ENZ-ABS679), used for GRP78 detection, from Enzo Life Science; anti-TFEB (Cat #: 13372-1-AP) from proteintech.

**Cell culture**

All cells were cultured at 37 °C in a 5% $CO_2$ environment. Rat adrenal pheochromocytoma PC12D cells [173] (obtained from Dr. Kazuo Umezawa at Keio University) were cultured in Dulbecco's modified Eagle medium (DMEM; Nissui, Cat #: 05919) supplemented with 5% fetal bovine serum, 10% horse serum, 0.6 mg/mL L-glutamine, 100 U/mL penicillin G, and 0.1 mg/mL kanamycin. Human neuroblastoma SH-SY5Y (purchased from American Type Culture Collection) cells were cultured in DMEM supplemented with 10% fetal bovine serum, L-glutamine, and antibiotics. Differentiation was achieved by 72 h treatment with 100 ng/mL NGF (for PC12D) or 7 days treatment with 1 $\mu$M RA (for SH-SY5Y).

**siRNA transfection**

Stealth siRNA against TFEB (RSS337388) and negative control siRNAs (12935300) were purchased from Invitrogen. Cells were transfected with 100 nM siRNA using Lipofectamine RNAiMAX (Invitrogen) for 48 h according to the manufacturer's instruction.

**Plasmid transfection**

To generate tfLC3 vector, sequences encoding mCherry and human LC3B were inserted into the pEGFP-C1 plasmid vector. pEGFP-N1-TFEB (No. 38119, Dr. Shawn Ferguson's lab) was purchased from Addgene. EGFP-tagged huntingtin exon1 (pEGFP-Q23 or pEGFP-Q74) was kindly provided from Dr. Shinji Saiki at Juntendo University [112]. Transfections were performed with Lipofectamine 3000 (Invitrogen) according to the manufacturer's protocol unless otherwise stated.

**Retroviral transduction**

GFP-LC3-RFP was amplified by PCR from the pMRX-IP-GFP-LC3-RFP plasmid vector (kindly provided from Dr. Noboru Mizushima at the University of Tokyo) [97] using the following primers: forward, CTCTAGACTGCCGGATCCCCCGCCGC-CACC; reverse, AGGAATTCCCGTACCACCACACTGGGATCC. GFP-LC3-RFP was then cloned into the BamHI site of the pGCDNsam vector (kindly provided from Dr. Masafumi Onodera at National Center for Child Health and Development). For the generation of retrovirus, the resulting pGCDNsam-GFP-LC3-RFP plasmid was co-transfected with pVSV-G vector (Clontech) into GP2-293 (Clontech) cells using Lipofectamine LTX (Invitrogen). Maintenance of GP2-293 cells and plasmid transfection were performed according to the manufacturer's protocol. 293GPG cells [174] were maintained according to the method described elsewhere [175], and transduced by exposure to viral supernatants harvested from the GP2-293 culture supernatants harvested on days 1, 2, and 3 with 4 μg/mL of polybrene by spinoculation at 1000 × g for 1 h at 32 °C followed by cell sorting using FACSAria III (BD Biosciences) to enrich for 293GPG cells stably expressing GFP-LC3-RFP. Virus supernatant from 293GPG-GFP-

LC3-RFP cells was harvested and concentrated as described [175]. PC12D cells stably expressing GFP-LC3-RFP cells were generated by transduction and sorting as above, using the concentrated virus from 293GPG-GFP-LC3-RFP cells.

**Autophagy flux assay**

For ratiometric autophagy flux assay, PC12D-GFP-LC3-RFP cells were seeded into a 384-well black plate (CellCarrier 384-Ultra, PerkinElmer). After 72 h differentiation by exposure to 100 ng/mL NGF, cells were treated with compounds for 24 h. Cells then were fixed with 10% formalin containing 2 $\mu$g/mL Hoechst33342 (Invitrogen, Cat #: H3570) for 30 min. Image capture and quantification of GFP and RFP intensity in cells were performed using a high-content imager (OPERA Phenix) and Harmony software ver 4.5 (PerkinElmer) or a plate-reader (SAFIRE, TECAN). For the autophagy flux assay using fluorescence imaging with tfLC3, NGF-differentiated PC12D cells were transfected with the tfLC3 vector. At 48 h after transfection, cells were treated with the indicated compounds for 8 h. Fixation, confocal microscopy were then performed as previously described [87].

**PCA, clustering, and heatmap analyses**

The rate of inhibition by each signal transduction modulator was calculated by setting the average of vehicle-treated cells at 1 and autophagy inducer-treated cells at 0. The autophagy inhibition score then was calculated by z-score normalization and analyzed by PCA, heatmap, and hierarchical clustering (based on Euclidean distance matrix and Ward's linkage method) using R ver 3.4.2 (http://www.R-project.org).

**Western blotting analysis**

Western blotting was performed according to previously published method [176].

In brief, cells were lysed with RIPA buffer, and protein lysates were separated by SDS-PAGE and transferred onto PVDF membranes. The membranes were incubated overnight at 4 °C with the primary antibodies, and then incubated for 1 h at room temperature with the appropriate HRP-conjugated secondary antibodies. Chemiluminescence was detected using the Immobilon Western Kit (Merck Millipore) and ChemiDoc XRS+ (BioRad).

**RNA extraction, RT-PCR, and Quantitative RT-PCR**

Total RNA was extracted from NGF-differentiated PC12D cells using the RNeasy Plus Mini Kit (QIAGEN). From 2 $\mu$g of total RNA, first-strand complementary DNA (cDNA) was produced using M-MLV reverse transcriptase (Promega) according to the manufacturer's instructions. For detection of *Xbp1* splicing, first-strand cDNA from PC12D cells was subjected to PCR with KOD plus polymerase (Toyobo) using primers as follows: for *Xbp1*, AGTGGAGTAAGGCTGGTGGCC and CAACAGTGTCAG-AGTCCATGGG; for *Gapdh*, TTGTGATGGGTGTGAACCAC and GGATGCAGGG-ATGATGTTCT. The amplified products were separated by electrophoresis on an 8% polyacrylamide gel (for *Xbp1* detection) and 1% agarose gel (for *Gapdh* detection) and visualized by ethidium bromide staining and ChemiDoc XRS+ (BioRad) system. The expression levels of spliced *Xbp1* and *Gapdh* were quantified using Fiji software. *Gapdh* was used to normalize transcript levels. Quantitative PCR was performed on a Thermal Cycler Dice (Takara, Shiga, Japan) using SYBR Premix Ex Taq (Takara). mRNA levels were determined with the $\Delta\Delta$Ct method and normalized to β-actin levels. The primer sequences are listed in Table 3.

**TFEB nuclear translocation assay**

PC12D cells were transfected with the pEGFP-N1-TFEB plasmid. At 48 h after

the transfection, cells were selected with 0.8 mg/mL G418 (Wako, Cat #: 071-06431) for 2 weeks. Cells stably expressing TFEB-GFP were treated with compounds for 1 h and then fixed with 3% paraformaldehyde containing 2 $\mu$g/mL Hoechst33342 for 30 min. Images were acquired using a confocal laser scanning microscope system (FV1000, Olympus). The percentage of TFEB nuclear translocation cells was quantified using Fiji software.

**Aggresome staining**

Aggresome staining was performed as described in Chapter 2. In brief, differentiated PC12D and SH-SY5Y cells seeded on coverslips were fixed with 3% paraformaldehyde, permeabilized with 0.3% Triton X-100, 1% bovine serum albumin (BSA) for 30 min, and blocked with 1% BSA in PBS-Tween for 60 min. Aggresomes were stained using the Proteostat Aggresome Detection Kit (Enzo Life Sciences) according to the manufacturer's instructions. Samples were observed under confocal microscope as above, and quantitation was performed using Fiji software.

**Clearance of mutant huntingtin**

Differentiated PC12D cells were transfected with the pEGFP-Q23 or pEGFP-Q74 plasmid. At 48 h after the transfection, cells were treated with the indicated compounds for 24 h. Cells were then fixed with 3% paraformaldehyde and observed under confocal microscope as above. Percentage of cells with GFP-huntingtin aggregates to GFP-positive cells was calculated in each sample.

**Primary neuronal cell culture and LDH assay**

The primary cultured rat cortical neurons were collected from Wister rat embryos at embryonic day 18 and incubated with 0.03% papain in Hank's balanced salt solution

(HBSS, Gibco) for 5 min at 37 °C. After dissociation with 10% FBS in neuronal culture medium (Neurobasal Plus medium (Gibco) supplemented with 0.5 mM L-glutamine, penicillin-streptomycin, 2% B-27 supplement (Gibco)), tissues were rinsed three times with HBSS, resuspended in neuronal culture medium, and filtered through a 70 $\mu$m nylon cell strainer to remove debris. The dissociated cells were plated onto poly-D-lysine-coated 96-well plates (Corning, Cat #: 354640) at a density of $3 \times 10^4$ cells/well. After 48 h, half of the medium was replaced with fresh neuronal culture medium, and cells were treated with 16.7 $\mu$g/mL Uridine (Sigma, Cat #: U3750) and 6.7 $\mu$g/mL 5-Fluoro-2'-deoxyuridine (Sigma, Cat #: F0503) for 4 days to suppress the proliferation of non-neural cell types. Cells were then maintained with half of the medium replaced every 3 or 4 days. On day 14, cells were treated with various compounds for 24 h. After treatment, 100 $\mu$L of the cell culture medium was collected, and LDH levels released from damaged cells were measured using a Cytotoxicity LDH Assay Kit-WST (Dojindo, Cat #: CK12) according to the manufacturer's instructions. The absorbance at 490 nm was measured by a plate-reader (SpectraMax iD3, Molecular Devices). The study was approved by the Animal Experiment Committee (Approval No. 310261) at Juntendo University, and were performed in accordance with national, institutional and the ARRIVE guidelines.

**Statistical analyses**

All data are presented as the mean ± standard deviation (SD). Statistical analyses were performed with the two-tailed non-paired Student's t-test unless otherwise stated. All analyses were conducted using SPSS statistics software (ver. 24; IBM).

**Table 3.** Primer sequences for qRT-PCR.

| Target | | Primer sequences |
|---|---|---|
| *Atp6v1h* | Forward | CTCAGTATGTGCAGTGTGTTGC |
| | Reverse | TACAGTTCACCCCATCTGCTTC |
| *Ctsb* | Forward | CTATCCCTCTGGAGCATGGAAC |
| | Reverse | CACATCTTGTTGCACTTGGGAG |
| *Ctsd* | Forward | CCTGGGCGATGTCTTTATTG |
| | Reverse | GGCAAAGCCGACCCTATT |
| *Lamp1* | Forward | GCACCTCCAACTATTCCCTGAA |
| | Reverse | ACAGACCCAAACCTGTCACTTT |
| *Map1lc3b* | Forward | AACAGGAGAAGGATGAAGACGG |
| | Reverse | TTGACTCAGAAGCCGAAGGTTT |
| *Sqstm1/p62* | Forward | CATCTTCCGCATCTACATTAA |
| | Reverse | TAGCGAGTTCCCACCACA |
| *Tfeb* | Forward | ACAAGGCACCATCCTCA |
| | Reverse | CCAGCTCGGCCATATTCA |
| *Uvrag* | Forward | ACTCCAGACTTGAGGCAAAC |
| | Reverse | ACAGATACTCACCATCTGACC |
| *Vps18* | Forward | GCTGATGATTCGCTCCATTGAC |
| | Reverse | AGTCTGGTAGCTGTATCCCTGT |
| *β-actin* | Forward | CCTCTGAACCCTAAGGCCAA |
| | Reverse | GCCTGGATGGCTACGTACA |

# Chapter 4

# Conclusion

Although the usefulness of chemical biology has been recognized by researchers in medicine, neurobiology, and pharmacology, chemical biological studies on neurodegenerative disorders are still not sufficiently conducted, compared to cancer research. In the present study, I addressed to develop novel drug seeds or strategies for PD treatment using chemical biological approach, which provides the findings that activating the cellular redox pathway and intracellular degradation pathway can be potent therapeutic interventions in PD (Figure 4).

As described in Chapter 2, I focused bilirubin, the end product of heme redox metabolism, identified as a novel biomarker for PD. By using chemical biological approach, I established the unique screening system targeting intracellular bilirubin level and identified a novel PD drug seed, BRUP-1. BRUP-1 directly inhibited the association of Keap1 with Nrf2 leading to Nrf2 activation, which induces HO-1 expression and subsequent bilirubin production. Bilirubin up-regulation by BRUP-1 potently suppressed neurotoxin-induced ROS production, protein aggregates formation, and ultimately cell death. These findings not only provide a new member of Keap1-Nrf2 direct inhibitors but also suggest chemical modulation of heme metabolism can be a novel therapeutic strategy to treat PD.

As described in Chapter 3, I performed the analyses on signal transduction pathways and on the effectiveness of autophagy inducers in cellular models of neurodegenerative diseases including PD. My chemical genomic approach enabled me to classify autophagy inducers into several clusters that appeared to correlate with their autophagy-inducing modes of action. Moreover, I demonstrated that autophagy inducers including SMK-17 that I identified as a new autophagy inducer, showed clearing effects of protein aggregates observed in cellular models of PD and HD, suggesting that

autophagy induction may improve neuronal function in patients with PD and HD (as well as those with other proteinopathies) even after disease onset.

Taken together, my two chemical biological researches on PD lead to the findings of two novel bioactive compounds, BRUP-1 and SMK-17 that activates bilirubin production and autophagy, respectively. Chemical genetical/genomical approaches provided me to show the mechanisms of action of these compounds. Furthermore, my results suggest that chemical intervention in heme redox and/or autophagy pathways can be novel and effective strategies to treat PD. In conclusion, the application of chemical biology is a powerful method to contribute to not only the understanding the biology but also development of novel therapeutic strategies in neurodegenerative disorders including PD.
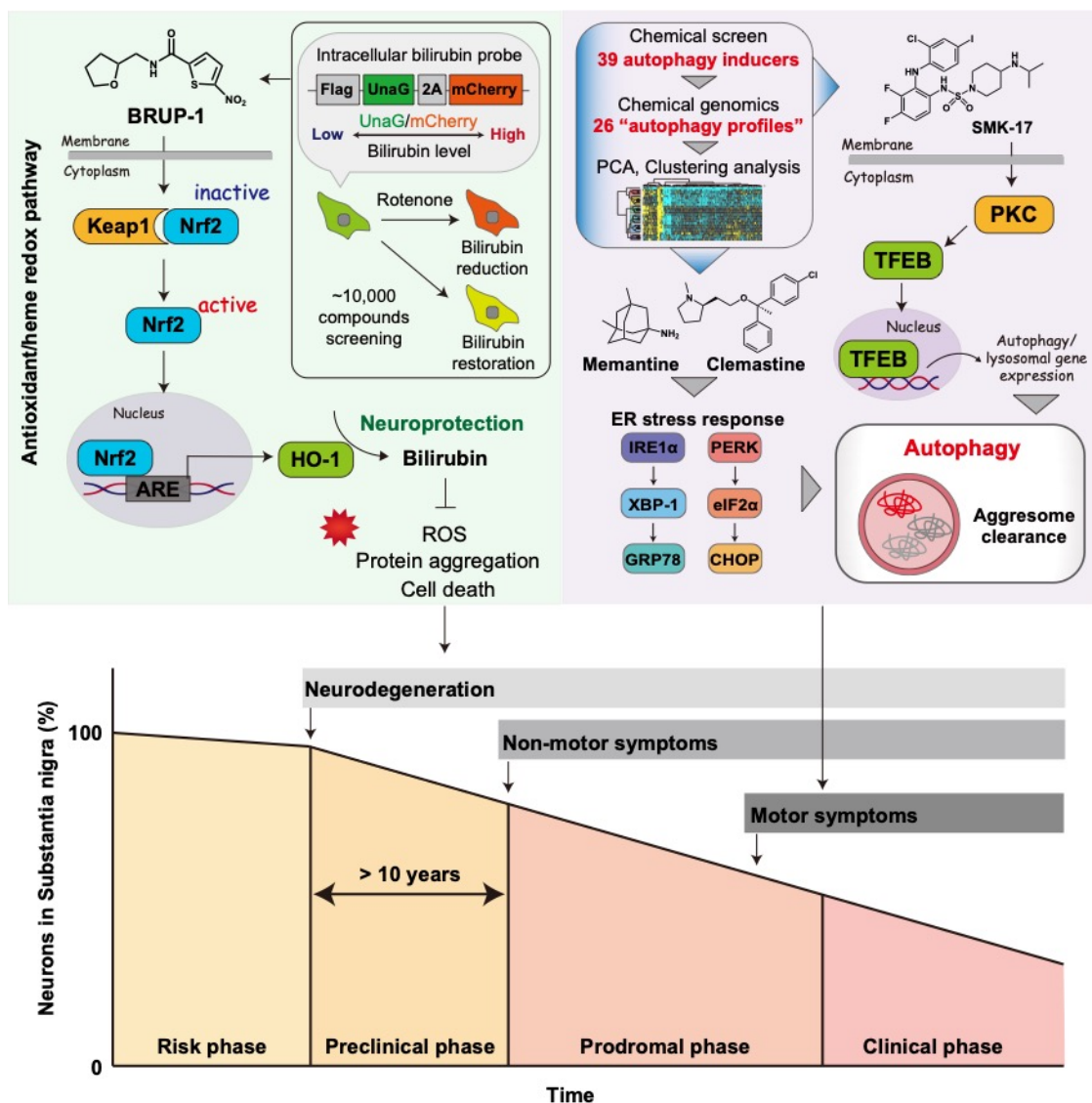
**Figure 4.** Overview of the present study. (Left) Graphical summary of the study described in Chapter 2: BRUP-1, an intracellular bilirubin modulator, exerts neuroprotective activity in a cellular Parkinson's disease model. (Right) Graphical summary of the study described in Chapter 3: A chemical genomics-aggrephagy integrated method studying functional analysis of autophagy inducers. (Down) Pathological phases in PD and proposal commencing time of the intervention using modulators of bilirubin metabolism and autophagy (Figure adapted from [177]).

# References

1.      Liu J, Farmer JD, Jr., Lane WS, et al. Calcineurin is a common target of cyclophilin-cyclosporin A and FKBP-FK506 complexes. Cell. 1991 Aug 23;66(4):807-15.

2.      Bredel M, Jacoby E. Chemogenomics: an emerging strategy for rapid target and drug discovery. Nat Rev Genet. 2004 Apr;5(4):262-75.

3.      Chan TF, Carvalho J, Riles L, et al. A chemical genomics approach toward understanding the global functions of the target of rapamycin protein (TOR). Proc Natl Acad Sci U S A. 2000 Nov 21;97(24):13227-32.

4.      Soga S, Neckers LM, Schulte TW, et al. KF25706, a novel oxime derivative of radicicol, exhibits in vivo antitumor activity via selective depletion of Hsp90 binding signaling molecules. Cancer Res. 1999 Jun 15;59(12):2931-8.

5.      Lesage S, Brice A. Parkinson's disease: from monogenic forms to genetic susceptibility factors. Hum Mol Genet. 2009 Apr 15;18(R1):R48-59.

6.      Global, regional, and national incidence, prevalence, and years lived with disability for 354 diseases and injuries for 195 countries and territories, 1990-2017: a systematic analysis for the Global Burden of Disease Study 2017. Lancet. 2018 Nov 10;392(10159):1789-1858.

7.      Espay AJ, Morgante F, Merola A, et al. Levodopa-induced dyskinesia in Parkinson disease: Current and evolving concepts. Ann Neurol. 2018 Dec;84(6):797-811.

8.      Zeng XS, Geng WS, Jia JJ, et al. Cellular and Molecular Basis of Neurodegeneration in Parkinson Disease. Front Aging Neurosci. 2018;10:109.

9.      Noyce AJ, Bestwick JP, Silveira-Moriyama L, et al. Meta-analysis of early nonmotor features and risk factors for Parkinson disease. Ann Neurol. 2012 Dec;72(6):893-901.

10.     Quinones MP, Kaddurah-Daouk R. Metabolomics tools for identifying biomarkers for neuropsychiatric diseases. Neurobiol Dis. 2009 Aug;35(2):165-76.

11.     Athauda D, Foltynie T. The ongoing pursuit of neuroprotective therapies in Parkinson disease. Nat Rev Neurol. 2015 Jan;11(1):25-40.

12.     Jankovic J. Parkinson's disease: clinical features and diagnosis. J Neurol Neurosurg Psychiatry. 2008 Apr;79(4):368-76.

13.     Saiki S, Sato S, Hattori N. Molecular pathogenesis of Parkinson's disease: update. J Neurol Neurosurg Psychiatry. 2012 Apr;83(4):430-6.

14.     Schipper HM, Liberman A, Stopa EG. Neural heme oxygenase-1 expression in idiopathic Parkinson's disease. Exp Neurol. 1998 Mar;150(1):60-8.

15.     Beal MF. Experimental models of Parkinson's disease. Nat Rev Neurosci. 2001 May;2(5):325-34.

16.     Bae JW, Kim MJ, Jang CG, et al. Protective effects of heme oxygenase-1 against MPP(+)-induced cytotoxicity in PC-12 cells. Neurol Sci. 2010 Jun;31(3):307-13.

17.     Falkenburger BH, Saridaki T, Dinter E. Cellular models for Parkinson's disease. J Neurochem. 2016 Oct;139 Suppl 1:121-130.

18.     Panahian N, Yoshiura M, Maines MD. Overexpression of heme oxygenase-1 is neuroprotective in a model of permanent middle cerebral artery occlusion in transgenic mice. J Neurochem. 1999 Mar;72(3):1187-203.

19.     Jazwa A, Cuadrado A. Targeting heme oxygenase-1 for neuroprotection and neuroinflammation in neurodegenerative diseases. Curr Drug Targets. 2010 Dec;11(12):1517-31.

20.     Stocker R, Yamamoto Y, McDonagh AF, et al. Bilirubin is an antioxidant of possible physiological importance. Science. 1987 Feb 27;235(4792):1043-6.

21.     Sedlak TW, Saleh M, Higginson DS, et al. Bilirubin and glutathione have complementary antioxidant and cytoprotective roles. Proc Natl Acad Sci U S A. 2009 Mar 31;106(13):5171-6.

22.     Jansen T, Daiber A. Direct Antioxidant Properties of Bilirubin and Biliverdin. Is there a Role for Biliverdin Reductase? Front Pharmacol. 2012;3:30.

23.     Yamaguchi T, Komoda Y, Nakajima H. Biliverdin-IX alpha reductase and biliverdin-IX beta reductase from human liver. Purification and characterization. J Biol Chem. 1994 Sep 30;269(39):24343-8.

24.     Ryter SW, Morse D, Choi AM. Carbon monoxide and bilirubin: potential therapies for pulmonary/vascular injury and disease. Am J Respir Cell Mol Biol. 2007 Feb;36(2):175-82.

25.     Barone E, Di Domenico F, Mancuso C, et al. The Janus face of the heme oxygenase/biliverdin reductase system in Alzheimer disease: it's time for reconciliation. Neurobiol Dis. 2014 Feb;62:144-59.

26.     Jeney V, Balla J, Yachie A, et al. Pro-oxidant and cytotoxic effects of circulating heme. Blood. 2002 Aug 1;100(3):879-87.

27.     Yanatori I, Tabuchi M, Kawai Y, et al. Heme and non-heme iron transporters in non-polarized and polarized cells. BMC Cell Biol. 2010 Jun 4;11:39.

28.     Otterbein LE, Bach FH, Alam J, et al. Carbon monoxide has anti-inflammatory effects involving the mitogen-activated protein kinase pathway. Nat Med. 2000 Apr;6(4):422-8.

29.     Almeida AS, Queiroga CS, Sousa MF, et al. Carbon monoxide modulates apoptosis by reinforcing oxidative metabolism in astrocytes: role of Bcl-2. J Biol Chem. 2012 Mar 30;287(14):10761-70.

30.     Gowda S, Desai PB, Hull VV, et al. A review on laboratory liver function tests. Pan Afr Med J. 2009 Nov 22;3:17.

31.     Inoguchi T, Fukuhara S, Yamato M, et al. Serum bilirubin level is a strong predictor for disability in activities in daily living (ADL) in Japanese elderly patients with diabetes. Sci Rep. 2019 May 8;9(1):7069.

32.     Moccia M, Picillo M, Erro R, et al. Increased bilirubin levels in de novo Parkinson's disease. Eur J Neurol. 2015 Jun;22(6):954-9.

33.     Qin XL, Zhang QS, Sun L, et al. Lower Serum Bilirubin and Uric Acid Concentrations in Patients with Parkinson's Disease in China. Cell Biochem Biophys. 2015 May;72(1):49-56.

34.     Hatano T, Saiki S, Okuzumi A, et al. Identification of novel biomarkers for Parkinson's disease by metabolomic technologies. J Neurol Neurosurg Psychiatry. 2016 Mar;87(3):295-301.

35.     Lee DY, Oh M, Kim SJ, et al. Bilirubin-Related Differential Striatal [18F]FP-CIT Uptake in Parkinson Disease. Clin Nucl Med. 2019 Nov;44(11):855-859.

36.     Macias-Garcia D, Mendez-Del Barrio C, Jesus S, et al. Increased bilirubin levels in Parkinson's disease. Parkinsonism Relat Disord. 2019 Jun;63:213-216.

37.     Kumagai A, Ando R, Miyatake H, et al. A bilirubin-inducible fluorescent protein from eel muscle. Cell. 2013 Jun 20;153(7):1602-11.

38.     Takeda TA, Mu A, Tai TT, et al. Continuous de novo biosynthesis of haem and its rapid turnover to bilirubin are necessary for cytoprotection against cell damage. Sci Rep. 2015 May 20;5:10488.

39.     Iwatani S, Nakamura H, Kurokawa D, et al. Fluorescent protein-based detection of unconjugated bilirubin in newborn serum. Sci Rep. 2016 Jun 21;6:28489.

40.     Szymczak-Workman AL, Vignali KM, Vignali DA. Design and construction of 2A peptide-linked multicistronic vectors. Cold Spring Harb Protoc. 2012 Feb 1;2012(2):199-204.

41.     Exner N, Lutz AK, Haass C, et al. Mitochondrial dysfunction in Parkinson's disease: molecular mechanisms and pathophysiological consequences. EMBO J. 2012 Jun 26;31(14):3038-62.

42.     Foresti R, Motterlini R. The heme oxygenase pathway and its interaction with nitric oxide in the control of cellular homeostasis. Free Radic Res. 1999 Dec;31(6):459-75.

43.     Barnham KJ, Masters CL, Bush AI. Neurodegenerative diseases and oxidative stress. Nat Rev Drug Discov. 2004 Mar;3(3):205-14.

44.     Maghzal GJ, Leck MC, Collinson E, et al. Limited role for the bilirubin-biliverdin redox amplification cycle in the cellular antioxidant protection by biliverdin reductase. J Biol Chem. 2009 Oct 23;284(43):29251-9.

45.     Mancuso C. Bilirubin and brain: A pharmacological approach. Neuropharmacology. 2017 May 15;118:113-123.

46.     Dodson M, Redmann M, Rajasekaran NS, et al. KEAP1-NRF2 signalling and autophagy in protection against oxidative and reductive proteotoxicity. Biochem J. 2015 Aug 1;469(3):347-55.

47.     Martin D, Rojo AI, Salinas M, et al. Regulation of heme oxygenase-1 expression through the phosphatidylinositol 3-kinase/Akt pathway and the Nrf2 transcription factor in response to the antioxidant phytochemical carnosol. J Biol Chem. 2004 Mar 5;279(10):8919-29.

48.     Jain A, Lamark T, Sjottem E, et al. p62/SQSTM1 is a target gene for transcription factor NRF2 and creates a positive feedback loop by inducing antioxidant response element-driven gene transcription. J Biol Chem. 2010 Jul 16;285(29):22576-91.

49.     Villeneuve NF, Lau A, Zhang DD. Regulation of the Nrf2-Keap1 antioxidant response by the

ubiquitin proteasome system: an insight into cullin-ring ubiquitin ligases. Antioxid Redox Signal. 2010 Dec 1;13(11):1699-712.

50.    Lo SC, Li X, Henzl MT, et al. Structure of the Keap1:Nrf2 interface provides mechanistic insight into Nrf2 signaling. Embo J. 2006 Aug 9;25(15):3605-17.

51.    Chen Y, Inoyama D, Kong AN, et al. Kinetic analyses of Keap1-Nrf2 interaction and determination of the minimal Nrf2 peptide sequence required for Keap1 binding using surface plasmon resonance. Chem Biol Drug Des. 2011 Dec;78(6):1014-21.

52.    Barone MC, Sykiotis GP, Bohmann D. Genetic activation of Nrf2 signaling is sufficient to ameliorate neurodegenerative phenotypes in a Drosophila model of Parkinson's disease. Dis Model Mech. 2011 Sep;4(5):701-7.

53.    He Q, Song N, Jia F, et al. Role of alpha-synuclein aggregation and the nuclear factor E2-related factor 2/heme oxygenase-1 pathway in iron-induced neurotoxicity. Int J Biochem Cell Biol. 2013 Jun;45(6):1019-30.

54.    Gan L, Johnson JA. Oxidative damage and the Nrf2-ARE pathway in neurodegenerative diseases. Biochim Biophys Acta. 2014 Aug;1842(8):1208-18.

55.    Kulasekaran G, Ganapasam S. Neuroprotective efficacy of naringin on 3-nitropropionic acid-induced mitochondrial dysfunction through the modulation of Nrf2 signaling pathway in PC12 cells. Mol Cell Biochem. 2015 Nov;409(1-2):199-211.

56.    Tsou YH, Shih CT, Ching CH, et al. Treadmill exercise activates Nrf2 antioxidant system to protect the nigrostriatal dopaminergic neurons from MPP$^+$ toxicity. Exp Neurol. 2015 Jan;263:50-62.

57.    Zhao P, Yang X, Yang L, et al. Neuroprotective effects of fingolimod in mouse models of Parkinson's disease. FASEB J. 2017 Jan;31(1):172-179.

58.    Wakabayashi K, Tanji K, Odagiri S, et al. The Lewy body in Parkinson's disease and related neurodegenerative disorders. Mol Neurobiol. 2013 Apr;47(2):495-508.

59.    Yu Q, Zhang H, Li Y, et al. UCH-L1 Inhibition Suppresses tau Aggresome Formation during Proteasomal Impairment. Mol Neurobiol. 2018 May;55(5):3812-3821.

60.    Olzmann JA, Li L, Chin LS. Aggresome formation and neurodegenerative diseases: therapeutic implications. Curr Med Chem. 2008;15(1):47-60.

61.    Butterfield DA, Reed T, Newman SF, et al. Roles of amyloid beta-peptide-associated oxidative stress and brain protein modifications in the pathogenesis of Alzheimer's disease and mild cognitive impairment. Free Radic Biol Med. 2007 Sep 1;43(5):658-77.

62.    Bakken AF, Thaler MM, Schmid R. Metabolic regulation of heme catabolism and bilirubin production. I. Hormonal control of hepatic heme oxygenase activity. J Clin Invest. 1972 Mar;51(3):530-6.

63.    Sun J, Hoshino H, Takaku K, et al. Hemoprotein Bach1 regulates enhancer availability of heme

oxygenase-1 gene. EMBO J. 2002 Oct 1;21(19):5216-24.

64. Kitamuro T, Takahashi K, Ogawa K, et al. Bach1 functions as a hypoxia-inducible repressor for the heme oxygenase-1 gene in human cells. J Biol Chem. 2003 Mar 14;278(11):9125-33.

65. Suzuki H, Tashiro S, Sun J, et al. Cadmium induces nuclear export of Bach1, a transcriptional repressor of heme oxygenase-1 gene. J Biol Chem. 2003 Dec 5;278(49):49246-53.

66. Farombi EO, Surh YJ. Heme oxygenase-1 as a potential therapeutic target for hepatoprotection. J Biochem Mol Biol. 2006 Sep 30;39(5):479-91.

67. Nguyen T, Nioi P, Pickett CB. The Nrf2-antioxidant response element signaling pathway and its activation by oxidative stress. J Biol Chem. 2009 May 15;284(20):13291-5.

68. Theodore M, Kawai Y, Yang J, et al. Multiple nuclear localization signals function in the nuclear import of the transcription factor Nrf2. J Biol Chem. 2008 Apr 4;283(14):8984-94.

69. Dinkova-Kostova AT, Holtzclaw WD, Cole RN, et al. Direct evidence that sulfhydryl groups of Keap1 are the sensors regulating induction of phase 2 enzymes that protect against carcinogens and oxidants. Proc Natl Acad Sci U S A. 2002 Sep 3;99(18):11908-13.

70. Zhang DD, Hannink M. Distinct cysteine residues in Keap1 are required for Keap1-dependent ubiquitination of Nrf2 and for stabilization of Nrf2 by chemopreventive agents and oxidative stress. Mol Cell Biol. 2003 Nov;23(22):8137-51.

71. Magesh S, Chen Y, Hu L. Small molecule modulators of Keap1-Nrf2-ARE pathway as potential preventive and therapeutic agents. Med Res Rev. 2012 Jul;32(4):687-726.

72. Jiang ZY, Lu MC, You QD. Discovery and Development of Kelch-like ECH-Associated Protein 1. Nuclear Factor Erythroid 2-Related Factor 2 (KEAP1:NRF2) Protein-Protein Interaction Inhibitors: Achievements, Challenges, and Future Directions. J Med Chem. 2016 Dec 22;59(24):10837-10858.

73. Cuadrado A, Rojo AI, Wells G, et al. Therapeutic targeting of the NRF2 and KEAP1 partnership in chronic diseases. Nat Rev Drug Discov. 2019 Apr;18(4):295-317.

74. Castellani R, Smith MA, Richey GL, et al. Glycoxidation and oxidative stress in Parkinson disease and diffuse Lewy body disease. Brain Research. 1996;737(1-2):195-200.

75. Schipper HM. Experimental induction of corpora amylacea in adult rat brain. Microscopy Research and Technique. 1998;43(1):43-48.

76. Ramsey CP, Glass CA, Montgomery MB, et al. Expression of Nrf2 in neurodegenerative diseases. J Neuropathol Exp Neurol. 2007 Jan;66(1):75-85.

77. Jakel RJ, Kern JT, Johnson DA, et al. Induction of the protective antioxidant response element pathway by 6-hydroxydopamine in vivo and in vitro. Toxicol Sci. 2005 Sep;87(1):176-86.

78. Innamorato NG, Jazwa A, Rojo AI, et al. Different susceptibility to the Parkinson's toxin MPTP in mice lacking the redox master regulator Nrf2 or its target gene heme oxygenase-1. PLoS One. 2010 Jul 28;5(7):e11838.

79.   Kawaguchi Y, Kovacs JJ, McLaurin A, et al. The Deacetylase HDAC6 Regulates Aggresome Formation and Cell Viability in Response to Misfolded Protein Stress. Cell. 2003;115(6):727-738.

80.   Taylor JP, Tanaka F, Robitschek J, et al. Aggresomes protect cells by enhancing the degradation of toxic polyglutamine-containing protein. Hum Mol Genet. 2003 Apr 1;12(7):749-57.

81.   Tanaka M, Kim YM, Lee G, et al. Aggresomes formed by alpha-synuclein and synphilin-1 are cytoprotective. J Biol Chem. 2004 Feb 6;279(6):4625-31.

82.   Hideshima T, Bradner JE, Wong J, et al. Small-molecule inhibition of proteasome and aggresome function induces synergistic antitumor activity in multiple myeloma. Proc Natl Acad Sci U S A. 2005 Jun 14;102(24):8567-72.

83.   Kataura T, Saiki S, Ishikawa KI, et al. BRUP-1, an intracellular bilirubin modulator, exerts neuroprotective activity in a cellular Parkinson's disease model. J Neurochem. 2020 Mar 3.

84.   Wang Q, Liu Y, Zhou J. Neuroinflammation in Parkinson's disease and its potential as therapeutic target. Transl Neurodegener. 2015;4:19.

85.   Vasavda C, Kothari R, Malla AP, et al. Bilirubin Links Heme Metabolism to Neuroprotection by Scavenging Superoxide. Cell Chem Biol. 2019 Oct 17;26(10):1450-1460.e7.

86.   Fujimaki T, Saiki S, Tashiro E, et al. Identification of licopyranocoumarin and glycyrurol from herbal medicines as neuroprotective compounds for Parkinson's disease. PLoS One. 2014;9(6):e100395.

87.   Igarashi Y, Matsuoka N, In Y, et al. Nonthmicin, a Polyether Polyketide Bearing a Halogen-Modified Tetronate with Neuroprotective and Antiinvasive Activity from Actinomadura sp. Org Lett. 2017 Mar 17;19(6):1406-1409.

88.   Klionsky DJ, Abdelmohsen K, Abe A, et al. Guidelines for the use and interpretation of assays for monitoring autophagy (3rd edition). Autophagy. 2016;12(1):1-222.

89.   Nixon RA. The role of autophagy in neurodegenerative disease. Nat Med. 2013 Aug;19(8):983-97.

90.   Sarkar S. Regulation of autophagy by mTOR-dependent and mTOR-independent pathways: autophagy dysfunction in neurodegenerative diseases and therapeutic application of autophagy enhancers. Biochem Soc Trans. 2013 Oct;41(5):1103-30.

91.   Williams A, Sarkar S, Cuddon P, et al. Novel targets for Huntington's disease in an mTOR-independent autophagy pathway. Nat Chem Biol. 2008 May;4(5):295-305.

92.   Dunlop EA, Tee AR. mTOR and autophagy: a dynamic relationship governed by nutrients and energy. Semin Cell Dev Biol. 2014 Dec;36:121-9.

93.   Martina JA, Chen Y, Gucek M, et al. MTORC1 functions as a transcriptional regulator of autophagy by preventing nuclear transport of TFEB. Autophagy. 2012 Jun;8(6):903-14.

94.   Zhou J, Liao W, Yang J, et al. FOXO3 induces FOXO1-dependent autophagy by activating the AKT1 signaling pathway. Autophagy. 2012 Dec;8(12):1712-23.

95.     Song S, Tan J, Miao Y, et al. Crosstalk of ER stress-mediated autophagy and ER-phagy: Involvement of UPR and the core autophagy machinery. J Cell Physiol. 2018 May;233(5):3867-3874.

96.     Magi S, Tashiro E, Imoto M. A chemical genomic study identifying diversity in cell migration signaling in cancer cells. Sci Rep. 2012;2:823.

97.     Kaizuka T, Morishita H, Hama Y, et al. An Autophagic Flux Probe that Releases an Internal Control. Mol Cell. 2016 Nov 17;64(4):835-849.

98.     Xi H, Kurtoglu M, Liu H, et al. 2-Deoxy-D-glucose activates autophagy via endoplasmic reticulum stress rather than ATP depletion. Cancer Chemother Pharmacol. 2011 Apr;67(4):899-910.

99.     Kornicka K, Szlapka-Kosarzewska J, Smieszek A, et al. 5-Azacytydine and resveratrol reverse senescence and ageing of adipose stem cells via modulation of mitochondrial dynamics and autophagy. J Cell Mol Med. 2019 Jan;23(1):237-259.

100.    Selimovic D, Porzig BB, El-Khattouti A, et al. Bortezomib/proteasome inhibitor triggers both apoptosis and autophagy-dependent pathways in melanoma cells. Cell Signal. 2013 Jan;25(1):308-18.

101.    Ding WX, Ni HM, Gao W, et al. Differential effects of endoplasmic reticulum stress-induced autophagy on cell survival. J Biol Chem. 2007 Feb 16;282(7):4702-10.

102.    Geng X, Ma L, Li Z, et al. Bromocriptine Induces Autophagy-Dependent Cell Death in Pituitary Adenomas. World Neurosurg. 2017 Apr;100:407-416.

103.    Apolloni S, Fabbrizio P, Amadio S, et al. Actions of the antihistaminergic clemastine on presymptomatic SOD1-G93A mice ameliorate ALS disease progression. J Neuroinflammation. 2016 Aug 22;13(1):191.

104.    You L, Shou J, Deng D, et al. Crizotinib induces autophagy through inhibition of the STAT3 pathway in multiple lung cancer cell lines. Oncotarget. 2015 Nov 24;6(37):40268-82.

105.    Yoo YM, Jeung EB. Melatonin suppresses cyclosporine A-induced autophagy in rat pituitary GH3 cells. J Pineal Res. 2010 Apr;48(3):204-11.

106.    Milano V, Piao Y, LaFortune T, et al. Dasatinib-induced autophagy is enhanced in combination with temozolomide in glioma. Mol Cancer Ther. 2009 Feb;8(2):394-406.

107.    Wu Y, Li X, Xie W, et al. Neuroprotection of deferoxamine on rotenone-induced injury via accumulation of HIF-1 alpha and induction of autophagy in SH-SY5Y cells. Neurochem Int. 2010 Oct;57(3):198-205.

108.    Zheng ZY, Li J, Li F, et al. Induction of N-Ras degradation by flunarizine-mediated autophagy. Sci Rep. 2018 Nov 16;8(1):16932.

109.    Dou Q, Chen HN, Wang K, et al. Ivermectin Induces Cytostatic Autophagy by Blocking the PAK1/Akt Axis in Breast Cancer. Cancer Res. 2016 Aug 1;76(15):4457-69.

110. Sakamaki JI, Wilkinson S, Hahn M, et al. Bromodomain Protein BRD4 Is a Transcriptional Repressor of Autophagy and Lysosomal Function. Mol Cell. 2017 May 18;66(4):517-532.e9.

111. Sarkar S, Floto RA, Berger Z, et al. Lithium induces autophagy by inhibiting inositol monophosphatase. J Cell Biol. 2005 Sep 26;170(7):1101-11.

112. Hirano K, Fujimaki M, Sasazawa Y, et al. Neuroprotective effects of memantine via enhancement of autophagy. Biochem Biophys Res Commun. 2019 Oct 8;518(1):161-170.

113. Bao W, Gu Y, Ta L, et al. Induction of autophagy by the MG132 proteasome inhibitor is associated with endoplasmic reticulum stress in MCF7 cells. Mol Med Rep. 2016 Jan;13(1):796-804.

114. Jung CH, Ro SH, Cao J, et al. mTOR regulation of autophagy. FEBS Lett. 2010 Apr 2;584(7):1287-95.

115. Morselli E, Marino G, Bennetzen MV, et al. Spermidine and resveratrol induce autophagy by distinct pathways converging on the acetylproteome. J Cell Biol. 2011 Feb 21;192(4):615-29.

116. Oh M, Choi IK, Kwon HJ. Inhibition of histone deacetylase1 induces autophagy. Biochem Biophys Res Commun. 2008 May 16;369(4):1179-83.

117. Kiga M, Nakayama A, Shikata Y, et al. SMK-17, a MEK1/2-specific inhibitor, selectively induces apoptosis in beta-catenin-mutated tumors. Sci Rep. 2015 Feb 2;5:8155.

118. Prieto-Dominguez N, Ordonez R, Fernandez A, et al. Modulation of Autophagy by Sorafenib: Effects on Treatment Response. Front Pharmacol. 2016;7:151.

119. Ha JY, Kim JS, Kim SE, et al. Simultaneous activation of mitophagy and autophagy by staurosporine protects against dopaminergic neuronal cell death. Neurosci Lett. 2014 Feb 21;561:101-6.

120. Thoreen CC, Kang SA, Chang JW, et al. An ATP-competitive mammalian target of rapamycin inhibitor reveals rapamycin-resistant functions of mTORC1. J Biol Chem. 2009 Mar 20;284(12):8023-32.

121. Zhang J, Ng S, Wang J, et al. Histone deacetylase inhibitors induce autophagy through FOXO1-dependent pathways. Autophagy. 2015 Apr 3;11(4):629-42.

122. Ogata M, Hino S, Saito A, et al. Autophagy is activated for cell survival after endoplasmic reticulum stress. Mol Cell Biol. 2006 Dec;26(24):9220-31.

123. Yang JW, Zhang QH, Liu T. Autophagy facilitates anticancer effect of 5-fluorouracil in HCT-116 cells. J Cancer Res Ther. 2018 Dec;14(Supplement):S1141-s1147.

124. Cortes CL, Veiga SR, Almacellas E, et al. Effect of low doses of actinomycin D on neuroblastoma cell lines. Mol Cancer. 2016 Jan 4;15:1.

125. Cabrera S, Maciel M, Herrera I, et al. Essential role for the ATG4B protease and autophagy in bleomycin-induced pulmonary fibrosis. Autophagy. 2015 Apr 3;11(4):670-84.

126. Vanzo R, Bartkova J, Merchut-Maya JM, et al. Autophagy role(s) in response to oncogenes and DNA replication stress. Cell Death Differ. 2019 Aug 14.

127. Kwon KY, Viollet B, Yoo OJ. CCCP induces autophagy in an AMPK-independent manner. Biochem Biophys Res Commun. 2011 Dec 16;416(3-4):343-8.

128. Han W, Sun J, Feng L, et al. Autophagy inhibition enhances daunorubicin-induced apoptosis in K562 cells. PLoS One. 2011;6(12):e28491.

129. Koleini N, Kardami E. Autophagy and mitophagy in the context of doxorubicin-induced cardiotoxicity. Oncotarget. 2017 Jul 11;8(28):46663-46680.

130. Maskey D, Yousefi S, Schmid I, et al. ATG5 is induced by DNA-damaging agents and promotes mitotic catastrophe independent of autophagy. Nat Commun. 2013;4:2130.

131. Ding WX, Ni HM, Gao W, et al. Linking of autophagy to ubiquitin-proteasome system is important for the regulation of endoplasmic reticulum stress and cell viability. Am J Pathol. 2007 Aug;171(2):513-24.

132. Ojha R, Jha V, Singh SK. Gemcitabine and mitomycin induced autophagy regulates cancer stem cell pool in urothelial carcinoma cells. Biochim Biophys Acta. 2016 Feb;1863(2):347-59.

133. Zamora A, Alves M, Chollet C, et al. Paclitaxel induces lymphatic endothelial cells autophagy to promote metastasis. Cell Death Dis. 2019 Dec 20;10(12):956.

134. Dupont N, Jiang S, Pilli M, et al. Autophagy-based unconventional secretory pathway for extracellular delivery of IL-1beta. Embo J. 2011 Nov 8;30(23):4701-11.

135. Wu Q, Wang X, Nepovimova E, et al. Mechanism of cyclosporine A nephrotoxicity: Oxidative stress, autophagy, and signalings. Food Chem Toxicol. 2018 Aug;118:889-907.

136. Atkins C, Liu Q, Minthorn E, et al. Characterization of a novel PERK kinase inhibitor with antitumor and antiangiogenic activity. Cancer Res. 2013 Mar 15;73(6):1993-2002.

137. Bertolotti A, Zhang Y, Hendershot LM, et al. Dynamic interaction of BiP and ER stress transducers in the unfolded-protein response. Nat Cell Biol. 2000 Jun;2(6):326-32.

138. Harding HP, Zhang Y, Ron D. Protein translation and folding are coupled by an endoplasmic-reticulum-resident kinase. Nature. 1999 Jan 21;397(6716):271-4.

139. Pakos-Zebrucka K, Koryga I, Mnich K, et al. The integrated stress response. EMBO Rep. 2016 Oct;17(10):1374-1395.

140. Kimura S, Noda T, Yoshimori T. Dissection of the autophagosome maturation process by a novel reporter protein, tandem fluorescent-tagged LC3. Autophagy. 2007 Sep-Oct;3(5):452-60.

141. Kiga M, Tanzawa F, Iwasaki S, et al. Antitumor effects of novel highly hydrophilic and non-ATP-competitive MEK1/2 inhibitor, SMK-17. Anticancer Drugs. 2012 Jan;23(1):119-30.

142. Settembre C, Di Malta C, Polito VA, et al. TFEB links autophagy to lysosomal biogenesis. Science. 2011 Jun 17;332(6036):1429-33.

143. Settembre C, Zoncu R, Medina DL, et al. A lysosome-to-nucleus signalling mechanism senses and regulates the lysosome via mTOR and TFEB. Embo J. 2012 Mar 7;31(5):1095-108.

144. Rusmini P, Cortese K, Crippa V, et al. Trehalose induces autophagy via lysosomal-mediated TFEB

activation in models of motoneuron degeneration. Autophagy. 2019 Apr;15(4):631-651.

145.    Li Y, Xu M, Ding X, et al. Protein kinase C controls lysosome biogenesis independently of mTORC1. Nat Cell Biol. 2016 Oct;18(10):1065-77.

146.    Lin MT, Beal MF. Mitochondrial dysfunction and oxidative stress in neurodegenerative diseases. Nature. 2006 Oct 19;443(7113):787-95.

147.    Shinjo S, Mizotani Y, Tashiro E, et al. Comparative analysis of the expression patterns of UPR-target genes caused by UPR-inducing compounds. Biosci Biotechnol Biochem. 2013;77(4):729-35.

148.    Reisberg B, Doody R, Stoffler A, et al. Memantine in moderate-to-severe Alzheimer's disease. N Engl J Med. 2003 Apr 3;348(14):1333-41.

149.    Verhagen Metman L, Del Dotto P, van den Munckhof P, et al. Amantadine as treatment for dyskinesias and motor fluctuations in Parkinson's disease. Neurology. 1998 May;50(5):1323-6.

150.    Johnson JW, Kotermanski SE. Mechanism of action of memantine. Curr Opin Pharmacol. 2006 Feb;6(1):61-7.

151.    Hayashi T. The Sigma-1 Receptor in Cellular Stress Signaling. Front Neurosci. 2019;13:733.

152.    Kubickova J, Lencesova L, Csaderova L, et al. Haloperidol Affects Plasticity of Differentiated NG-108 Cells Through sigma1R/IP3R1 Complex. Cell Mol Neurobiol. 2018 Jan;38(1):181-194.

153.    Nishitoh H, Matsuzawa A, Tobiume K, et al. ASK1 is essential for endoplasmic reticulum stress-induced neuronal cell death triggered by expanded polyglutamine repeats. Genes Dev. 2002 Jun 1;16(11):1345-55.

154.    Margariti A, Li H, Chen T, et al. XBP1 mRNA splicing triggers an autophagic response in endothelial cells through BECLIN-1 transcriptional activation. J Biol Chem. 2013 Jan 11;288(2):859-72.

155.    Green AJ, Gelfand JM, Cree BA, et al. Clemastine fumarate as a remyelinating therapy for multiple sclerosis (ReBUILD): a randomised, controlled, double-blind, crossover trial. Lancet. 2017 Dec 2;390(10111):2481-2489.

156.    Apolloni S, Fabbrizio P, Parisi C, et al. Clemastine Confers Neuroprotection and Induces an Anti-Inflammatory Phenotype in SOD1(G93A) Mouse Model of Amyotrophic Lateral Sclerosis. Mol Neurobiol. 2016 Jan;53(1):518-531.

157.    Nicolau-Galmes F, Asumendi A, Alonso-Tejerina E, et al. Terfenadine induces apoptosis and autophagy in melanoma cells through ROS-dependent and -independent mechanisms. Apoptosis. 2011 Dec;16(12):1253-67.

158.    Hu WW, Yang Y, Wang Z, et al. H1-antihistamines induce vacuolation in astrocytes through macroautophagy. Toxicol Appl Pharmacol. 2012 Apr 15;260(2):115-23.

159.    Jakhar R, Paul S, Bhardwaj M, et al. Astemizole-Histamine induces Beclin-1-independent autophagy by targeting p53-dependent crosstalk between autophagy and apoptosis. Cancer Lett.

2016 Mar 1;372(1):89-100.

160. Jangi SM, Ruiz-Larrea MB, Nicolau-Galmes F, et al. Terfenadine-induced apoptosis in human melanoma cells is mediated through Ca2+ homeostasis modulation and tyrosine kinase activity, independently of H1 histamine receptors. Carcinogenesis. 2008 Mar;29(3):500-9.

161. B'Chir W, Maurin AC, Carraro V, et al. The eIF2alpha/ATF4 pathway is essential for stress-induced autophagy gene expression. Nucleic Acids Res. 2013 Sep;41(16):7683-99.

162. Py BF, Boyce M, Yuan J. A critical role of eEF-2K in mediating autophagy in response to multiple cellular stresses. Autophagy. 2009 Apr;5(3):393-6.

163. Dever TE. Gene-specific regulation by general translation factors. Cell. 2002 Feb 22;108(4):545-56.

164. Kinsey CG, Camolotto SA, Boespflug AM, et al. Protective autophagy elicited by RAF-->MEK-->ERK inhibition suggests a treatment strategy for RAS-driven cancers. Nat Med. 2019 Apr;25(4):620-627.

165. Chauhan S, Goodwin JG, Chauhan S, et al. ZKSCAN3 is a master transcriptional repressor of autophagy. Mol Cell. 2013 Apr 11;50(1):16-28.

166. Le Good JA, Ziegler WH, Parekh DB, et al. Protein kinase C isotypes controlled by phosphoinositide 3-kinase through the protein kinase PDK1. Science. 1998 Sep 25;281(5385):2042-5.

167. Squier TC. Oxidative stress and protein aggregation during biological aging. Exp Gerontol. 2001 Sep;36(9):1539-50.

168. Kao C, Chao A, Tsai CL, et al. Bortezomib enhances cancer cell death by blocking the autophagic flux through stimulating ERK phosphorylation. Cell Death Dis. 2014 Nov 6;5:e1510.

169. Ji MM, Lee JM, Mon H, et al. Proteasome inhibitor MG132 impairs autophagic flux through compromising formation of autophagosomes in Bombyx cells. Biochem Biophys Res Commun. 2016 Oct 28;479(4):690-696.

170. Wang D, Xu Q, Yuan Q, et al. Proteasome inhibition boosts autophagic degradation of ubiquitinated-AGR2 and enhances the antitumor efficiency of bevacizumab. Oncogene. 2019 May;38(18):3458-3474.

171. Glickman MH, Ciechanover A. The ubiquitin-proteasome proteolytic pathway: destruction for the sake of construction. Physiol Rev. 2002 Apr;82(2):373-428.

172. Marambio P, Toro B, Sanhueza C, et al. Glucose deprivation causes oxidative stress and stimulates aggresome formation and autophagy in cultured cardiac myocytes. Biochim Biophys Acta. 2010 Jun;1802(6):509-18.

173. Katoh-Semba R, Kitajima S, Yamazaki Y, et al. Neuritic growth from a new subline of PC12 pheochromocytoma cells: cyclic AMP mimics the action of nerve growth factor. J Neurosci Res. 1987;17(1):36-44.

174. Ory DS, Neugeboren BA, Mulligan RC. A stable human-derived packaging cell line for production of high titer retrovirus/vesicular stomatitis virus G pseudotypes. Proc Natl Acad Sci U S A. 1996 Oct 15;93(21):11400-6.

175. Suzuki A, Obi K, Urabe T, et al. Feasibility of ex vivo gene therapy for neurological disorders using the new retroviral vector GCDNsap packaged in the vesicular stomatitis virus G protein. J Neurochem. 2002 Aug;82(4):953-60.

176. Shikata Y, Yoshimaru T, Komatsu M, et al. Protein kinase A inhibition facilitates the antitumor activity of xanthohumol, a valosin-containing protein inhibitor. Cancer Sci. 2017 Apr;108(4):785-794.

177. Postuma RB, Berg D. Advances in markers of prodromal Parkinson disease. Nat Rev Neurol. 2016 Oct 27;12(11):622-634.

# Acknowledgements

ました東京大学大学院医学研究科教授　水島昇博士に厚く御礼申し上げます.

　　半年間の留学中，数多くの経験と知識を積む機会を与えて下さいました，英国・Newcastle University, Biosciences Institute 准教授　Viktor Korolchuk 博士，同研究員　Lucia Sedlackova 博士に心より御礼申し上げます.

　　本研究を遂行するにあたり，特別研究員として採用頂き特別研究員奨励費（Grant Number: 19J12969）をご支援頂きました日本学術振興会（JSPS）に謹んで御礼申し上げます.

　　また，慶應義塾大学理工学部生命情報学科ケミカルバイオロジー研究室秘書　梅崎秀香様には，様々な場面でサポートを頂きました. 同技術員　中島理子様，同卒業生　加藤直裕様，酒井駿様，三浦昌大様，戸塚美里様，後輩の柴原健介様，村岡慶人様には研究を進める上で必要不可欠な実験サポートとご助言を頂きました. 同卒業生　四方雄貴博士，井岡秀二博士，齋藤駿博士，溝谷優治博士には，様々な実験技術のご指導を頂き，数多くの相談に乗って頂きました. また，同訪問教授　久保和生博士，同研究員（現・順天堂大学医学部神経学講座特任助教）北川光洋博士には討論を通して数多くを学ばせて頂きました. 深く御礼を申し上げます. そして，研究生活を共にしたケミカルバイオロジー研究室の諸先輩方，同輩・後輩の皆様に深く感謝の意を表します.

　　最後に，私を常に暖かく見守り支えてくれた家族，友人に心より感謝致します.